Chemical Science

ROYAL SOCIETY OF CHEMISTRY

EDGE ARTICLE

View Article Online
View Journal | View Issue

Cite this: *Chem. Sci.*, 2023, **14**, 11647

All publication charges for this article have been paid for by the Royal Society of Chemistry

Received 2nd May 2023
Accepted 1st July 2023

DOI: 10.1039/d3sc02238b

rsc.li/chemical-science

The borderless world of chemical bonding across the van der Waals crust and the valence region†‡

Jorge Echeverría [a] and Santiago Alvarez [b]

The definition of the van der Waals crust as the spherical section between the atomic radius and the van der Waals radius of an element is discussed and a survey of the application of the penetration index between two interacting atoms in a wide variety of covalent, polar, coordinative or noncovalent bonding situations is presented. It is shown that this newly defined parameter permits the comparison of bonding between pairs of atoms in structural and computational studies independently of the atom sizes.

When any body exists in the elastic state, its ultimate particles are separated from each other to a much greater distance than in any other state; each particle occupies the centre of a comparatively large sphere, and supports its dignity by keeping all the rest, which by their gravity, or otherwise are disposed to encroach upon it, at a respectful distance.

John Dalton, *A New System of Chemical Philosophy*, Manchester, 1808.

We, chemists, tend to idealize atoms as hard spheres that may exist independently or connected by sticks with other atoms to form molecules, chains or networks. The sizes of those spheres and the lengths of the sticks – the chemical bonds – are instrumental in describing and understanding the structure, stability and reactivity of chemical entities. In this work, we are concerned with a general way of describing and interpreting the distance between two such spheres, regardless of whether we connect them with a stick (chemical bond) or not (non-bonded atoms). To this end we first need to set up the conceptual description of an atom, based on the ideal spherical atom of Dalton and Bohr and on our current knowledge of the distribution of its electron density when isolated or within a chemically bonded polyatomic species. Even if we know that bonded atoms are not spherical,[1,2] they can be reasonably considered as spheres that are slightly flattened along bond directions (Fig. 1a).

The first thing to notice is that the shape of an atom is defined by the envelope of its electron density. However, due to the exponential decay of the probability function of atomic orbitals with the distance to the nucleus, the border of an atom is not clearly defined and one must adopt a convention, such as admitting that the surface of an atom is a sphere that contains 99% of its electron probability density. Alternatively, one could consider the distance from the nucleus at which the electron density reaches a sufficiently small value (*e.g.*, 0.001 e bohr^{-3}, as proposed by Rahm and Hoffmann[3]) to define the radius of an atomic sphere.

For the present work, we find it appropriate to consider an atom as formed by three concentric spheres that contain regions of decreasing electron density. In such a model, the

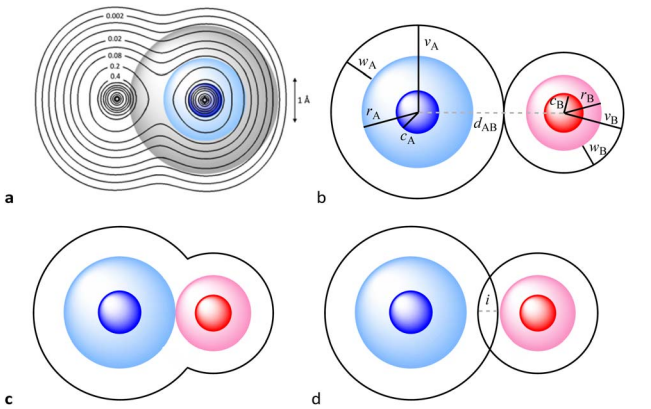

Fig. 1 (a) Calculated electron density map for a Cl_2 molecule superimposed on the idealized core (dark blue), valence (light blue) and van der Waals (grey) spheres of one of the Cl atoms defined by the corresponding radii. Isodensity lines are shown in electrons bohr^{-3}. (b) Definition of the core (dark colour), valence (light colour) and van der Waals (transparent) spheres with radii *c*, *r* and *v* and of the van der Waals crust of width *w* for atoms A and B, and visual description of the case of two contacting van der Waals spheres with no interpenetration ($p_{AB} = 0\%$). (c) Schematic description of the case in which two atoms are at a distance equal to the sum of the covalent radii ($d_{AB} = r_A + r_B$), which corresponds to a penetration index $p_{AB} = 100\%$. (d) Degree of interpenetration (i) of the van der Waals crusts of two atoms.

[a]*Instituto de Síntesis Química y Catalisis Homogénea (ISQCH) and Departmento de Química Inorgánica, Facultad de Ciencias, Universidad de Zaragoza, Pedro Cerbuna 12, 50009 Zaragoza, Spain. E-mail: jorge.echeverria@unizar.es*

[b]*Department de Química Inorgànica i Orgànica, Secció de Química Inorgànica, e Institut de Química Teòrica i Computacional, Universitat de Barcelona, Martí i Franquès 1-11, 08028 –Barcelona, Spain. E-mail: santiago@qi.ub.es*

† Dedicated to Prof. Juan J. Novoa, in memoriam.

‡ Electronic supplementary information (ESI) available. See DOI: https://doi.org/10.1039/d3sc02238b

inner sphere corresponds to the high electron density associated with core electrons, the second sphere contains in addition the electron density corresponding to the valence electrons, and the outermost sphere also includes the low electron density characteristic of the van der Waals space. The sizes of those spheres can be defined by the core,[4] covalent, and van der Waals radii, for which we use the symbols c, r, and v, respectively (Fig. 1b). These spheres correspond to well-defined regions of electron density, as can be seen in textbook representations[1,5] and illustrated in Fig. 1a through the calculated electron density map for the Cl_2 molecule (see the ESI‡ for computational details). From another point of view, the size of such spheres is associated with the radial extent of atomic orbitals, since in an atom with valence orbitals of quantum number n they contain the electrons of the shells with quantum numbers 1 to $n - 1$ (core sphere), n (valence sphere) and $n + i$ (van der Waals region and beyond, with $i \geq 1$).

In what follows we will employ the empirical sets of atomic covalent[6] and van der Waals[7,8] radii, based on crystallographic and spectroscopic gas phase structural data, proposed in recent years by us, which have been widely applied by the chemical community. The relationships of atomic radii with other parameters, such as the electrostatic potential felt by a valence electron, a constant value of the electron density, or atomic softness or atomic polarizability, have been extensively reviewed.[3,9]

When two atoms are involved in a bonding interaction, the outermost spheres of electron density interpenetrate to a greater or lesser extent depending on the strength of the interaction. The two canonical cases of covalent bonding and van der Waals interactions, corresponding to interatomic distances $d_{AB} = r_A + r_B$ and $d_{AB} = v_A + v_B$, respectively, are schematically represented in Fig. 1b and c, respectively. If we refer to the section of the van der Waals sphere external to the valence sphere (the transparent portion in Fig. 1b–d) as the van der Waals crust, its width is defined as $w = v - r$.[10,11] It is thus straightforward to calculate those widths for most chemical elements (Fig. 2a; data in Table S1 of the ESI‡).

Although there seems to be no clear periodic trend in crust widths, it is interesting to note that all of them fall between 0.60 and 1.20 Å, the large majority being between 0.80 and 1.10 Å. The portion of the volume of the van der Waals sphere that is occupied by the crust can be easily calculated (see Appendix in the ESI‡). Those volume fractions are presented in Fig. 2b, where we can see that for practically all naturally occurring elements the crust represents at least 60% of the volume of the van der Waals sphere, being higher than 90% for the lightest elements H, He and B to Ne. The element with the narrowest crust within each period is the alkali metal, whereas the widest crusts correspond to noble gases and late transition metals. It can also be seen that the proportion of the van der Waals crust appears to be roughly constant for the whole family of lanthanides.

Now we can face the aim of this work, to adopt a general parameter that describes the degree of interpenetration of the van der Waals and valence spheres of two atoms and check for its applicability to a variety of chemical systems, from the weakly interacting van der Waals diatoms held by London dispersion forces to the strongest multiple covalent bonds. Earlier attempts to normalize an interatomic distance d_{AB} by comparing it with the sum of the van der Waals radii include the proposal of Lommerse and co-workers[12] of using the quotient of the distance over the van der Waals radii sum, $\lambda = d_{AB}/(v_A + v_B)$. It adopts values smaller than one for distances shorter (and larger than one for distances longer) than the van der Waals sum. In other cases, the "corrected" or "relative" E···H distance, $d_{AB} - (v_A + v_B)$, has been used, *e.g.*, to compare the hydrogen contacts of a group 14 element[13] or in the study of π-hole interactions between nitro aromatic ligands and lone pairs within protein structures.[14] Those corrected distances are negative for contacts shorter than the van der Waals radii sum and positive for longer contacts, but it does not seem that they can be used for the comparison of interactions involving different atom pairs or for stronger interactions such as covalent bonds.

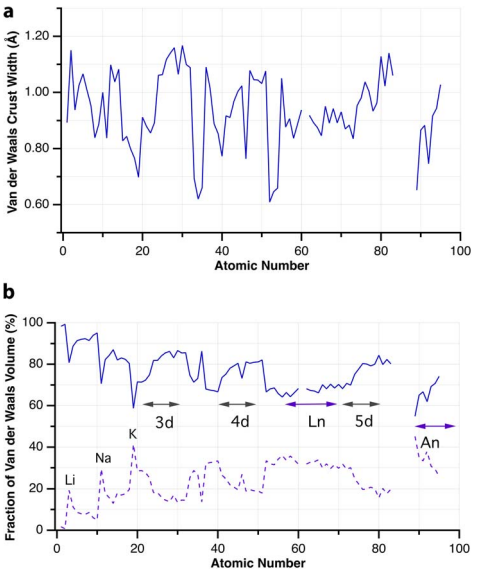

Fig. 2 (a) Widths of the van der Waals crusts for the first 95 elements. (b) The portion of the van der Waals sphere occupied by the van der Waals crust and by the valence sphere (dashed line). Data are provided in ESI, Table S1.‡

We propose instead to explore the applicability of our definition[10] of a penetration index to a wide variety of types of interatomic interactions. In short, the penetration index between atoms A and B is the ratio between the interpenetration of the two van der Waals crusts, $i = v_A + v_B - d_{AB}$ (see Fig. 1d) and the sum of the crust widths (eqn (1)). The introduction of a 100 factor results in the penetration index adopting values of 0% when the two van der Waals spheres are just touching each other (*i.e.*, $d_{AB} = v_A + v_B$) and 100% when they are interpenetrating up to the point where the two valence spheres touch each other (*i.e.*, $d_{AB} = r_A + r_B$), the two situations shown schematically in Fig. 1b and c.

$$p_{AB} = 100 \cdot (v_A + v_B - d_{AB})/(v_A + v_B - r_A - r_B) \quad (1)$$

With such a definition, any combination of two elements at a distance equal to the sum of the covalent radii is represented by a 100% penetration, whereas all the atom pairs at a distance equal to the sum of their van der Waals radii consistently have a 0% penetration index. In other words, we have a metric that is independent of the size of the interacting atoms. Of course, given the variability of the covalent bond lengths involving the same atom pair, we must expect that values of around zero correspond to van der Waals interactions and values of approximately 100 correspond to a covalent single bond.

In many instances of weak, non-covalent, secondary bonding or non-bonding interactions, however, the interatomic distance is somewhere in-between the sum of the covalent and the van der Waals radii sums, $r_A + r_B < d_{AB} < v_A + v_B$ (Fig. 1d). For those situations, we have a quantitative measure of the degree of interpenetration, which might calibrate the strength of such interactions, as we will extensively analyse in this work. This will greatly facilitate a wider and simpler perspective on many aspects of chemistry in which two-atom interactions are important, such as bonding, transition states and reaction mechanisms, non-covalent interactions and crystal engineering, ligand–protein interactions, or structural correlations.

Notice that a negative value of p_{AB} indicates that fuzzy van der Waals spheres are conventionally not interpenetrated, although a rather weak attractive interaction cannot be ruled out. In addition, the absolute value of a negative penetration index provides a qualitative description of the interaction as probably weakly attractive (small negative values) or as non-interacting or repulsive (large negative values). Conversely, values of p_{AB} larger than 100% indicate covalent or ionic bonding and provide a qualitative indication of the strength of the bond, including differentiation of single and multiple bonds, as will be shown below. In summary, the values of the penetration index are intended to provide semiquantitative information about interactions within van der Waals crust regions but could also be used as a semiquantitative indicator beyond the limits of 0 and 100%.

Beyond $p = 100\%$, the interpenetration of the valence shells of the two atoms occurs, and one could also define the corresponding index for the interpenetration of the valence shells, using the radii of the atomic cores[4] c_A and c_B (eqn (2)). That index takes the value $p^{val} = 0\%$ when the interatomic distance is equal to the sum of the covalent radii, and. $p^{val} = 100\%$ when the two atomic cores are in contact. For the common case of two interacting atoms with different crust widths, the degree of penetration of the crust of an atom A by a wider crust of an atom B, p_B, is larger than the penetration of the crust of B by that of A, p_A. For the interest of the reader, such individual penetration indices are discussed in an Appendix included in the ESI.‡ However, since the use of the joint index p_{AB} is simpler and powerful enough, as will be shown in what follows, we will use only the latter throughout this paper. Similarly, the possibility of using a volumetric interpenetration measure is analysed in the ESI, Appendix‡ but will not be further pursued in this work.

$$p^{val} = 100\cdot(r_A + r_B - d_{AB})/(c_A + c_B) \quad (2)$$

van der Waals complexes involving noble gases

Noble gas dimers

We start looking at the prototypes of van der Waals interactions, the noble gases that form weakly bound diatoms, but for which a great deal of chemistry involving other types of bonding has also been developed[15] since the pioneering work of Neil Bartlett.[16] For this purpose, we have performed DFT calculations in a range of interatomic Ng···Ng distances (we will use the symbol Ng to represent any noble gas throughout) and performed energy decomposition analyses (EDA). To work with penetration indices instead of interatomic distances we must use a modified version of the Lennard-Jones potential, in which the distance is replaced by $100 - p$ (eqn (3)), where ε and σ correspond to the depth of the potential well at the minimum and to the value of $100 - p$ at which the energy crosses the zero line (*i.e.*, $p_0 = 100 - \sigma$, the penetration counterpart of the spinoidal radius discussed by Lobato *et al.*[17]), respectively, and n is a fitting parameter that in the common Lennard-Jones formulation would adopt a value of 6. By equating to zero the derivative of the energy with respect to p, the expression in eqn (4) gives us the penetration index at the minimum, p_{min}.

$$E = 4\varepsilon\left[\left(\frac{\sigma}{100-p}\right)^{2n} - \left(\frac{\sigma}{100-p}\right)^{n}\right] \quad (3)$$

$$p_{min} = 100 - \sigma \times 2^{\frac{1}{n}} \quad (4)$$

The calculated energy curves are shown in Fig. 3 and the relevant fitting parameters are presented in Table 1. The fittings do not reproduce very well the high energy branch beyond p_0, which is nevertheless irrelevant for the present discussion, since the zone around the minimum and the pre-dissociation region are well reproduced. Several observations can be made based on those results:

(a) All the interaction energies are similar, between −0.7 and −1.1 kJ mol^{-1}, with an average of −0.91 (9) kJ mol^{-1}.

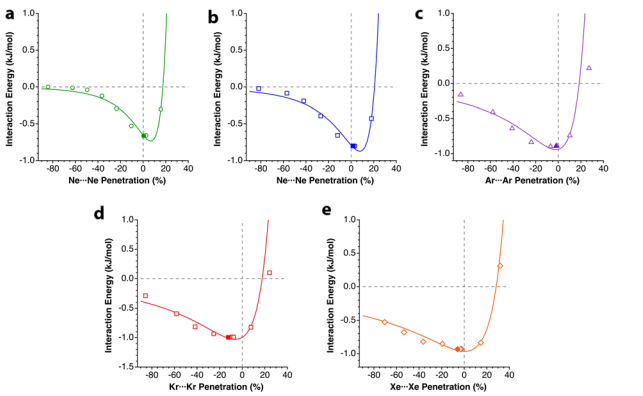

Fig. 3 Interaction energy of Ng_2 adducts represented as a function of the penetration index for He to Xe. The solid symbols correspond to the optimized Ng–Ng distance. Data are provided in ESI, Tables S2–S6.‡

Table 1 Fitting of the potential energy curves of Ng_2 dimers[a] to the Lennard-Jones potential of eqn (3), and penetration index for the optimized structures (p_{opt}, experimental value in parentheses)

	ε	σ	n	p_{min} (%)	p_{opt} (%)	χ^{2b}	p_0
HeHe	0.733	82.56	5.7034	6.77	0.40	0.016	17.44
NeNe	0.871	79.32	4.5673	7.68	1.97(3.3)[20]	0.018	20.68
ArAr	0.942	81.51	3.0725	−2.14	−1.99(6.6)[21,22]	0.029	18.49
KrKr	1.028	82.35	2.7177	−6.27	−12.37(6.8)[23]	0.025	17.65
XeXe	0.963	71.72	2.1109	0.40	−6.03	0.026	28.28

[a] Points with $p > 20\%$ were excluded from the fitting. [b] Parameter that measures the goodness of fit.

(b) In all cases, penetrations at the energy minimum, p_{min}, are around 0%, between −6.2 and 7.5%, consistent with the expectations for purely van der Waals interactions.

(c) The width of the potential energy well increases as we go down the group, as indicated using the decreasing value of n (see Tables S2–S6, ESI‡). This fact should be reflected in the stretching force constant and, consequently, in the wavenumber of the signal in the Raman spectra.

(d) The penetration index of the optimized molecules is well correlated with the value obtained from the fitting of the energy scan to the Lennard-Jones potential. The linear correlation found is shown in eqn (5).

$$p_{opt} = 1.0264 \times p_{min} - 5.6574 \ (r^2 = 0.97) \quad (5)$$

High-level calculations place the minimal energy for the He_2 dimer at 2.96 Å,[18] *i.e.*, a penetration index of −4.3%. Some dispersion, of a few percent units, is not unexpected, due to small dissociation energies and shallow potential wells. Calculations reported by other authors[19] consistently yield minima with penetrations between −7 and +5% for the dimers of He, Ne and Ar, as well as for the mixed diatomics HeNe, HeAr, and NeAr.

The penetration dependence of the different contributions to the interaction energy in the Ng_2 dimers, according to an energy decomposition analysis (EDA), is presented in Fig. 4. It is rewarding to find very similar patterns for the five noble gas dimers analyzed, which can be summarized as follows:

1.- The orbital and dispersion attractive interaction terms operate at penetrations of about −30% or less, at which the electrostatic and Pauli components are still negligible.

2.- At penetrations near the energy minimum the London dispersion is the predominant attractive force in all cases.

3.- Further penetration is prevented by a rocketing increase in the Pauli repulsion energy.

4.-The Pauli repulsion appears at lower penetrations than the electrostatic attraction.

5.- The absolute values of the Pauli repulsion and the electrostatic attraction follow a similar exponential dependence on the penetration index, and they are nicely correlated (Fig. 5a and b).

6.- As a result of the two previous points, the electrostatic term cannot by itself stabilize the dimers of the two neutral Ng atoms.

7.- The combined effect of the Pauli and electrostatic terms shows an exponential dependence on the penetration index,

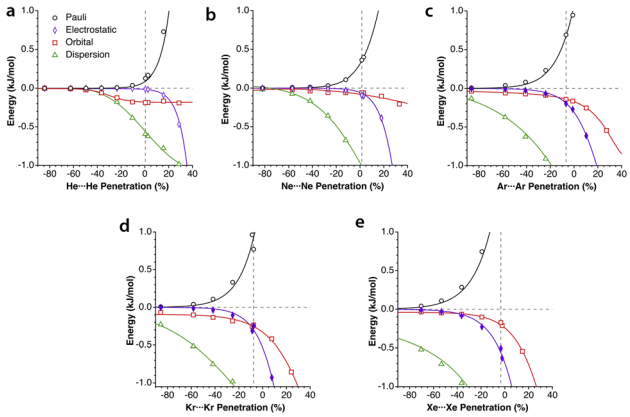

Fig. 4 Evolution of the components of the interaction energy as a function of the penetration index for noble gas dimers. The vertical dashed lines indicate the position of the energy minima. Data are provided in ESI, Tables S2–S6.‡

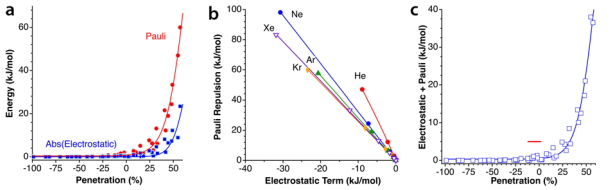

Fig. 5 (a) Electrostatic and Pauli components as a function of the penetration index for all the Ng_2 adducts. (b) Correlation between the electrostatic and Pauli components for each Ng_2 dimer. (c) The sum of the Pauli and electrostatic components as a function of the penetration index for all the Ng_2 dimers. The horizontal straight segment indicates the range in which the dimers are stable toward dissociation. Data are provided in ESI, Tables S2–S6.‡

roughly independent of the noble gas considered (Fig. 5c), preventing the dimers from reaching penetrations higher than a few percentual units.

8.- Point 7 implies that the electronegativity or size of the noble gas atoms is practically irrelevant in determining the degree of interpenetration of the Ng_2 dimers.

After having seen how the penetration index allows us to calibrate on the same scale the van der Waals interactions in a computational study of the dimers of the noble gases, we turn our attention to the experimental information by analysing all the structures that contain only noble gases, either in the gas phase (as found in the Mogadoc database)[24] or in the solid state, retrieved from the ICSD.[25] The ranges of penetration indices found are summarized in Fig. 6, while numerical data and references are provided in the ESI (Table S7).‡ Experimental interatomic distances for the He_2 and Xe_2 complexes could not be found in the Mogadoc database but could be retrieved from the literature.[26,27] The dimers of the fleeting noble gases Rn and Og have been computationally studied,[28] and the results considered by the authors to be the best ones give interatomic distances of 4.42 and 4.28 Å. Since no reliable empirical van der Waals radii are available for these two elements,[6,24] their penetration indices in the optimized dimers can be taken as 0%,

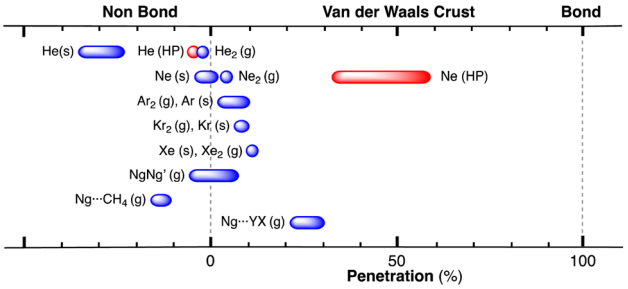

Fig. 6 Ranges of penetration indices found for pairs of noble gas atoms in the gas and solid states. Blue bars correspond to structures at atmospheric pressure, and red bars to structures under pressure. Ng stands for noble gases in general, and X and Y for halogens (data provided in Table S7 in the ESI‡).

assuming the corresponding radii to be half of the optimized interatomic distances (*i.e.*, 2.21 and 2.14 Å).

The ranges of experimental Ng···Ng penetrations in the dimers are consistent with the values found computationally, around the 0% mark. Since the van der Waals radii of noble gases used for the calculation of penetration indices[7] were obtained from the more abundant Ng···O distances rather than from Ng···Ng distances, it is understandable that the experimental values of the latter yield penetration values that are not strictly zero. However, the small positive or negative values found are consistent with the existence of predominant van der Waals interactions. It is remarkable that also the mixed noble gas adducts, Ng···Ng′, appear grouped around the zero mark with small positive or negative values. For comparison, we also include the penetrations of noble gases with methane in Fig. 6, which appear to be smaller than the noble gas-noble gas ones, as well as those of noble gases with halogen and interhalogen diatomic molecules XY, whose values are all above 20%, suggesting that important polarization effects supplement the dispersion attractive interaction. It is also noteworthy that the Ng···Ng penetrations in the solid state are in general smaller than those in the gas phase dimers, most likely due to the higher number of nearest-neighbors in the crystal structures.

Effect of pressure on noble gas···noble gas interpenetration

Experimental data involving He atoms in the solid state under pressure present nearest-neighbour penetrations that go from −34 to −25% as the pressure increases from 3 to 18 MPa and increase to −6% at a much higher pressure of 1.7 GPa.[29] The Ne_2 dimer in the gas-phase[20] has a penetration index of 3.3%, and similar penetration values (−1.8 to 1.4%) appear between the nearest neighbours in the solid state structure at atmospheric pressure.[30–32] Under high pressure (10–170 GPa),[33,34] however, there is a sharp increase in the Ne···Ne interpenetration, reaching indices in the range of 30–60% (Fig. 7). The heavier elements present increasing penetrations as the atomic number increases, as expected for dispersion-dominated interactions. Recent calculations on Ng_2 and NgNg′ dimers (Ng = Ne–Xe)[35] give somewhat shorter distances and small positive penetrations (1–11%).

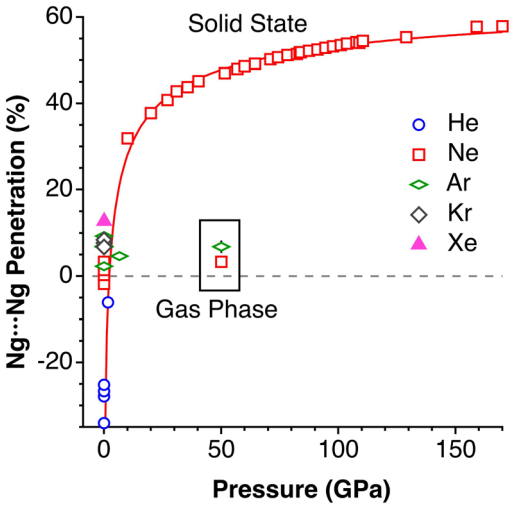

Fig. 7 Variation of the interpenetration of the Ng···Ng van der Waals crusts as a function of the applied pressure in the solid state. Penetrations for the Ng_2 dimers in the gas phase without applied pressure are shown in the inset for comparison.

Noble gas–molecule interactions

Another group of typically weak van der Waals interactions appears between noble gases and closed-shell molecules, such as methane. In the Ar···CH_4 adduct, for instance, the argon atom sits at the centre of a face of the tetrahedral methane molecule, with a negative penetration of the Ar and C atoms (−15.3%) and still more negative penetration for the Ar···H contacts (−36.0%). A similar behaviour is found for methane adducts with Kr and Xe. In summary, van der Waals complexes of noble gases with a small nonpolar molecule such as methane present negative p_{NgC} indices, between −11 and −15 (Ng = Ar, Kr, Xe) and smaller penetrations with H atoms, except for Xe that forms a Xe···H–C angle of 132°. If methane is replaced by difluoromethane,[36] the presence of a dipole moment makes the interaction with the noble gas more favourable, and slightly positive Ng···F penetration indices appear (8–10%). Also, the dipolar character of the interhalogen molecules Y–X, where Y is the less electronegative halogen of the molecule, results in significantly higher Ng···Y penetrations (between 21 and 30% for Ng = Kr, Y–X = Cl–F; Ng = Ar, YX = Cl–F, Br–Cl and I–Cl). It seems clear that, in this case, we can think about σ-hole interactions. Another interesting molecule that has positive penetration indices with noble gases (Ar and Kr) is SiF_4. Even if it doesn't have dipolar character, the polar nature of the Si–F bonds allows for σ-hole interactions through the centre of a tetrahedral face and Ng···Si penetration indices of around 17%.

A study of the structure of 4-cyanophenol using helium as a pressure-transmitting medium has been reported,[37] and two phase transitions have been found at 2.4 and 3.6 GPa. The authors analysed the effect of applied pressure on the hydrogen bonding and π–π stacking interactions that determine the crystal packing at atmospheric pressure.[38] They observed that the π–π interactions are much more affected by pressure than

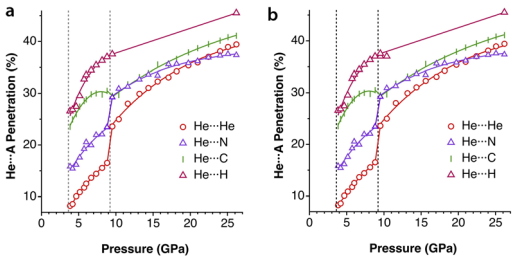

Fig. 8 Changes in the penetration indices of (a) the C···C (π–π) and N···O (hydrogen-bonded) contacts and (b) several He···atom contacts with applied pressure in the crystal structure of 4-cyanophenol. The dotted vertical lines indicate two phase transitions. Penetration indices calculated from the structural data in ref. 37 and standard covalent[6] and van der Waals radii.[7] Data are provided in ESI, Table S8.‡

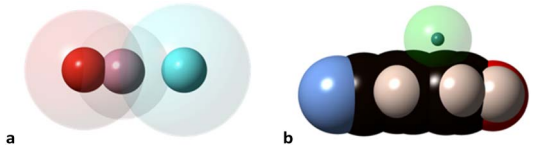

Fig. 9 van der Waals (transparent spheres) and valence (solid spheres) domains of the atoms in (a) the O–H···N hydrogen bond, and (b) interpenetration of the van der Waals crust of a He atom (transparent sphere) with that of the carbon atoms (black spheres) for the shortest He···π contact of *p*-cyanophenol as determined by synchrotron X-ray diffraction at 26.19 GPa (drawn from the structural data in ref. 37 and standard covalent[6] and van der Waals radii[7]).

the hydrogen bonding interactions. Taking the shortest non bonding C···C and N···O distances as an indication of the π–π and hydrogen bonding interactions, respectively, conveniently converted into the corresponding penetration indices (Fig. 8a), we see that this assertion holds for the intermediate pressure regime, in which the hydrogen-bonded N···O penetration increases in a practically linear way, while the C···C (π–π) interactions increase almost exponentially. In the high-pressure zone, however, the two interactions evolve in parallel, reaching penetrations as high as ∼40%.

A most interesting result is that the compound incorporates He atoms in-between the molecules at a pressure of 2.4 GPa and above, in increasing proportions as the pressure increases. Thus, after a first phase transition at 2.68 GPa, He···H, He···N and He···O contacts with penetration indices in the range of 13–25% appear. At pressures higher than 3.4 GPa, the pressure-transmitting He atoms are incorporated within the crystal structure and penetrate the van der Waals crust of the C and H atoms (Fig. 8b). Above 9 GPa there is another phase transition that implies a leap in the He···N and He···He penetrations and, from there on, He···He, He···C, He···N and He···H penetrations increase at the same pace with increasing pressure. He and H atoms seem to interpenetrate more than the other atom pairs, although this conclusion should be taken with a grain of salt, given the usual uncertainty associated with the localization of hydrogen atoms from X-ray diffraction data and the disorder that affects the He atoms in that pressure range. The quite similar degree of interpenetration of different atom pairs, and the fact that they increase similarly with the applied pressure, suggests that at this point the whole crystal could be described as a close packing of fluffy spheres of different sizes, compressed in similar proportions.

Notice that in the O–H···N hydrogen bond there is interpenetration of not only the H and N crusts (70%) but also the O crust that extends beyond the hydrogen atom and interpenetrates 37% with the N crust, as can be appreciated in Fig. 9a. Similarly, the interpenetration of the He and aromatic C atoms becomes large at high pressures (Fig. 9b). The finding of the H-mediated interpenetration of the hydrogen-bonded oxygen and nitrogen atoms is consistent with our earlier orbital analysis of the superexchange interaction between two square planar Cu(II) ions in hydrogen-bond bridged Cu(II) dimers, which was found to be due to direct through-space interaction between the oxygen atoms of the two monomers, whereas the hydrogen bridges play essentially an indirect structural role by holding those oxygens at a close distance.[39] Although to a lesser extent, this phenomenon also appears at ambient pressure, with H···N and O···N penetration indices of 50–55% and 19–20%, respectively, in several structural determinations at different temperatures and using diffractometers or synchrotron radiation.[37,38,40,41] Search for all O–H···N hydrogen bonds in the Cambridge Structural Database (see the Methodology section) shows this to be a typical behaviour since the average penetrations with their standard deviations are 47(7)% for the H···N and 18(6)% for the O···N pair. Similarly, in O–H···O hydrogen bonds the H···O and O···O penetrations are 42(8) and 13(6)%, respectively.

Clathrates

Among the many clathrates that host noble gas atoms, we focus on a couple of illustrative examples. One of them, $Ar(D_2O)_3$, has been structurally analysed by neutron diffraction at 920 MPa.[42] In that structure, two Ar atoms are nearby (3.247 Å, p_{ArAr} = 36.0%) within a polyhedron formed by hydrogen-bonded water molecules, and Ar···O contacts at 2.164 Å indicate a surprisingly high degree of interpenetration of the corresponding crusts, p_{ArO} = 74.2%.

In the clathrate that forms hydroxiquinone with Xe at atmospheric pressure, the noble gas atom establishes contacts with 6 surrounding molecules through one of the hydroxyl groups and the orto C–H bonds, the highest penetration corresponding to the Xe···C atom pairs (3.7%), followed by the Xe···O pair (−1.9%) and smaller Xe···H penetrations (between −3.6 and −10.8%).[44]

The existence of endohedral fullerenes with a noble gas atom enclathrated within a C_{60} molecule, Ng@C_{60} (Ng = He, Ne, Kr)[45–47] has sparked much debate about the existence or absence of host–guest bonding. Merino and co-workers, for instance, carried out a computational study of different noble gases in C_{60}, dodecahedrane and cubane.[43] The use of penetration indices allows us to compare the noble gas–cage interaction energies for atoms of different sizes (Fig. 10). We note in passing that the penetration indices of the calculated structures

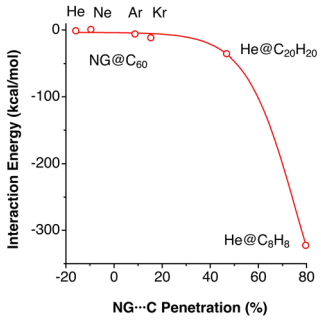

Fig. 10 Interaction energies of noble gas atoms with their carbon cages in endohedral fullerenes and polyhedranes plotted as a function of the Ng–C penetration indices. Data adapted from ref. 43 (ESI, Table S8‡).

are very similar to those found in the experimental structures of the clathrates Ng@C_{60} (Ng = He, Ne, Kr).[45–47]

A study carried out by Schwerdtfeger and co-workers reported calculations for a noble gas (He, Ne, and Ar) atom within C_n fullerenes, n being an even number from 20 to 60.[48] In a related computational experiment, Merino *et al.* introduced two He atoms inside a dodecahedrane molecule,[50] whereupon the He–He distance shortens to 1.265 Å, for a high penetration index of 69%, similar to the degree of interpenetration achieved experimentally between Ne atoms in the solid state under high pressure. In summary, while the contacts between noble gas atoms typically have penetration indices of around 0%, characteristic of dispersion interactions, their penetration with the cage atoms in clathrates can reach high values, most likely through donor–acceptor interactions with π* orbitals of the host. The representation of the calculated interaction energies as a function of the Ng···C penetration index (Fig. 11a) shows a similar behaviour of the three noble gases, to be compared with the large differences observed when the interaction energy is plotted as a function of the interatomic distance (Fig. 11b).

Krapp and Frenking computationally introduced two noble gas atoms in a buckminsterfullerene cage, Ng_2@C_{60}, with the Ng_2 pairs in three different orientations relative to the symmetry axes of the cage.[49] We refer to the original paper for a detailed discussion of the nature of the Ng···Ng and Ng···C interactions, but focus here on how the penetration indices of those two interactions show an excellent linear correlation (Fig. 11c), with the Ng···Ng penetrations almost doubling the Ng···C ones. Moreover, the fact that the penetrations become much larger than expected as the atomic size of the noble gas increases, largely exceeding 100% in the case of Xe, indicates that those atoms are mechanically kept at very short distances by the fullerene. It also makes us think about what changes must appear in the electronic structures of host and guest to allow the two Ng atoms to get so close to each other. Maybe an electron transfer to form covalently bonded Ng_2^+ or Ng_2^{2+} cations (the Kr_2^+ cation in the gas phase,[51] for instance, has a penetration index of 80%) and the well characterized C_{60}^- or C_{60}^{2-} fullerides?[52] An attempt to find a similar relationship using the interatomic Ng···Ng and Ng···C distances leads to a completely uncorrelated set of points (see ESI, Fig. S1a‡).

The Ng···Ng force constants present the well known correlation with the interatomic distances, known as Badger's rule[53] (Fig. S1b‡) and, interestingly, a simpler, linear correlation can be found between the force constants and the penetration indices (Fig. S1c‡). Also the electron density at the Ng···Ng bond critical points found by Krapp and Frenking is nicely correlated with the penetration index (Fig. 11d), whereas a poorer correlation is found with the interatomic distances (Fig. S1d in the ESI‡).

A related study on up to six noble gas atoms within carbon, boron or water clathrates or within BN doped carbon nanotubes has been reported by Merino, Chattaraj and coworkers.[54]

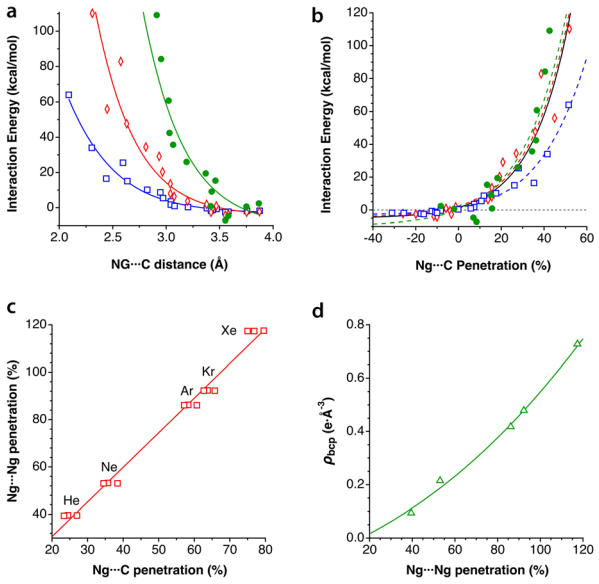

Fig. 11 The interaction energy between fullerenes C_{20}–C_{60} and an enclathrated noble gas atom as a function of (a) the Ng···C penetration index and (b) the Ng···C distance. Data were adapted from Schwerdtfeger *et al.*[48] (see ESI, Table S9‡). (c) Relationship between the Ng···Ng and Ng···C penetrations in Ng_2@C_{60}, and (d) dependence of the electron density at the Ng···Ng bond critical point on the penetration index, elaborated from data published by Krapp and Fenking.[49]

Tip–molecule interaction in electron probe microscopy

In the field of atomic probe microscopy, progress is continuously being made in obtaining images of electron density on small molecular regions while, at the same time, studies of electron transfer between the microscope's tip and a single molecule are of great importance for the development of molecular electronics. In this context, Mallada *et al.* recently reported[55] images of a σ-hole in the electron density of C(*p*-PhX)$_4$ (X = F, Br) on an Ag(111) surface using Kelvin probe force microscopy with Xe and CO tips. They computationally analysed the interaction between the tip and a halogen atom of the adsorbed molecules and found interaction energy *vs.* tip height curves in good agreement with the experimental observations.

To see how the use of penetration indices could be used in such a case, we plot in Fig. 12 the interaction energies between

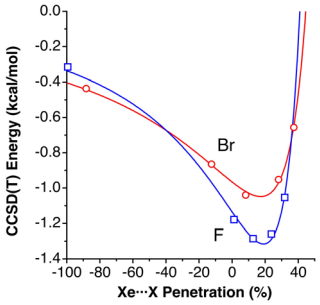

Fig. 12 Interaction energies between XPh molecules (X = F, Br) and a model of a Xe-terminated KFPM tip calculated by Mallada *et al.*,[55] represented as a function of the Xe···X penetration index. The curves are fittings to a modified Lennard-Jones potential (eqn (3)). Fitting parameters: $\sigma = 59.0942$, $\varepsilon = 1.3153$ and $n = 2.1968$ for X = F and $\sigma = 55.498$, $\varepsilon = 1.0480$, and $n = 1.7367$ for X = Br. Data are provided in ESI, Table S10.‡

XPh molecules (X = F, Br) and a model of a Xe-terminated KFPM tip calculated by Mallada *et al.*[55] as a function of the Xe···X penetration index. The calculated data can be fitted to a modified Lennard-Jones expression described above (eqn (3)), as shown in Fig. 12. We find it remarkable that the energy minimum for the tip-halogen atom interaction appears at practically the same degree of Xe···X penetration for the two halogens studied.

Inter-layer interactions in 2D solids

The weak van der Waals forces between layers in 2D solids are responsible at the same time for their crystallinity and their exfoliability. If the interlayer interactions depend on the same type of forces as for the noble gases discussed above, we should expect the ranges of penetration indices in layered solids to be similar to those found for noble gases.

Intercalated graphites

Intercalation and deintercalation of alkaline ions between the layers of graphite are processes of enormous importance due to their applicability as electrodes for batteries.[56,57] In the structure of naked graphite, the separation between the closest carbon atoms in neighbouring layers is 3.645 Å,[58] or a penetration index of −5%, consistent with the existence of weak van der Waals forces that account for the easy exfoliation of this material. When the metal content is low, as in LiC_{12},[59] LiC_{18},[60] or NaC_{64},[61] intercalated and unintercalated layers alternate, and two different interlayer distances must be considered. In those cases, both the unintercalated and intercalated layers present C···C penetrations similar to those in pristine graphite, of around 0%. In alkali-intercalated graphite with high metal content, as in LiC_6,[59] KC_8,[62] RbC_8,[63] and CsC_8,[63] all layers are intercalated and the interlayer distance is most likely determined by the size of the alkaline metal. The different behaviour of the two families of intercalated graphites is shown in Fig. 13a, where we also observe an excellent correlation between the covalent radius of the metal

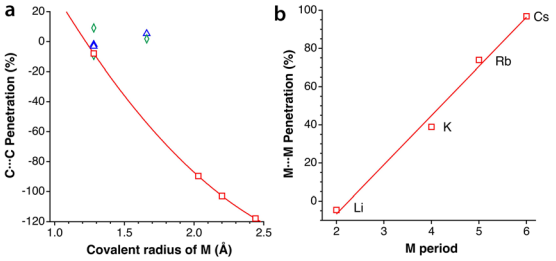

Fig. 13 (a) Interlayer C···C penetration as a function of the covalent radius of the metal M in intercalated graphites: unintercalated layers (rhombuses) and intercalated layers (triangles) in compounds with low metal content (triangles) intercalated layers in high metal content graphites (squares). (b) Intralayer M···M penetration in high metal content intercalated graphite as a function of the period of M.

atom and the interlayer C···C penetration, with the paradoxical result that for LiC_6 the interlayer penetration is similar to that between unintercalated or poorly intercalated graphite layers.

An additional interesting result of the penetration analysis of the structures of intercalated graphites is that the intralayer penetration between the metal atoms in the compounds with high metal contents (*i.e.*, LiC_6, KC_8, RbC_8, and CsC_8) increases in a practical linear way as we go down the group of alkaline metals, presenting an excellent correlation with the atomic number and with the period of the alkaline metal (Fig. 13b). Additionally, we notice that the H···H penetration indices between two layers of graphane, obtained from the structure optimized by Janowsky and Pulay,[64] are around −10% for the shortest contacts, slightly more negative than that for the C···C contacts between two layers of graphite.

Layered AX_2 and AX_3 solids

We have analysed a sample of 74 structures of binary 2D solids with AX_2 and AX_3 stoichiometries (X = Cl, Br, I, O, S, Se, Te), including 10 different structural types ($CdCl_2$, CdI_2, NbS_2, MoS_2, $TaSe_2$, WTe_2, graphite, $RhBr_3$, BiI_3, and NbS_3). The penetration indices for the shortest X···X contacts of each crystal structure are distributed around −3% (Fig. 14), covering a range between −25 and 25%, regardless of the structural type and the nature of

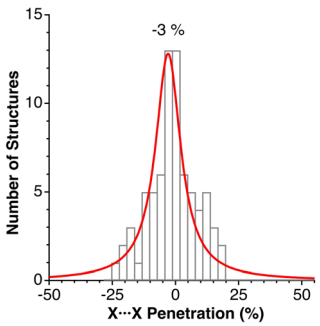

Fig. 14 Histogram and Lorentzian fitting of the distribution of the shortest interlayer penetrations in a sample of 2D solids. Data are provided in ESI, Table S11.‡

the cations and anions (A and X), similar to the behaviour found for the noble gas dimers (Fig. 7), but covering a wider range of values as could be expected for a much larger sample set and a wider variety of chemical compositions.

Rydberg molecules

An atom that holds an electron in an atomic orbital with a higher principal quantum number n than the valence shell is called a Rydberg atom. Similarly, a molecule with an electron in an outer shell is termed a Rydberg molecule. Such Rydberg states can engage in weakly attractive interactions with atoms, ions, or molecules. Presently, there is much interest in ultralong range Rydberg molecules that can be obtained in ultracold gases, generating *via* laser irradiation Rydberg states that may form bonds at distances in the range 3–9 μm (*i.e.*, one thousand times longer than typical bond distances), with lifetimes of the order of tens of μs. For instance, $Rb(5s^1)$–$Rb(ns^1)$ "macrodimers" formed by a ground state atom and a Rydberg atom with n = 35–37 have been reported, with lifetimes of 15–18 μs.[65,66] Also a bond between an Rb ion and a Rydberg Rb atom, predicted in 2000,[67] has been detected recently.[68] Certainly, those interactions do not imply interpenetration of van der Waals crusts, but many Rydberg molecules studied earlier imply lower-lying excited states and indeed form within the van der Waals playground.

Attachment of an electron to an ammonium ion results in a neutral Rydberg molecule NH_4, and a second electron gives rise to a double-Rydberg (DR) molecule NH_4^-,[69] since two electrons are found in a Rydberg-like orbital that is distributed in the periphery of a closed-shell ammonium cation.[69] Interestingly, in this (and other) Rydberg and DR molecules chemical bonds seem to be not significantly affected, and the penetration of the N and H crusts in NH_4 and NH_4^- is 99%, compared to that in the ammonium cation, *e.g.*, 100% in the solid state structure of $(ND_4)F$ determined by neutron diffraction,[70] and similarly for the independent cation in the gas phase.[71] However, the DR structure is a local minimum unstable toward dissociation into ammonia and hydride,[72] with an activation energy of around 14 kcal mol^{-1} needed to separate one of the hydrogen atoms to a penetration index of 57%. Similar considerations apply to the H_3O Rydberg molecule and the DR H_3O^- anion derived from the hydronium cation.[69]

Two Rydberg molecules may use their Rydberg electrons to form a two-electron chemical bond, as shown computationally by Boldyrev and Simons for the case of dimers of NH_4.[74] Although those dimers are unstable toward dissociation into $2NH_3 + H_2$, they are local minima with small energy barriers. Given their Rydberg nature, there is no need for a high interpenetration of the van der Waals crusts, yet, in the case of the D_{3d} dimer with a single short H···H contact (2.354 Å), the penetration index p_{HH} is 3%, within the range of values found for pure van der Waals interactions (Fig. 3). The same authors explored later the formation of bonds in the Rydberg NH_4 molecule with alkaline atoms.[73] Some of their results are summarized in Fig. 15, where it is noted that the penetration index between the contact atoms, p_{HM}, is now much higher (25–56%), since overlap with the valence orbitals of the alkaline atom is required in this case. It can also be observed that the more electropositive the alkaline atom is (and the smaller), the higher the penetration, while the N–H bond is much less sensitive to the degree of H···M penetration, taking as a reference the value for the independent NH_4 molecule. The transition state for the dissociation of the metastable Rydberg bonds requires enhanced M···H penetration, close to forming M–H bonds, and a simultaneous depenetration of the N and H atoms, leading finally to the thermodynamically favoured product, NH_3 + M − H.

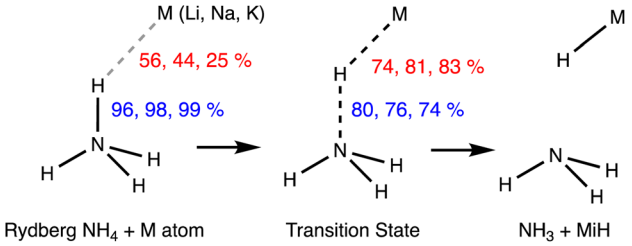

Fig. 15 Penetration indices of the N–H bond of an NH_4 Rydberg molecule and its H···M contacts with alkaline ions in the metastable state (left) and in the dissociation transition state (centre) to the products of a proton transfer reaction (right). Adapted from data reported by Boldyrev and Simons.[73]

Metallophilic interactions

The most abundant and most studied examples of metallophilic ($d^{10}\cdots d^{10}$ or $d^8\cdots d^8$) interactions are those involving two or more linearly coordinated Au(I) complexes and were termed "aurophilic",[75] a name that was later made more general to include other metals presenting similar metal–metal closed-shell interactions. The aurophilic interactions have been recently reviewed by Schmidbaur and Raubenheimer.[76] Those interactions were initially studied computationally *via* extended Hückel calculations by the Hoffmann group in related Cu(I) compounds[77] and in Au(I) compounds.[78] More recent studies on d^{10}–d^{10} interactions include Cu(I)[79] and Hg(II)[80] compounds. Similar interactions can be found between square planar d^8 metal centres.[81–83]

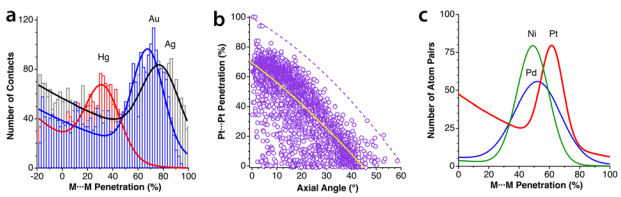

Fig. 16 (a) Distribution of metallophilic contacts between linear d^{10} complexes according to their M···M penetration indices. (b) Distribution of the Pt···Pt penetration index as a function of the stacking angle for contacts between square planar Pt(II) complexes. The continuous line indicates the general trend, and the dashed line corresponds to the highest values at certain angles. (c) Fitting of the M···M penetration index distribution for square planar complexes of Ni, Pd and Pt. Raw data are provided in ESI, Table S12.‡

If we look at the distribution of metal–metal penetrations between dicoordinated Ag(I), Au(I) and Hg(II) ions (Fig. 16a) we can see clear peaks with maxima at 32, 68 and 78% for Hg, Au and Ag, respectively. At lower penetrations, one can find an increasing number of structures that most likely do not present metallophilic interactions.

In Fig. 16b we present a scatterplot of the Pt⋯Pt penetration indices between neighbouring molecules of square planar Pt(II) complexes and the angle of the Pt–Pt vector with the Pt coordination plane. Although there is a high dispersion, most of the structures follow roughly a general tendency to present higher penetration indices as the deviation of the contact from the axial direction becomes smaller. Since metallophilic interactions are non-covalent, it is surprising to find in that plot four points with penetrations higher than 90%. They correspond to four crystallographically independent molecules in the crystal structure of a partially oxidized bisoxalatoplatinate salt with a fractional Pt–Pt bond order,[84] and similarly for a Pd compound with a penetration index of 91%.[85] The rest of the 3359 structures analysed have penetrations of at most 82%. We also pay attention to those structures with significantly higher penetration than others with the same angle. One is the double complex salt $[Pt(en)_2][Pt(CN)_4]$,[86] in which the Pt atoms of the cation and anion alternate in a regular stacking, thus adding an electrostatic attraction to the metallophilic interaction. In another case with an excess penetration,[87] two Pt atoms are close due to a short Pt⋯S contact as seen by comparing the Pt⋯S and Pt⋯Pt penetrations (73 *vs.* 21%). In yet another case, the neighbouring monomers are slipped in such a way that a Pt⋯O contact (52% penetration) predominates over the Pt⋯Pt one (4%).[88]

Finally, in Fig. 16c we compare the distribution of the M⋯M penetrations for square planar Ni(II), Pd(II) and Pt(II) complexes. It can be seen that the most common penetration indices for the three metals are within the 50–60% range, but also that there is a wide distribution of values that goes from 20 to an upper limit of 90%, with Pd showing the widest distribution.

Secondary metal–ligand interactions

We have analyzed some secondary intramolecular interactions between a square planar metallic atom and a pending phenyl group from the point of view of penetration indices and the results are summarized in Fig. 17a, where the peaks of the distribution of M⋯C penetrations are presented for M = Rh^I, Ir^I, Ni^{II}, Pd^{II}, and Pt^{II}. There, the maximum probability for the M⋯C contacts appears at quite similar degrees of penetration (24–29%), except for Pd, for which the distribution is slightly displaced to lower penetrations, centred at 18%. The corresponding secondary interactions of arenes with linearly coordinated Ag^I and Au^I ions have also been analysed and represented in Fig. 17a for comparison.

It is also interesting to compare the penetrations found in the recently reported structures of ethylene complexes of Cu^I, Ag^I and Au^I with tris(pyridyl)borate ligands coordinated in a bidentate mode, forming a trigonal planar coordination sphere.[89] These complexes present secondary interactions between the metal atom and the pending pyridyl ring, with penetrations of 66, 71 and 62% for Cu, Ag and Au, respectively, similar to the largest penetrations found for square planar and linear complexes. Notice that we show only a Lorentzian fitted to the peak of maximum probability but, in general, the distribution does not decay to zero at low penetration and continues to increase due to the presence in the crystal structure of weakly or non-interacting contacts, as seen in Fig. 16a and c.

Notably, secondary bonding of an aryl pending from a σ-coordinated phenyl group is also present in the first dinuclear compounds with quintuple Cr–Cr bonds reported by Power and coworkers.[90,91] C⋯Cr penetration indices for such interactions have values between 87 and 93%, *i.e.*, very close to a, if not a true, covalent bond. For comparison, the host of arenes coordinated in an η^6 mode to a Cr atom have average C⋯Cr penetration indices between 92 and 104%. Related compounds with quadruple Mo–Mo bonds from the group of Carmona[92–94] have similarly semi-coordinated aryl groups but with smaller C⋯Mo penetrations (61–83%). A quite different series of compounds but with similar bonding features contains a *p*-terphenyldiphosphine that was designed to act as a bidentate ligand through phosphine groups, while at the same time facilitating metal-arene interactions through the central phenyl ring.[95] When coordinated to Ni, Pd or Mo, the short C⋯M contacts have penetrations in the range of 73–104%, and only in an Ag^I compound does it drop to 65%.

A quite different example of secondary interactions focuses on the nitrato ligand acting in a monodentate coordination mode. In this case (Fig. 17b), the smaller size of the 3d metals (Co, Ni and Cu) facilitates a significantly higher penetration than that for the 4d (Cd and Pd) and 5d (W) metals. It must be noted that the two families of secondary bonds considered here cover a range of penetration indices similar to those found for hydrogen bonds (see below).

The importance of secondary interactions in solid-state chemistry was assessed by Landrum and Hoffmann,[96] paying attention in particular to those involving pnictogens and halogens. It was found that, for instance, Sb⋯Cl interactions cover a range of distances between 2.45 and 4.0 Å, *i.e.*, penetrations from 15 to 87%, like those shown by late transition metals with aryl groups (Fig. 17a) or by 3d metals with a monodentate nitrate anion (Fig. 17b).

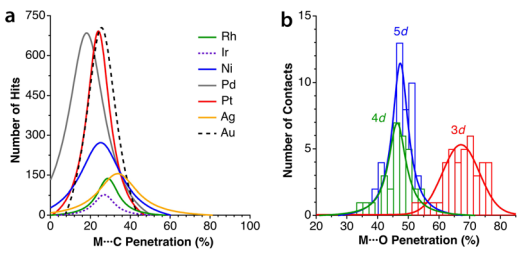

Fig. 17 (a) Distribution of the penetration indices of intramolecular arene⋯square planar and arene⋯linear metal atom secondary interactions. (b) Distribution of the penetration indices for the secondary interaction between a pending oxygen atom of a monodentate nitrato ligand and a square planar 3d, 4d and 5d transition metal atom. Data are provided in ESI, Tables S13 and S14.‡

The Jahn–Teller effect,[97,98] consisting of the distortion from a regular geometry of molecules with a degenerate ground state, is well known in coordination chemistry, mostly because it affects the large family of six-coordinated copper(II) complexes that commonly present two long copper–ligand distances in *trans* positions and four shorter ones in the equatorial plane of an elongated octahedron.[99] The elongation of the two axial bonds may be so large that in many cases the coordination sphere of Cu is described as square planar, but two secondary interactions can be identified in axial positions by close inspection of the crystal structure. Less well known is the fact that trigonal prismatic copper(II) complexes also present a Jahn–Teller distortion, but in this case affecting two *cis* ligands.[100] Certainly, the Jahn–Teller effect is present in a wide variety of chemical systems besides copper(II) complexes, but we focus here on them and on isoelectronic silver(II) compounds only to establish a connection with other non-Jahn–Teller secondary interactions. To this end, we have looked at the Cu···F (CSD) and Ag···F distances[101] and found the secondary interactions to cover the ranges 42–82% and 70–91%, respectively, compared to values of between 95 and 101% for the short M–F bonds in both cases. The low penetration limit, however, is an artifact dictated by the maximum contact distance adopted in structural database searches, and the two "tetracoordinated" metal ions have secondary interactions extending from a maximum of 95% to 0% or even negative penetration values.

Intramolecular contacts

Let us try to find some trends in intramolecular non-bonded contacts by looking first at simple AX_n molecules (A = group 13–16 elements and X = H or halogen), comparing them with the paradigmatic case of methane. By their bonding to the same carbon atom, two geminal hydrogens in alkyl groups are held nearby, resulting in a 35% interpenetration of their van der Waals crusts, as deduced from non-bonded H···H distances in methane in the gas phase. A similar value is obtained for the methyl groups in the CSD crystal structures without disorder, obtained by neutron diffraction and with an agreement factor *R* of at most 2.5% (ESI, Fig. S2‡). Replacing the central carbon atom of methane by an increasingly larger group-14 element increases the distance between the *gem* hydrogens, with a consequent decrease in the interpenetration of their crusts (Fig. 18a). A similar behaviour is found for groups 13 and 15 AH_3 and group 16 AH_2 molecules, with the hydrogen atoms becoming closer as we move from left to right of the periodic table within the same period.

We must note at this point that X-ray distances involving hydrogen atoms have larger uncertainties (typically 0.010 Å) than those for heavier atoms. For this reason, throughout this work we restrict structural database searches for distances involving hydrogen to non disordered structures, small *R* factors (<5% or <2.5%) and to neutron diffraction data, whenever these restrictions still allow us to work with a significant number of structural data. In all cases, however, differences of a few hundredths of an Ångstrom in distance do not have dramatic effects on penetration values. For instance, O···H distances of 2.65 and 2.69 Å differ in their penetration indices by only a 2.3%.

If we restrict the central atoms (A) to group 14 elements and replace the H atoms by halogen atoms, giving rise to AX_4 molecules (Fig. 18b), the variation in the penetration index with the size of A for a given halogen is quite like that for hydrides. The effect of the substitution of the external atoms, however, is less pronounced than that of the substitution of the central one, as seen by the smaller separation between the lines in Fig. 18b compared to those in Fig. 18a. The smaller effect of the size of X is explained as due to an increase in the A–X distance as we move down the halogen group, which increases the distance between the X atoms and is compensated for in part by the larger size of their van der Waals crusts. The effect of the increased steric crowding of a $Me_{3-n}H_nC$–X molecule on the C–X bond strength[102] is an indication of the importance of the interpenetration of geminal groups.

We cannot ignore that along the AH_3 (group 15) and AH_2 (group 16) series the H–A–H bond angle decreases drastically as we go from the second to the third period. While a smaller angle should result in a higher H···H penetration, the opposite occurs, and the compounds with larger bond angles are those with a higher H···H penetration (Fig. 18c). This behaviour is akin to the classical Gillespie–Nyholm explanation for varying bond angles, *i.e.*, the smallest central atoms impose shorter H···H distances (higher penetration), which can be relieved by increasing the bond angle.

Another factor that affects the penetration between *gem* atoms is hybridization, which imposes large differences in bond angles. Thus, the wider H–C–H angle in the sp^2 carbon atom of ethylene or formaldehyde, compared to that in the sp^3-hybridized methane, results in a slightly smaller interpenetration of the sp^2 *gem* H atoms, decreasing from 35 to 30%.

The interaction between vicinal H atoms, *i.e.*, those bonded to two neighbouring carbon atoms, seems to be much less important. Ethane and ethene present small negative values (−8 and −4%, respectively). The quite similar H···H penetration values despite the shorter C–C bond in the latter, appear because it is in part compensated for by larger C=C–H bond angles (120°) than in ethane (109.5°).

One of the classical examples in organic stereochemistry is the non-planarity of the biphenyl molecule, attributed to steric

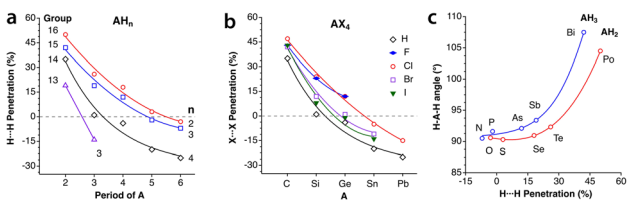

Fig. 18 (a) Variation in the penetration indices for the intramolecular *gem* H···H contacts in main group AH_n molecules (n = 3, 4, 3 and 2 for groups 13, 14, 15 and 16, respectively) with the size of the central atom. (b) A similar plot for the **14** AX_4 halides, with A being a group-14 element.(c) Correlation between the H-A-H fond angle and the *gem* H···H penetration for group 15 AH_3 and group 16 AH_2 molecules. Raw data are provided in ESI, Table S15.‡

repulsion between the *ortho* hydrogen atoms of the two phenyl rings. While Matta *et al.* proposed the existence of H···H bonding, based on a topological analysis of the electron density of biphenyl and related aromatic compounds,[103] Poater *et al.* ruled out a bonding interaction and found that steric repulsion prevented the minimum from having the coplanar conformation, based on an energy decomposition analysis (EDA) of phenanthrene, biphenyl and anthracene[104,105] and on calculations of a tetraradical molecule derived from biphenyl by removing the four *ortho* hydrogens. Other remarkable contributions include an article by Grimme *et al.* based on vibrational spectroscopy data[106] and an illuminating discussion on this topic by Krapp and Frenking.[49] Although it is not our purpose to participate in such a debate, we think that consideration of the crust interpenetration of atoms belonging to the same molecule can be of great help in analysing such problems from a wider perspective. Thus, in Chart 1 we show some of the molecules to be considered, together with their average H···H distances retrieved from the CSD and converted into p_{HH} penetration indices. For comparison, we also show in that chart the p_{HH} values for the *gem* and *vic* H atoms in methane,[107] ethane in its staggered conformation,[108] ethylene,[109] and cyclobutane.[110] Notice, for instance, that in the fully planar biphenyl characterized by Poater *et al.* as a transition state the interpenetration of the *ortho* hydrogen atoms is 26%, somewhat less than that between the *gem* H atoms in alkanes and alkenes.

Free bipyridine has an anti orientation,[111] and the H–H distance is rather long. However, the N···H penetration is 22%, and it seems likely that a non-negligible N···H interaction, be it attractive or repulsive, exists in that conformation between the nitrogen lone pair and the proximal hydrogen atom. We observe that in the nearly planar coordinated bipyridine, the H···H penetration is on average 12 (3)%, *i.e.*, significantly less than that in methane, ammonia or water (Fig. 18a). From the computational results for the biphenyl molecule just mentioned,[104] we find that the minimum with a torsion angle of 35.5° has a very low penetration index of 5.6%, well within two standard deviations of the average experimental value (Chart 1), while in the planar transition state the penetration is a non-negligible 26.1% and in the perpendicular orientation, also a transition state, there is no interpenetration of those H atoms at all, with an index of −64.5%.

The ability of the *tert*-butyl group to establish weakly attractive H···H interactions has been proposed to be responsible for unusual stabilities of long or congested C–C bonds. Matta *et al.*,[103] for instance, have estimated that each H···H contact in tetra-*tert*-butyltetrahedrane contributes 1.6 kcal mol^{-1} to the stability of the molecule, which they associate with H···H distances as short as 2.116 Å[112] (16% penetration). More recently, Schreiner and co-workers[113] have reported the neutron diffraction structure of tri(3,5-*tert*-butylphenyl)-methane, in which two molecules engage in a contact at a very short H···H distance (1.566 Å, 47% penetration) between their central C–H groups, supported by several H···H interactions between their *t*-butyl groups, but at distances of 2.39 Å and longer, *i.e.*, penetrations of at most a 1%. In summary, H···H contacts can help stabilize a molecule if they can have not too high interpenetrations, and the resulting molecular geometry results from a delicate balance of the penetration-dependences of the C–C bond and H···H contacts.

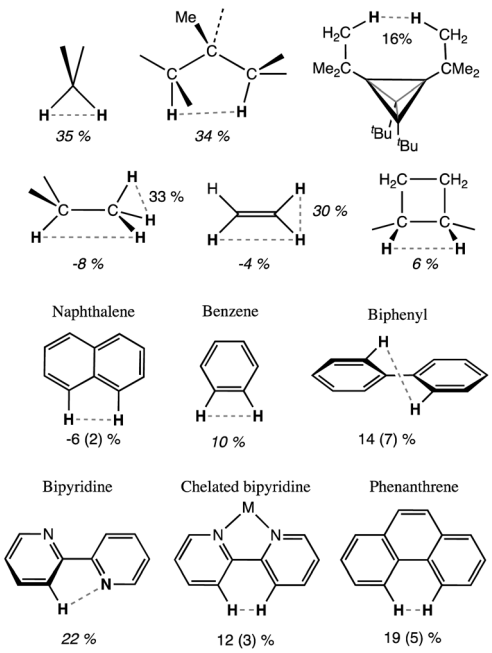

Chart 1 Intramolecular penetration indices of some organic molecules, from X-ray crystal structures (average of CSD structures with esds in parentheses) or from the gas phase (italics).

Agostic M···H interactions, alkane σ-complexes and dihydrogen coordination

Agostic interactions *vs.* σ C–H bond coordination

Prototypic organometallic complexes are those formed by an alkyl group coordinated to a transition metal (**1** in Chart 2). However, it was soon discovered that in some cases a distortion of a coordinated alkyl group allows for close contact between a hydrogen atom and the metal (**2** in Chart 2), for which the

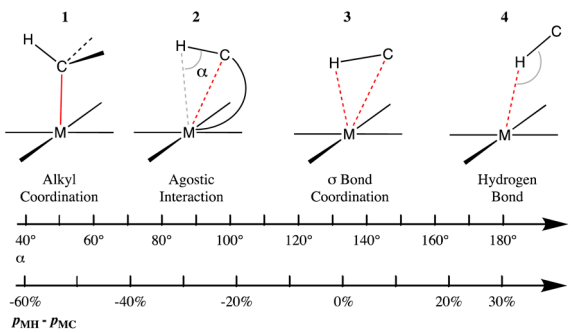

Chart 2 Different bonding situations between a C–H group and a transition metal, characterized by the M···H–C angle and the difference between the M–H and M–C penetration indices.

term "agostic bond" was coined.[114] The agostic interactions are not that different from the so-called σ-bond coordination, in which the C–H group and a metal atom form a 3 center-2 electron bonded system (**3** in Chart 2). Several reviews have been devoted to this family of compounds whose interest arises in good part from the possibility of acquiring a better understanding of the activation of C–H bonds in many processes catalysed by organometallic complexes.[115–118] A computational study of several Mn, Re and Rh σ-complexes has found that the dispersion interaction is largely responsible for thermodynamic stability of such species.[119]

Without loss of continuity, further geometrical changes may lead to C–H···M hydrogen bonds (**4** in Chart 2), also referred to as anagostic. The coordination of a C–H bond of an alkane to a Lewis acid such as a transition metal ion is nowadays well established in many cases,[120] in which the two electrons of the C–H bond are shared with the metal M and can thus be considered a specific type of 3c–2e bond. It seems clear that these four types of interactions between a metal atom and a C–H group are connected in a continuous geometrical pathway analogous to that proposed by Crabtree.[121] Such a pathway can be characterized by changes in the M···H–C angle, as well as by changes in the relative values of M–H and M–C penetrations, represented by the difference between the corresponding penetration indices, $p_{MH} - p_{MC}$, as shown in Chart 2. Notice that negative values of the penetration difference may suggest that the C–H unit interacts with the metal mostly through the carbon atom, whereas values close to zero point to a similar participation of both the C and H atoms, and large positive values indicate an interaction dominated by the proton-metal contact.

To test the ability of penetration indices to describe the different bonding situations in the metal–HC system, we have chosen to analyse prototypic structures that fulfill one of the three following criteria: (i) σ-bonded alkyl complexes from our database of homoleptic transition metal complexes,[122] (ii) prototypic examples of agostic and σ-bond coordinated complexes, and (iii) a representative sample of square planar metal complexes in which the metal atom is involved in hydrogen bonding with a C–H group (either intra- or intermolecular) selected from a large set of structures with M···H–C angles between 165 and 180° found in the CSD. One must be cautious with these numerical values, however, given the uncertainty associated with the position of H atoms determined by X-ray crystallography.

A plot of the differential penetration as a function of the M···H–C angle (Fig. 19, data are presented in ESI, Table S16‡) confirms the trend expected from Chart 2, with M···H–C angles covering the whole range between 40 and 180° and $p_{MH} - p_{MC}$ going from −60% (carbon-dominated bonding) to +30% (hydrogen-dominated bonding). It is also interesting to verify that the *cis* hydride and alkyl (or aryl) ligands in the same molecule are in a distinct situation, in which both the M–H and M–C penetrations are around 100% and therefore the differential penetration ($p_{MH} - p_{MC}$) values are concentrated around the 3% mark, while the H···C contacts have penetration indices between 0 and 45% (centred at 25%), similar to those found between *gem* H atoms in methyl groups or like those discussed above (Fig. S3 in the ESI‡).

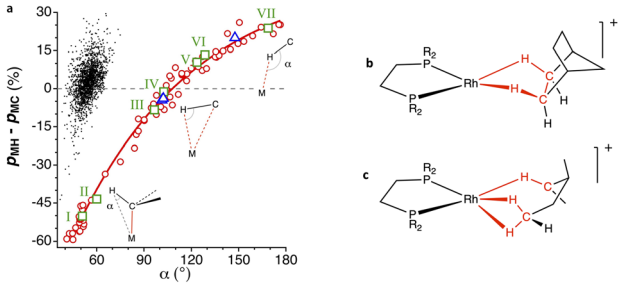

Fig. 19 (a) Difference of the M···H and M···C penetration indices represented as a function of the M···H–C angle (α) in σ-bond coordinated alkyl and aryl complexes (circles). The dots correspond to hydrides with a non-carbonylic carbon atom bonded in the *cis* position to the same metal atom. (b) Example of an alkane coordinated to a metal atom mostly through the hydrogens.[123,124] (c) Example of a molecule with one methylene group coordinated in an $\eta^2 : \eta^2$ mode and another in an η^1 mode (triangles in the plot). Data are provided in ESI, Table S16.‡

Let us now comment with some details on a few specific examples, highlighted in Fig. 19a as squares, that can be seen as snapshots along the bonding coordinate of Chart 2. First, we have the $[NbMe_6]^-$ anion (point I in Fig. 19a),[125] in which there is a regular tetrahedral Nb–C–H bond angle, which presents an M···H–C angle of 51°, a strong M–C penetration (109%) and a much lower, but non-negligible M–H penetration (59%), and a differential penetration of −50%. Even if it is clear in this case that there is a covalent M–C bond and just a *gem* contact between the M and H atoms, the interpenetration of these two atoms is comparable to those between hydrogen atoms in H_2O (Fig. 18).

An angular distortion of the Ti–Me moiety in the landmark titanium methyl complex $[(dmpm)Cl_3Ti–CH_3]$ (point II in Fig. 19a), with an M–C–H bond angle of 94°, is the signature for an agostic Ti···H interaction. The Ti···H penetration, at 69%, is only slightly larger than that in the non-agostic complex just mentioned. Similarly, short contacts to a metal atom can as well be made by C–H groups not directly bound to the metal, but in β, γ, δ or φ positions, usually belonging to phenyl, isopropyl, or *tert*-butyl groups of coordinated ligands. There seems, however, to be no correlation whatsoever between the number of intervening bonds between the M and H atoms and the interpenetration of their van der Waals crusts.

The structures that appear in Fig. 19 with a small negative or positive difference between M···H and M···C interpenetrations constitute probably the best examples of C–H σ-bond coordination. For instance, in $[ClPt(^t$Bu-py-PhF$)]$[126] (point III in Fig. 19a), a distal methyl group of the *t*-Bu substituent of a coordinated pyridine contacts through a CH_2 group the square planar Pt atom at an empty coordination site (Fig. 20a), with H···Pt and C···Pt penetration indices of 74 and 82%, respectively, as expected for a σ-bond coordination **2** ($p_{MH} - p_{MC} = -8\%$). This situation is similar to that found computationally by Bickelhaupt and coworkers[102] in the initial complex formed by

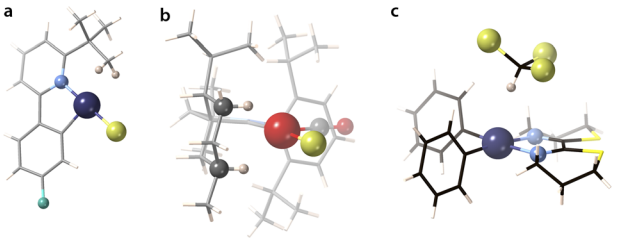

Fig. 20 Structures showing (a) a $CH_2\cdots Pt$ contact[126] with predominant C···Pt penetration (xampuy, −8% diff.), (b) two κ^1–C–H···Rh contacts[129] with predominant H···Rh penetration (cefcia, 15% diff.), and (c) C–H···Pt hydrogen bond between a chloroform molecule and a square planar Pt^{II} complex (kekzab, 24% diff.).[130]

a Pd atom and a methane molecule as the first step in an oxidative addition of a C–H bond. In that complex, the $CH_2\cdots Pd$ group has H···Pd and C···Pd penetration indices of 77 and 75%, respectively.

Another prototypical example is that of $[(dmpe)_2TiCl_3–CH_2–CH_3]$ (point IV in Fig. 19a),[127] in which the β carbon atom of the coordinated ethyl group is at 2.50 Å of Ti, and the corresponding H atom is at 2.06 Å, yet the penetrations of the two atom pairs are practically identical and high enough as to consider them both bonded in a σ C–H bond coordination mode **3**. A similar situation is found for weakly bound propane molecules at open coordination sites of Fe atoms in a MOF (point V in Fig. 19a),[128] with a slightly predominant Fe···H penetration ($p_{MH} - p_{MC} =$ 10%).

Among the coordinated σ C–H bonds, a particularly interesting family of Rh complexes has been made by A. Weller and coworkers[131] (Fig. 19b and c). In those compounds, the σ-bond coordination is not a secondary interaction, but the alkyl groups are coordinated only through the C–H bonds, occupying specific coordination sites (**4**). The alkyl-metal bonding has been nicely described by NCI (non-covalent interactions) plots and NBO donor–acceptor analysis.[132] They were obtained *via* a single crystal to single crystal reaction in which a diene precursor is reduced with H_2, resulting in coordinated alkanes that include cyclooctane, 2,3-hexane, norbornane, or pentane, with a variety of hapticities. As an example, in the Rh complex with 3-methylpentane (triangles in Fig. 19a),[133] whose structure is schematically shown in Fig. 19c, one methylene group is coordinated through its three atoms (Rh–H penetrations 83% and Rh–C penetration 88%), while another methylene is coordinated predominantly through the H atom ($p_{RhH} - p_{RhC} =$ 20%). A related Rh complex in which a cyclohexyl group is attached to a carbene ligand is coordinated through two C–H bonds (shown in Fig. 20, point VI in Fig. 19a).[129]

Finally, we have a clear example of hydrogen bonding with a transition metal (Fig. 20c) in a chloroform adduct with a square planar Pt complex (point VII in Fig. 19a).[130] In this, the $CHCl_3$ molecule establishes a contact at a Pt···H distance of 2.589 Å (penetration index of 56%) in an axial position (Fig. 20c), with a Pt···H–C angle of 169°.

In summary, a representation of the M···H and M···C penetration indices as a function of the incidence angle of the C–H bond, even if showing a poor correlation, allows us to draw several conclusions: (i) the M···H penetration increases as the incidence angle tends to 180°, while the M···C penetration varies very little with that angle; (ii) so far, the highest M···H penetrations are close to 100%, and correspond to the cyclooctane,[134] norbornane[135] and cyclooctane[134] Rh complexes and an Os complex[136] with two phenylic C–H groups occupying two sites of the coordination octahedron, all with coordination mode **4**; (iii) those high M···H penetrations appear at Rh–H–C angles larger than 110° and predominate over the M···C penetrations that are below the 75% mark; (iv) for incidence angles below 100° the M···H and M···C penetrations are similar, as is the case of the *n*-hexane[132] and *n*-pentane[123] rhodium complexes. The structures shown in Fig. 20, thus, represent snapshots along the path from hydrogen-bonded alkanes to σ C–H coordinated alkanes. It must be stressed that the structures aligned along the path shown in Fig. 20 correspond to a wide variety of transition metals: Ti, Cr, Fe, Co, Ni, Mo, Ru, Rh, Os, Ir, Pd, and Pt.

Dihydrogen *vs.* dihydride coordination and Si–Si bond coordination

The H–H bond in H_2 can also coordinate to a Lewis acid through its two electrons, as first reported by Kubas.[137] For σ-bonded dihydrogen, Kubas characterized several steps along the oxidative addition reaction of a dihydrogen molecule to a metal atom, which starts with the formation of a dihydrogen complex that may evolve to a dihydride complex in five successive steps, by stretching the H···H distance.[138] Due to the usual uncertainty in the position of hydrogen atoms near heavy atoms associated with X-ray structural determination, a great deal of computational studies[139] as well as neutron diffraction structure determinations of deuterated samples has been devoted to this family of compounds.[140]

Concerning the different situations described by Kubas (**5**), from a free dihydrogen molecule to a dihydride complex resulting from oxidative addition, since we are comparing in all cases the same pair of interacting atoms, the H–H distance and the p_{HH} penetration index are equivalent. However, the penetration index provides us with an added meaning that is not as easily appreciated with raw interatomic distances. Notice, for instance, how the interpenetration of the two hydrogen crusts goes from nearly 100%, indicative of the covalent bond in free H_2, to a weaker bond in the η^2-coordinated dihydrogen, to a final 45% value in the dihydride complex, comparable to that found for the two *gem* hydrogen atoms in methane (35%).

The oxidative addition pathway proposed by Kubas (**5**) is beautifully expressed as a correlation between the H···H and M···H penetration indices found in the structures determined by neutron diffraction (Fig. 21a), despite the variety of metal atoms considered (Fe, Ni, Mo, Ru, and Os). In contrast, the data from X-ray structures show no correlation, most probably due to the uncertainty in the H atom positions determined with this technique.

We have also analyzed the coordination of Si–Si bonds to transition metals,[141–144] and found them to follow a similar trend

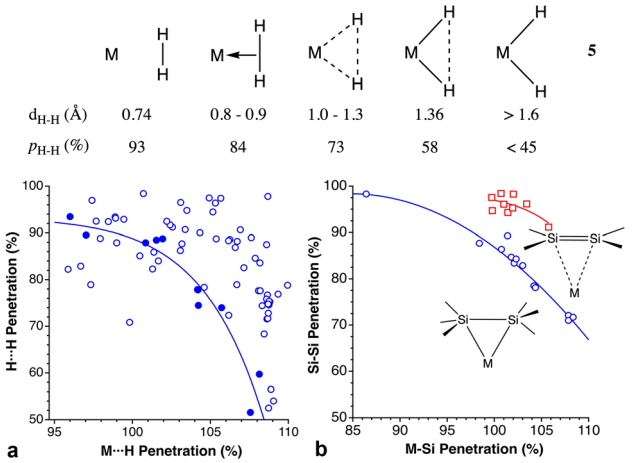

Fig. 21 (a) Relationship between the M···H and H···H penetration indices for all structures of transition metal M(η^2-H_2) fragments determined by X-ray diffraction (empty circles) or by neutron diffraction (filled circles). The continuous line is a least squares fitting to the neutron diffraction data only. (b) Relationship between the Si–Si and M–Si penetrations in compounds with σ-coordinated Si–Si bonds (M = Ni, Pd, Mo, Cu; circles) and in the π-coordinated disilenes found in the CSD (squares). Data are provided in ESI, Table S17.‡

to the σ-bonded dihydrogen molecule (Fig. 21b) even if different metal atoms are included in the same plot. The outlier corresponds to a Mo compound in which three σ bonds, H–Si–Si–H are involved in a donation to the metal atom, with the coordination of the H atoms presenting a slightly higher penetration to Mo (100 and 110%) than the Mo–Si ones (97 and 107%). It is interesting to compare these penetration indices to those of π-bonded silene complexes, in which for the same M–Si penetration, the Si–Si penetration is about 12% higher. The Si–Si single bonds in the CSD, on the other hand, present a distribution of penetration indices centered around 93.7% (Fig. S4 in ESI‡).

Hydrogen bonds

Despite the variety of hydrogen bonds and their importance in chemistry and biology, their typologies and energies are usually grouped into three families.[145–147] Thus, hydrogen bonds are termed moderate if they resemble those between water molecules (one could also call them "normal"), and have associated energies in the range of 4–15 kcal mol^{-1}. Hydrogen bonds with energies above and below this range are termed strong and weak, respectively.

In a first exploration of the penetration between the hydrogen atom and the acceptor in a D–H···A hydrogen bond, we have analysed the probability density of penetrations for several combinations of hydrogen donors and acceptors: D = O, N and A = N, O, O═C, S═C, Cl and Br. As examples, we show two plots in Fig. 22, where we can appreciate both the similar probability maxima and the much wider dispersion for the case of the O–H···Cl than for the O–H···O bonds.

Grabowski and Sokalski[148] reported calculated dissociation energies for a variety of hydrogen-bonded pairs of molecules

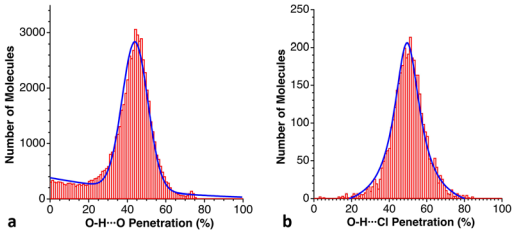

Fig. 22 Distribution of the penetration indices for O–H···A hydrogen bonds with (a) A = O and (b) A = Cl, with maxima at 43 and 46%, respectively (see ESI, Table S18).‡

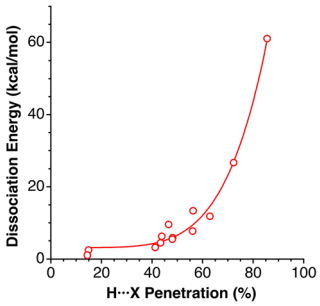

Fig. 23 Dissociation energies of hydrogen-bonded complexes comprising H···O, H···N, H···F, H···C and H···H contacts reported by Grabowski and Sokalski,[148] represented as a function of the corresponding penetration indices (see ESI, Table S20).‡

that include X···H atom pairs (X = F, O, N, C, and H). Those energies correlate nicely with the corresponding penetration indices (Fig. 23), despite the number of atoms involved in those hydrogen bonds.

Among the so-called classical hydrogen bonds, let us focus on N–H···Cl contacts. Their distribution peak has a sharp maximum at 42% and a tail at smaller values attributable to weaker interactions. If we limit the search to chloride anion interacting with alkylammonium cations, $R_3NH\cdots Cl$ (6224 data), the penetration distribution (Fig. 24a) can be fitted (disregarding the data of the tail with p < 30%) to a Lorentzian function with its maximum at 45.2%. If we now compare that distribution with those of the other halides, the maxima for F, Br, and I appear at 49.9, 39.9 and 33.4%, respectively (Fig. 24b).

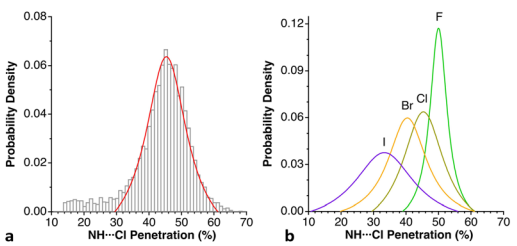

Fig. 24 (a) Distribution of the H···Cl penetration index for hydrogen bonds with alkylammonium cations, showing the fitting to a Lorentzian function. (b) Distribution of the N–H···X penetrations in hydrogen bonds between alkylammonium cations and halogen atoms (see ESI, Table S19).‡

These values decrease linearly as we go down the group, (p_{HX} = 61.3–5.48 n_X; r^2 = 0.99, where n_X is the period of X; data are given in Table S19‡).

The large crown ether 18-crown-6 (ref. 149) and derived macrocycles, such as the disilyl derivatives,[150] are well known to capture cationic species. In the case of the hydronium cation, H_3O^+, that makes three crystallographically independent H···O contacts in 11 data sets from 6 compounds, with penetration indices in the range 39–60%, the shortest contact in each adduct penetrates in all cases more than 48%, *i.e.*, among the highest values found for O···H–O hydrogen bonds (Fig. 24a), most likely due to the ionic nature of the hydrogen donor. For comparison, in related potassium clathrates of the same crown ether, the K···O interpenetration is in most cases higher than 80%, with a maximum probability density at 9% (Fig. S5 and Table S25, ESI‡), undoubtedly associated with the added contributions of donor–acceptor and ion-dipole interactions. In a different family of macrocycles, we find that protonated forms of trimethyl-triazacyclononane form intramolecular N–H^+···N hydrogen bonds with p = 33–42% (compared to 105% in the N–H^+ bond), similar to the values found for non-protonated N–H···N hydrogen bonds.

The F–H···F^- interaction is considered to be one of the strongest hydrogen bonds.[147] If we disregard those structures in which one or two fluorine atoms are bonded to another element, we are left with the FHF^- anion that can be found with a symmetric structure with F–H penetrations of 80 ± 1% in the gas phase,[151–153] in the solid state in its potassium salt[154] and the same salt cocrystallized with IF_5,[155] and in solution.[156] But it also appears in several organic crystal structures in the CSD with one short and one long F–H distance. A scatterplot of the two penetration indices (Fig. 25a) shows the existence of many structures in which one F–H bond (penetration ≈100%, to be compared with 98% in gaseous HF[157]) coexists with a long H···F contact (penetrations of 40–60%), and as the contact becomes more penetrating the bond is weakened, until reaching the symmetric structures in which the two penetration indices become identical, around 85%. The whole set of structural data thus represents snapshots along a proton transfer process between the two fluorides, F–H···F^- → F···H–F^-. We call the attention of the reader to the fact that the penetration between the two fluorine atoms is not negligible at all, in most cases between 20 and 45%, consistent with the observation of Dereka *et al.*, that it is better characterized as a hydrogen-mediated donor–acceptor bond.[156] In Fig. 25a we show how the van der Waals crusts of the two fluorine atoms interpenetrate in a symmetric F···H···F^- anion.

The H_2O^+–H···OH_2 cation also forms strong hydrogen bonds,[147] comparable only to those in the just discussed H–F···H^+ group and to the F–H···O interactions. This is found in solid state compounds with chloride,[158] bromide[159] or nitrate[160] as counterions and also in a host of organic anions. As for the case of the F···H···F^- groups, there is a wide variation of the two O–H penetrations, which also seem to be correlated in such a way that when a water molecule gets at shorter distances of the hydronium cation, the approaching O–H bond becomes longer (Fig. 25c), up to the point at which the two distances become identical. The dispersion seen in Fig. 25c is attributed to the poor determination of the hydrogen atom positions in the X-ray structures, as corroborated by selecting only those structures with an agreement factor $R \leq 2.5\%$. It must be noted that for small H···O penetrations the O–H bond is practically unaltered, as indicated by a plateau in Fig. 25c, and only for penetrations above 60% does it start to elongate in practically the same way as in the F–H···H^- case (Fig. 25a). An interesting feature of the distribution of the penetrations of the two O–H interactions (Fig. 25d) is the existence of two maxima corresponding to the H_2O–H^+···OH_2 and H_2O···H^+···OH_2 cases (at ∼110 and 88%, respectively), that suggest that there are three potential energy minima in an H_2O–H^+ + OH_2 → H_2OH + H^+OH_2 proton transfer process, which might proceed through a symmetric intermediate. The linear stretch of the proton transfer in the two systems, FHF^- and H_2O–H^+–OH_2, can be jointly fitted to a linear equation: $p_{H\cdots X} = 149.0 - 0.735\ p_{X-H}$, where X is F or O ($r^2$ = 0.95).

The distribution of penetration indices found for 21 types of hydrogen bonds is summarized in Fig. 26. The C–H···F, C–H···O, C–H···N and C–H···S interactions, considered to be weak hydrogen bonds,[146,161] are indeed the ones that present the lowest penetrations (Fig. 26). In the case of C–H···N contacts, the distribution of penetrations due to weak noncovalent interactions starts below 20% and constitutes a shoulder of the much abundant random distribution of atom pairs at about −22%. The abundant C–H···S hydrogen bonds have been the object of a detailed structural analysis recently.[162] It was concluded that such interactions show a geometric preference for angles larger than 155° and distances between 2.83 and 3.13 Å. A similar analysis carried out by us from the point of view of

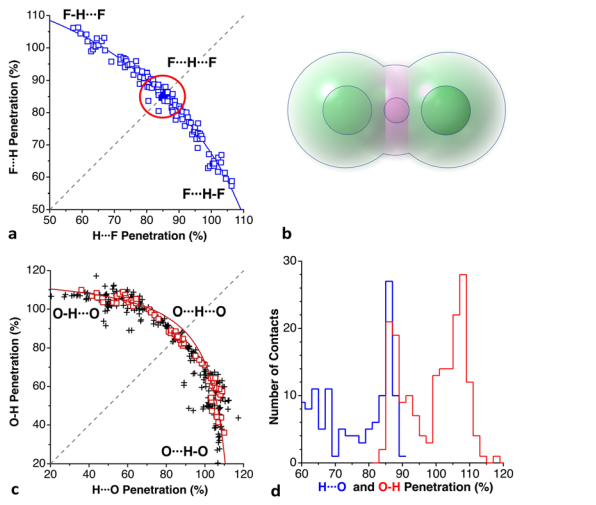

Fig. 25 (a) Correlation between the penetrations of the two F–H contacts in a F–H–F^- anion. (b) Representation of the valence and van der Waals spheres in the F–H–F^- anion[154] (c) Correlation between the high and small H···O penetrations in H_2O···H^+···OH_2 groups (squares correspond to crystal structures with $R \leq 2.5\%$). In a and c the dashed lines correspond to symmetric structures with two identical X–H penetrations, where X = F and O, respectively. (d) Distribution of the penetration indices in the long and short O–H contacts in H_2O···H^+···OH_2 groups (see ESI, Table S21).‡

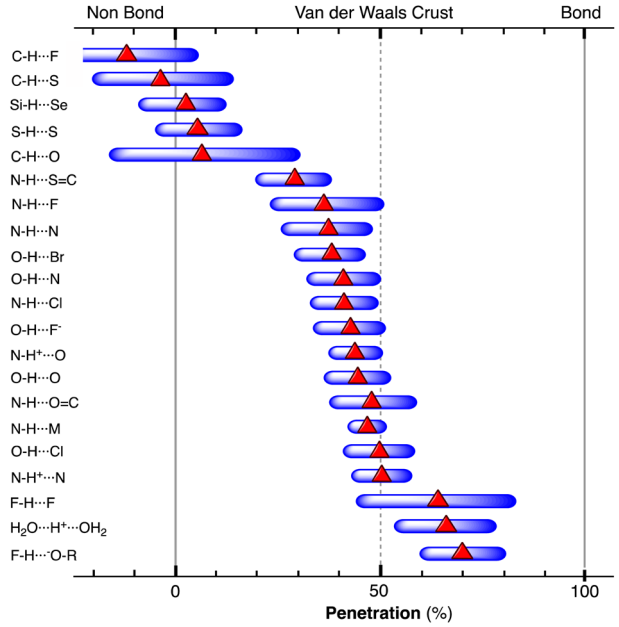

Fig. 26 Ranges of penetration indices presented by several types of hydrogen bonds (blue bars) represented by the width of the Lorentzian curve obtained by least squares fitting of the probability density distribution, and the position of the maximum of the probability density (red triangles). Data are provided in ESI, Tables S18–S21.‡

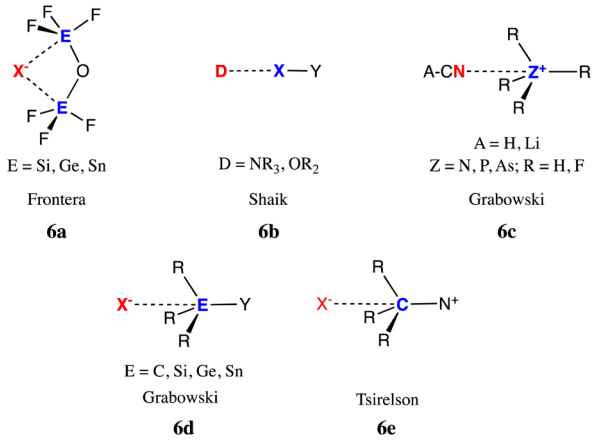

Chart 3 σ-Hole interactions studied by different groups and discussed in this section in terms of their penetration indices. The σ-hole-bearing atom and the donor atom are in boldface, and X and Y represent halogens in all cases.

the van der Waals crust interpenetration yields a distribution of the S···H penetration indices with a maximum at −7% that reaches values up to 25%, comprising contacts reported by Fargher *et al.*[162] (−2 to 15%) in a narrower range of angles. Keil *et al.* called attention to intramolecular Si–H···SeR_2 interactions at H···Se distances between 2.71 and 2.91 Å,[163] that correspond to penetrations of 6–19% (Table S21, ESI‡), well within the range found for intermolecular H···Se contacts (Fig. S6, ESI‡), distributed between −20 and +30%, with a maximum probability density at 2%.

Halogen and other σ-hole bonds

In a study of the directionality of σ-hole intermolecular interactions, Bickelhaupt and co-workers introduced the idea that they should not be considered as a simple electrostatic attraction between the charge distributions of two independent molecules, but that there is a substantial interpenetration of those charge densities.[164] Our present proposal of using penetration indices for the analysis of this class of noncovalent interactions is in line with their conclusion that there is a significant stabilizing component stemming from HOMO–LUMO interactions, *i.e.*, from the interpenetration of the valence spheres. As a first attempt at applying penetration indices to the study of σ-hole interactions, we have selected three families of adducts studied computationally by different authors and looked at their binding energies and other calculated data such as the components of the binding energy obtained from energy decomposition analyses (EDA) or the electron density at the bond critical point (bcp) obtained by the atoms in molecules (AIM) approach.

The families selected for this study are shown in Chart 3. First, we discuss the family of adducts in which a four-coordinated atom of the periodic group 14 (E in **6a**) interacts with a Lewis base that can be a halide or a group 16 compound, forming anionic or neutral adducts or "tetrel bonds", respectively, exemplified by the systems computationally studied by Frontera and co-workers.[165] The second group is formed by the adducts studied by Shaik and co-workers (**6b**),[166] in which a σ-hole of a halogen or interhalogen molecule Y–X interacts with a Lewis base such as ammonia or water, often called "halogen bonds". Then we look at "pnictogen bonds" of type **6c** in neutral adducts with NCH or NCLi as Lewis bases and analogous anionic adducts with a halide ion acting as the Lewis base, studied by Grabowski.[167] Finally, we consider the families of ion-molecule (**6d**)[167] and ionic-pair (**6e**)[168] interactions involving a group 14 atom.

The **6a** family, which comprises the nine structures with $X^-\cdots E$ interactions (X = F, Cl, Br; E = Si, Ge, Sn) reported by Frontera and coworkers,[165] shows a strong dependence of interaction energies on the penetration index for each set of interactions with the same halide (Fig. 27a) which can be fitted as a function of the *n*th power of the penetration index *p* (eqn (6)), where E_0, *a* and *n* are fitting parameters. Although E_0 is the value of the interaction energy at a small penetration, typically a large negative value of *p*, such extrapolation may not always be significant, given the sensibility of that fitting parameter to the values of the interaction energy for the points at low penetrations and the small number of points available. On the other hand, considering all the halide adducts together, a similar expression also provides a fair representation of the behaviour of the nine different combinations of E and X. Notice that for the same group 14 element E, the penetrations increase in the order Br ≤ Cl < F and the absolute values of the interaction energy follow the order Br < Cl << F. Conversely, for the same

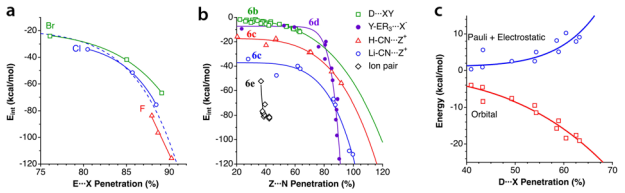

Fig. 27 (a) Dependence of the $X^-\cdots E$ binding energy (X = F, Cl, Br; E = Si, Ge, Sn) on the penetration indices for σ-hole bonds in adducts **6a** studied by Frontera and coworkers.[165] The dashed line corresponds to the least squares fitting for all the compounds. (b) Dependence of the interaction energy of adducts **6b** at their energy minima (squares)[166,169] of $R_3Pn{-}X^+$ ions with NC–H (triangles) and NC–Li (empty circles; X, R=H or F; Z = N, P, As) **6c**,[167] $R{-}EY_3\cdots X^-$ adducts **6d** (solid circles),[169] and ion pairs **6e** (filled squares)[168] on the penetration index. (c) The electrostatic + Pauli and orbital interaction components calculated by Wang *et al.*[169] for adducts **6b**, represented as a function of the D–X penetration. Data are provided in the ESI (Table S22).‡

halogen atom, both the penetration and interaction energies follow the trend Si < Ge < Sn.

$$E_{\text{int}} = E_0 - a \cdot p^n \tag{6}$$

The second set of intermolecular interactions **6b**, studied by Shaik and coworkers[166,169] comprises adducts of type D···X–Y (E = N, O, C=C; R = H, Me; X = halogen, Y = halogen or NO_2). First, we see (Fig. 27b) that the calculated binding energy presents a practically linear correlation with the penetration index, despite the varied combinations of atom pairs considered. It is also seen that the correlation exists regardless of the level of approximation used in the calculations, full valence bond theory (VBT) or the less costly version with block localized orbitals (BLOs).

The σ-hole bonding involving A–CN···Z interactions **6c**, where Z is a pnictogen atom and A can be H or Li, computationally studied by Grabowski,[167] also shows a dependence of the binding energy on the penetration index (Fig. 27b) but for penetrations higher than 60% there is a much stronger enhancement of the interaction energy, with a parallel behaviour of the two families (A = Li or H). Two of these systems, $PF_4^+\cdots$NC–Li and $AsF_4^+\cdots$NC–Li, reach penetrations close to 100%, consistent with the adoption of a nearly trigonal bipyramidal geometry of the ZF_4N group, and we have verified that there is a correlation between the penetration index and the N–Z–R bond angle for Z = pnictogen (**6c**), thus describing an SN_2 pathway. If we compare this behaviour with that of the **6b** series, we see that they cover a similar range of penetration indices but with much higher binding energies, a fact that can be explained based on the ionic nature of the pnictogen-containing species in this case. On the other hand, a comparison with the behaviour of adducts **6a** (Fig. 27a) shows similar ranges of binding energies, both corresponding to interactions between a neutral molecule and an ionic species, but a much wider range of penetration indices is covered by **6c**, due to the formation of trigonal bipyramidal structures. Despite the differences between the three groups of adducts, all of them can be seen as following a similar type of relationship between the interaction energy and the penetration index of the two interacting atoms, expressed as eqn (6). Moreover, the family **6e**, in which the interaction is between two ions of opposite signs,[168] shows much stronger interaction energies at relatively low penetration indices.

By looking at the results of the energy decomposition analyses (EDA), we can also observe (Fig. 27c) a nice dependence on the penetration indices of both the repulsive (or slightly attractive) combination of electrostatic and Pauli components and the attractive orbital component. Three outliers in that plot correspond to the interactions between a fluorine molecule and the $Me_nH_{3-n}N$ molecules; two are not shown in the figure. We suspect that such a different behaviour at short N···F distances is due to the presence of additional $N{-}CH_3\cdots F$ attractive interactions. In fact, in the gas phase structure of $Me_3N\cdots F_2$ the C···F distances[170] represent a penetration index of 23%. Such a hypothesis is further supported by a linear dependence of the N···F penetration on the number of methyl substituents.

Let us note in passing that the computational study of the interaction between halogenated molecules and the Xe atom of an electron probe microscopy tip discussed in Section 2.5 and Fig. 12 offers another example of a successful application of penetration indices to noncovalent halogen bonds.

In summary, we have calculated the penetration indices for a variety of halogen bonds studied by three different groups[166,168,171] and found them to be all between 11 and 65%. We can thus provisionally conclude that such a range of values is characteristic of halogen bonds, while the penetrations obtained for tetrel and pnictogen bonds correspond to stronger interactions in which there is an additional ion-dipole contribution with varying degrees of formation of a bond in a hypercoordinated species. Still more interesting are the 26 different σ- and π-hole interactions studied by Murray and Politzer,[172] that include halogen-, chalcogen-, pnictogen- and hydrogen-bonding, and follow a dependence on the penetration index similar to the one shown in Fig. 27a (see ESI, Fig. S7‡).

One- and three-electron σ bonds

The existence of one- and three-electron bonds was proposed by Pauling almost a century ago.[173] The dihydrogen cation H_2^+ is the simplest molecular system showcasing a one-electron bond and has historical relevance because it was amenable to a solution of the Schrödinger equation.[174] Its interatomic distance determined in the gas phase is 1.058 Å,[175] that corresponds to a penetration index of 75%, short of the 100% expected for a two-electron bond, yet with a significative degree of penetration of the van der Waals crusts. A somewhat smaller penetration is found for the ground states of LiH^+[176] and Li_2^+, but still well beyond the midpoint of the van der Waals crust (65 and 67%, respectively). We compare this with the two-electron bonds in the analogous neutral species, which show penetration indices in the 90–100% range, as schematically represented in Fig. 28.

If we turn our attention now to the cationic dimers of noble gases, Ng_2^+ (Ar–Xe$^+$, Kr–Xe$^+$, He–He$^+$, and Kr–Kr$^+$), with 3 σ electrons, we find penetration indices in the range 48–80%, *i.e.*, at least 15% less than that of the H–X and C–X two-electron

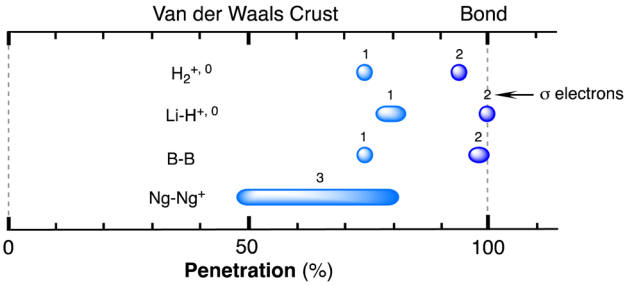

Fig. 28 Ranges of penetration indices found for several diatomic species with one-, two-, or three- σ-electron bonds. Ng stands for a noble gas. Data are provided in the ESI (Table S23).‡

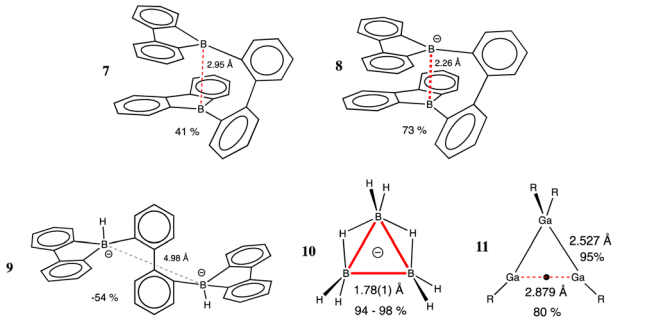

Chart 4 Examples of compounds containing boron–boron intramolecular "contacts" with widely varying degrees of the interpenetration of the van der Waals crusts (**7**–**10**), and a gallium compound with a one-electron σ Ga–Ga bond (**11**). Penetration indices are given as percentages.

bonds (Fig. 29). The much larger variability of the penetration indices in the Ng_2^+ ions seems to be correlated with the Mulliken electronegativity difference between the two elements. Such an electro-negativity dependence can be considered responsible for the quite low interpenetration found in the He–Kr^+ species (3.060 Å,[177] p_{HeKr} = 19%). For comparison, we also show in Fig. 29 the effect of the electronegativity difference on the degree of penetration of the atoms involved in the D–X bond in deuterium halides in the solid state[178–180] and of the sp^3 C–X bonds in the CSD. The single bonds appear in a region of penetrations of around 100%, compared to the maximum value achieved by the half-bonds (80%). In addition, there is a less pronounced but clear dependence on the electronegativity difference, with the penetration index decreasing as the electronegativity difference increases.

An illustrative example of more complex molecules in which penetration indices may conveniently differentiate non-coordinated from one- and two-electron σ bonds is provided by 5,5′-biphenyl-2,2′-diylbis(5*H*-dibenzo[*b*,*d*]borole and its anion (**8** in Chart 4). The pristine neutral molecule adopts the *syn* conformation shown in **7**, which places one boron atom on top of the other, at 2.95 Å,[181,182] with a degree of interpenetration p_{BB} of 41%, pointing to some sort of weak interaction, similar to that found in a phenanthroline diborole (p_{BB} = 38%).[183]

One-electron reduction of **7** yielded compound **8** which was characterized by EPR and X-ray crystallography, showing a shorter B–B distance of 2.265 Å (p_{BB} = 73%). Such a shortened distance must be attributed to a one-electron B–B σ bond.[184] In the dianion **9**, with coordinatively and electronically saturated B atoms, they are well separated, at p_{BB} = −54%. For comparison, the single B–B bond found for Br_2B–BBr_2 in the gas phase (1.689 Å)[185] and those that appear in 20 structures (30 crystallographically independent molecules) of the triangular $B_3H_8^-$ anion (**10**) have all penetration indices in the range 94–98%. Those degrees of B–B penetration are seen to be similar to those of the simpler one- and two- σ-electron molecules just discussed (Chart 4).

The Ga_3R_4 radical[186] has the shape of an isosceles triangle with two sides corresponding to Ga–Ga single bonds (**11**) and the third one forming a longer one-electron σ-bond, the penetration index decreasing from 95 to 80%. Notice the similar degrees of penetration shown by the B–B and Ga–Ga one-electron bonds in **8** and **11**, respectively. To provide a broader picture, we plot in Fig. 30 the ranges of penetrations in structures found in the CSD (Table S23 in the ESI‡) for single, double and triple Al–Al and Ga–Ga bonds, as well as compounds with formal Al–Al[187] and Ga–Ga[188,189] bond orders of 1.5.[188,189]

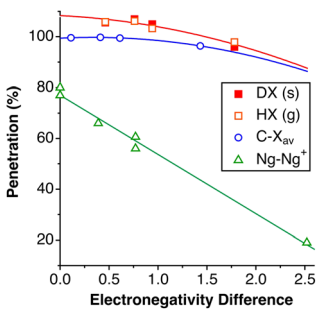

Fig. 29 Dependence of the penetration indices of the Ng–Ng^+ half bonds and the deuterium-X and Csp^3–X single bonds on the difference of the electronegativity of the two bonded atoms. Ng stands for noble gas, and X for a halogen; data from the gas phase are shown with empty symbols, and from the solid state with filled symbols. Data are provided in the ESI (Table S24).‡

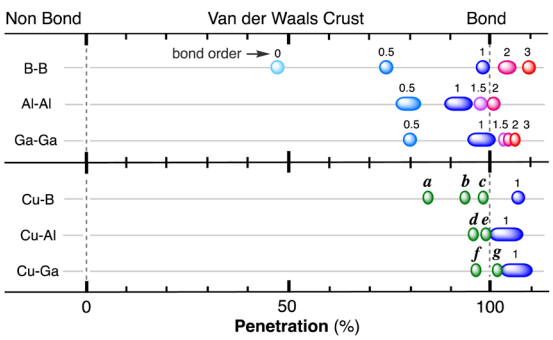

Fig. 30 Map of penetration indices for some group 13 homonuclear pairs with bond orders from 0 to 3 (above) and for Cu–E pairs in compounds **12** and **13** (below, E = B, Al, Ga). Numerical data are provided in the ESI (Table S23).‡ **a**, **b** and **c** represent the three species $[Cu(TPB)]^n$, with n = +1, 0 and −1, respectively; **d** and **f** refer to compounds **13** with M = Al and Ga, respectively, and **e** and **g** refer to the cationic complexes $\mathbf{13}^+$, with M = Al and Ga, respectively.

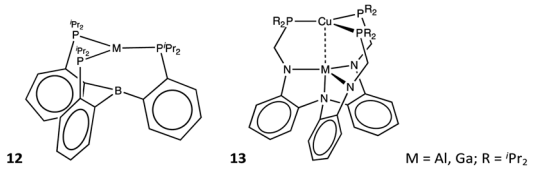

The trisphosphine ligand TPB (tris[2-(diisopropylphosphino)-phenyl]borane) **12** forms complexes with several transition metals: Fe, Co, Ni, Pd, Pt, Cu, Ag and Au.[190–192] As in the case of silatranes discussed below, the molecular topology places the metal and boron atoms at relatively short distances, such that the M···B penetration indices are in the range 72–99%. The metal atoms are in a good position to act as donors to the empty p orbital of boron. A nice fine-tuning of the interaction was achieved by Peters and co-workers *via* the reduction of the Cu(I) complex, characterizing three species $[Cu(TPB)]^{1+,\ 0,\ 1-}$, that present increasing degrees of interpenetration of the Cu and B van der Waals crusts as the charge becomes more negative: 84, 94 and 98% (points **a**, **b** and **c**, respectively, in Fig. 30). Even if the authors assign Cu–B bond orders 0, 1/2 and 1, respectively, we think that these molecules present a three-orbital interaction pattern that involves essentially the z^2 and p_z orbitals of Cu and p_z of B, resulting in a non-negligible degree of Cu → B dative bonding even for the cationic complex, consistent with its high penetration index. For comparison, the one-electron B–B bonds discussed above have penetrations of less than 80% (Fig. 28), those of H_2^+ and LiH^+ are 75 and 65%, while the Me_3N–BF_3 and H_3N–BH_3 adducts have penetration indices of 94–96%, and the unsupported single Cu–B bonds in the CSD, 108(1)%.

The related cationic complexes $\mathbf{13}^+$ reported by Graziano *et al.*[193] feature short Cu···M distances (M = Al, Ga), corresponding to penetration indices of 96 and 98% for Al and Ga (points **d** and **f** in Fig. 31), respectively. Their one-electron reduction results in an enhanced penetration (100 and 104%, points **e** and **g** in Fig. 31, respectively). Again, comparison with the penetration indices of canonical one-electron bonds in LiH^+ and H_2^+ and compounds **8** and **11** (from 65 to 80%) suggests that three, rather than one, electrons are involved in Cu–M bonding in the neutral compounds **13**. We think that the attribution of a one-electron bond character to the Cu–M atom pair is an oversimplification of a more sophisticated bonding scheme along the N–M–Cu molecular axis that involves 5 electrons and up to 6 atomic orbitals (s, p_z and z^2 of Cu, s and p_z of M and the N lone pair orbital).

In these systems, the interpenetration is forced mechanically, *i.e.*, by a rigid framework of covalent bonds that keep two non-bonded or weakly bonded atoms at a relatively short distance, as happens in silatranes, tripod ligands and iron maiden compounds,[194] discussed in other sections of this work. A recently reported $Ni^0 \cdot Ni^I$ half bond[195] has a penetration index of 93.5%, remarkably similar to those found in this section for Cu·Al, Cu·Ga and N·B half bonds.

In a thoughtful account of one-electron bonds,[196] Oliveira de Sousa and Nascimento state that one-electron bonds are not "half-bonds", since the difference in the bond dissociation energies of one- and two-electron bonds has no relation to bond orders. A similar energetic consideration should apply to the comparison of single, double and triple bonds. We note that the penetration of the van der Waals cores shows the same behaviour, and their values for one- and two-electron bonds are much closer to a 1 : 1 than to a 1 : 2 ratio, and analogous conclusions can be drawn upon comparison of the penetration indices of single, double and triple bonds. We note, however, that the definition of a bond order is related to the relative occupation of bonding and antibonding molecular orbitals, and from this point of view, a bond order of one-half should be assigned to both one- and three-σ-electron bonds.

In the (NHC)B≡B(NHC) compounds,[197,198] the B–B bond lengths of 1.45 Å (P_{BB} = 111%) are clearly differentiated from double bonds in the penetration map (Fig. 30). It is interesting to observe that such high penetrations coexist with contacts between the H atoms of the substituents at the carbenes at distances as short as 2.33 Å, or a penetration p_{HH} = 52%, much higher than that found for two interacting methane molecules (−5% or less, depending on the computational method used[199]).

In the host–guest complex of XeO_3 within a crown ether obtained by Schrobilgen and coworkers,[200] the calculated Wiberg bond orders for both the Xe–O bonds and the Xe···O contacts present an interesting correlation with the corresponding penetration indices, reflecting an "all or nothing" situation (Fig. 31). Notice that the correlation represents not only the wide picture of high *vs.* low penetrations but also how the small variations in penetration are correlated with tiny variations in the Wiberg bond orders, as seen in the inset of Fig. 31. It is interesting to note that the same XeO_3 molecule, co-crystallized with pyridine or *p*-(NMe_2)-pyridine[201] presents three X···N contacts at penetration indices (61–68%) not that different from those of the three Xe···O shortest ones in the 15-crown-5 compound (47–52%).

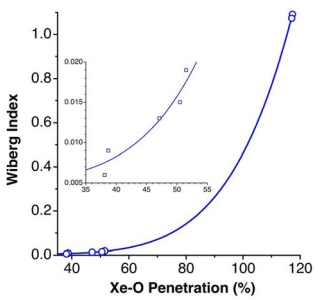

Fig. 31 Relationship between the Wiberg bond order[200] and the Xe–O penetration index in the adduct of XeO_3 with the crown ether 15-crown-5, covering both the Xe–O bonds (large Xe–O penetration indices) and the Xe···O contacts with the five crown oxygens (small penetration indices), shown in an expanded view in the inset (see ESI, Table S25).‡

Electron-deficient bonds

Boranes

Diborane is a prototypical molecule with three-centre two-electron bonds (3c–2e), and it is an inescapable target of our study to calibrate the degrees of penetration that might be characteristic of electron-deficient bonds. In 7 different

structural determinations in the gas phase, the B–H penetrations are 91.3% for the bridging hydrides, compared to 97.4% for the bonds to terminal hydrogen atoms. Interestingly, even if we usually think of (and depict) diborane as having two "banana bonds" covering the two B–H–B groups, we find that the B–B penetration is 96.1%, as high as the B–H ones and only slightly less than the two-electron B–B bonds (Fig. 30). Similar values are found for the organoboron analogues $R_2B(\mu\text{-}H)_2BR_2$: 94(1)% for the B–B and the same value for the B-μH penetrations (49 crystallographically independent data sets from the CSD).

The related electron deficient $B_3H_8^-$ anion (**10** in Chart 4) appears with various countercations in 22 crystallographically independent molecules found in the CSD with the usual restrictions (no disorder, $R \leq 7.5\%$). The average B–B penetration in this family is 94.8(9)%, almost identical to that in diborane, with no significant difference between the bridged and unbridged edges.

It is important to stress that the penetration in 3c–2e bonds is only slightly less than that in two-electron bonds. We think that this fact reflects a similar degree of overlap between valence orbitals of the two atoms required in both cases. A similar finding was mentioned for one-electron bonds. Thus, the different strength of one-electron, 3c–2e, and two-electron bonds reside in the different occupations of a σ-bonding MO (one- and two-electron bonds) or in the molecular topology that facilitates the formation of delocalized bonding between more than two atoms (3c–2e and two-electron bonds).

Two-electron bridging ligands

An important case of electron-deficient bonding is that of a hydride bridging two or more transition metals. The van der Waals crust formalism offers us a unique opportunity to check if one can find a common trend for all transition metals. To give a rough idea of the far-reaching applicability of the penetration indices, we have analysed for this study 8565 crystallographically independent data sets for 32 metals and 6 bonding modes (from non-bridging to μ_6) of hydrido-bridged compounds. The results are represented by plotting the ranges of values found as a function of the number of metal atoms bridged by a hydride (Fig. 32a), where we see a clear tendency to go from a full bond (penetrations higher than 100%) to lower penetrations as the two electrons of the donor are shared by an increasing number of metal atoms, despite the different number of bridged metal atoms considered and the usual uncertainty in the hydrogen atom position in the X-ray structural determinations.

In the case of tetrahedral arrays of four metal atoms with a μ_4 bridging hydride, two distinct cases are found, depending on whether the metal atoms form metal–metal bonds or are essentially held together by the hydride. In both cases, however, the M–H and M–M penetrations show nice linear correlations (Fig. 32b).

A similar analysis has been carried out for carbonyl-bridging compounds, also a highly frequent motif in transition metal chemistry, whence the lone pair of the carbonyl can be shared by two or more metal atoms at edges or faces, or even in the centre of clusters. From 285 148 crystallographically independent data sets of 26 different metals in 4 coordination modes (from terminal coordination to μ_4 bridges) we can deduce the ranges of penetration values for each nuclearity (Fig. 32c). Again, we see a clear tendency to go from a full bond (penetrations of a 100% or higher) in terminal M–CO links to lower penetrations as the two electrons of the donor are shared by an increasing number of metal atoms. The curve for the carbonyl-bridged systems is shifted to higher penetration values than that for the hydrido-bridged ones, undoubtedly an indication of the ability of CO to use both σ and π orbitals for bonding.

To complement this study, it is useful to briefly analyse the case of semi-bridging carbonyl[202] ligands (Fig. 33a), limiting our analysis to the M–C≡O fragments with angles between 160 and 180°. In those M–CO-*m* systems, the penetration of the σ M–C bond in all molecules is higher than that of the C-*m* bond which implies the π system of the carbonyl, with an average difference of 16%. The penetration indices of the O-*m* bond are also around the 100% mark, similar to or slightly smaller than the C-*m* bonds that show a higher dispersion. Metals found at the M

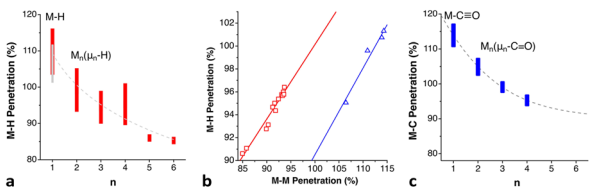

Fig. 32 (a) Ranges of M–H penetration indices for transition metal complexes with a terminal ($n = 0$) and bridging hydride ($n = 2$–6) ligand as a function of the nuclearity n. The superimposed narrower bar for $n = 1$ corresponds to neutron diffraction structures or X-ray structures with a deuteride ligand. (b) Correlation between the M–M and M–H penetrations in μ_4-H tetrahedral tetranuclear complexes with (triangles) and without (squares) metal–metal bonds. (c) Ranges of M–C penetration indices for transition metals with a terminal and bridging carbonyl ligand as a function of the nuclearity n. The ranges are centred at the position of the maximum, and the extent of the bar corresponds to the width at half-height of the Gaussian distribution of the p values. Data are provided in the ESI (Table S26).‡

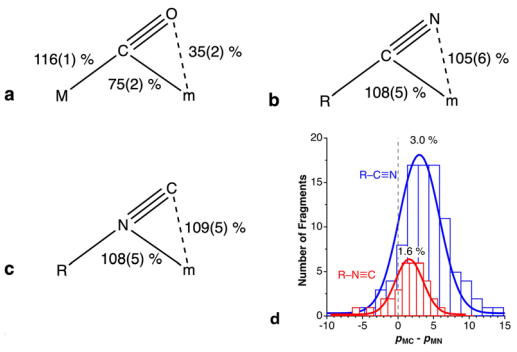

Fig. 33 Ranges of penetration indices for the different bonds in (a) semibridging carbonyl complexes, (b) η^2-coordinated nitriles and (c) η^2-coordinated isonitriles. (d) Distribution of the difference between the *m*-C and *m*-N penetrations in η^2-nitrile (R–C≡N) and isonitrile (R–N≡C) complexes of transition metals. The values indicated at the tip of each peak are the positions of the maxima of Gaussian distribution fittings. Data are provided in the ESI (Tables S27 and S28).‡

position are Ti, Mn, Co, Nb, Mo, W and Re, and at the *m* position Y, Ti, Mn, Zr, Nb and Mo. An exception to the general behaviour just described are the compounds with a purported semi-bridging carbonyl between a Mo atom and a d^{10} ion (Cu^{I} or Ag^{I}),[203] whose *m*-C penetrations are smaller (70–78%) and *m*-O ones much smaller (30–39%) than those in all other cases.

In contrast to the semi-bridging carbonyls, which present an *m*-C penetration 8% higher on average than the *m*-O one, in the η^2-nitrile and isonitrile complexes the *m*-C and *m*-N penetrations (Fig. 33b–d) are rather similar, with the former being on average 2% higher in the nitriles and 1% in the isonitriles. Data are provided in ESI, Table S28.‡

Noble gas – Lewis acid adducts

As the simplest example of donor–acceptor interactions between two neutral fragments, we consider the family of coordinative bonds between a noble gas (Ng) and a d^{10} M–X group, [Ng → M–X], where Ng = Ne, Kr, Ar, Xe; M = Cu, Ag, Au; X = F, Cl, Br, I), for which there is a reasonable amount of structural data obtained in the gas phase.

In Fig. 34 we represent the Ng–M penetration in the [Ng → M–X] complexes as a function of the row of the periodic table of X (*i.e.*, the principal quantum number *n* of its valence shell) for several combinations of noble gas and metal atoms. Such a plot allows us to analyse the effect of each of the three components of this family of molecules: (i) the halide X produces a significant *trans* influence on the Ng–M bond, whose penetration decreases linearly as we descend the halogen group, from F (98%) to I (92%), most clearly seen for the Ar → Ag–X series. (ii) Changing the noble gas from Ar to Kr affects little the degree of penetration for the same M–X fragment, with only a slight increase (of about 2%), even smaller than that effected by changing the halide. However, on going from Kr to Xe there is a larger increase in the penetration (around 7%). (iii) Surprisingly, the effect of the transition metal atom follows the opposite trend from that of the noble gas, with the penetration significantly decreasing as we descend the group from Cu to Ag (6–10%) and slightly increasing from Ag to Au (around 2%), undoubtedly related to the slightly smaller atomic radius of Au compared to Ag, due to the lanthanide contraction.

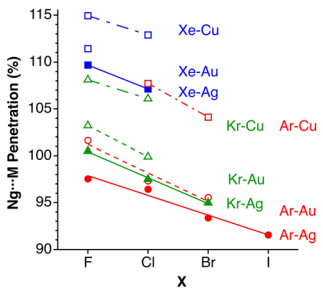

Fig. 34 Penetration indices of the Ng–M bonds in Ng–M–X complexes in the gas phase (Ng = Ne, Ar, Kr, Xe; M = Cu, Ag, Au; and X = F, Cl, Br, I), represented as a function of the period of X. Data provided in the ESI (Table S29).‡

Silatranes, germatranes and [1.1.1] propellanes

Silatranes and germatranes

Silatranes are tripod-like molecules with the topology shown in **14–15**, in which the pivotal nitrogen atom can be at varying distances from a group 14 atom (X), formally establishing an N → X donor–acceptor bond that makes X five coordinated, or keeping N and X at a longer distance, with X presenting a tetrahedral geometry and N retaining its lone pair with a pyramidal structure. Although there are multiple variations of the basic scheme shown here,[204] the most common examples are silatranes (X = Si and Y = O), azasilatranes (X = Si and Y = NR) and germatranes (X = Ge and Y = O).

In these compounds, however, the X···N distances cannot be too long due to the geometrical constraints of the tricyclic system and, correspondingly, the penetration indices cannot be too small. In the set of structures of sila- and germatranes retrieved from the CSD and gas phase structures from the MOGADOC database, we obtain a wide dispersion of penetration indices, between 14 and 98%. Such a wide interval no doubt includes molecules with and without X···N bonding interactions, so we opted for simultaneously calibrating the degree of pyramidalization of the X atom, defined as the C–N···X angle (α), which should be close to the tetrahedral angle (109.4°) when there is an N–X bond, but significantly smaller in the absence of a bonding interaction, reaching values below 90° for molecules in the exo conformation (**16**).

A scatterplot of the two parameters (Fig. 35a and b) shows that the Si and Ge compounds have the same behaviour, with a nice quadratic correlation between the C–N···X angle and the

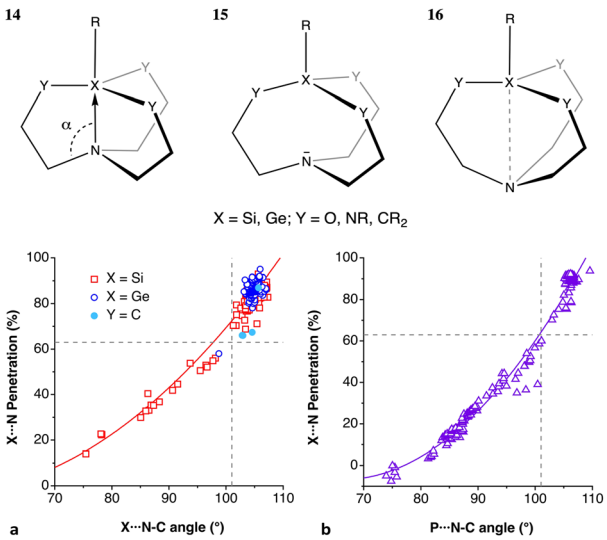

Fig. 35 Scatterplots of the X···N penetration indices and the average X···N–C angle for (a) silatranes (X = Si), germatranes (X = Ge) and (b) fosfatranes (X = P). The least-squares curves are fittings to all the data shown in each plot; the dashed lines delimit the regions with X–N bonds (upper right section) and with varying degrees of X···N non-covalent interactions (lower left section). Data are provided in the ESI (Table S30).‡

N···X penetration. Moreover, we can clearly distinguish two sets of structures: those with angles in the range 75–98° have penetration indices of 14–58%, corresponding clearly to molecules with no N–X bond, whose X and Si van der Waals crust interpenetrations are small enough to qualify for a bond, but large enough to produce some degree of orbital interaction that could compensate for an enhanced Pauli repulsion at such relatively short distances. The second set of points, much more abundant, cover the ranges 101–107° and 66–98% for the C–N···X angle and the N···X penetration index, respectively, clearly indicating the presence of an X–N bond. Looking now at the related fosfatranes (Fig. 35b), we find a similar behaviour and the common limit for the bonding regime corresponds to the values p_{XN} > 63%, X···N–C > 101° (data provided in ESI, Table S30).‡

[1.1.1]Propellanes and bicyclo[1.1.1]pentane

In the family of bicyclo[1.1.1]pentane derivatives (**17**) the two apical carbon atoms are constrained at a relatively short distance of 1.90(2) Å (average of 216 data sets from X-ray structures) by the bridging CR_2 groups. Although no bond can be formally assigned between those two atoms, the interpenetration of their van der Waals crusts is large, with an average index of 81(1)%, comparable to the typical values in one-electron bonds discussed above. In contrast, the related [1.1.1] propellanes (**18**), despite the unusual coordination of the apical carbon atoms, present a much higher average penetration index of 99.7 (3)% (11 data sets from X-ray crystal structures), as one would expect for a regular single bond between tetrahedral carbon atoms. Interestingly, the peripheral C–C bonds are very similar in the two cases, with penetration indices of 100(3) and 98(4)% in **17** and **18** respectively. The distribution of penetration indices (Fig. 36) shows a binary situation with a gap separating the structures with and without an axial C–C bond. It is also to be noted that the wing and central C–C bonds in propellane, which are described according to valence bond calculations as having different bond types, covalent and charge-shift, respectively,[205] have identical interpenetration of the van der Waals crusts of the bonded atoms.

We have shown earlier that [1.1.1]propellanes and bicyclo [1.1.1]pentanes are members of a wider family of compounds that comprise trinuclear transition metal complexes with two μ_3 bridging ligands in an M_3X_2 core.[206] Among those compounds, the propellane-like structure (**17**) with a short X–X distance appears when the number of framework electrons (FEC) is equal to 10, whereas the open structure without an X–X bond (**18**) appears for an FEC of 12. The organic C_5 analogues analysed obey the electron counting rules, as seen in Fig. 36. Moreover, we find a group of 6 compounds with type **18** structures and 14 framework electrons with still smaller penetration between the two apical atoms, 76.1 (7)%.

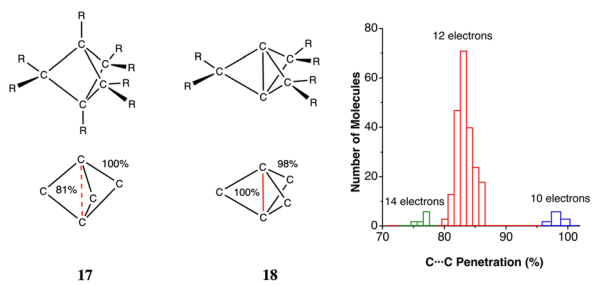

Fig. 36 Distribution of the penetration indices between the two apical atoms in trigonal bipyramidal C_5 cores **17** and **18**, depending on the framework electron count. Data were compiled from 238 crystallographically independent molecules in the CSD (Table S31 in the ESI‡).

Long C–C bonds

The interest in long carbon–carbon bonds has materialized in the last few years in several experimental and computational reports.[17,113,207–210] In the context of this work, it is interesting to calibrate what a "long bond" means in terms of penetration indices. Let us consider the C–C distances in dicarbadodecaboranes, $R_2C_2B_{10}H_{10}$, which have been noted to be quite long.[211] In a CSD search for crystal structures of such compounds, without disorder and an agreement factor $R \leq 10\%$, we have found 2515 crystallographically independent distances, covering the range between 1.429 and 2.156 Å, *i.e.*, penetration indices from 68.5 to 104.5%, with an average of 92(2)%. The penetration indices significantly smaller than the 100% expected for a covalent C–C single bond can be attributed to their electron-deficient nature, while the dispersion of the penetration indices should be attributed to electronic and steric effects of the substituents at the carbon atoms.

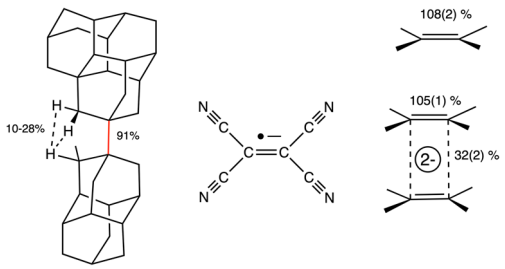

With a different approach, Schreiner and co-workers obtained long C–C bonds between adamantyl, diamantyl and triamantyl groups.[208] The longest distance, 1.704 Å, appears in the diamantyl-triamantyl compound, in which the C–C penetration is 91% (**19**). Its high stability towards dissociation despite the long bond distance was attributed to the existence of several H···H contacts between the diamantyl and triamantyl groups in the range 1.9–2.6 Å, *i.e.*, twelve interactions with penetration indices of 10 to 28%, comparable to those found above for O–H···N hydrogen bonds.

In a quite different chemical system, a long Pb–Pb bond in a diplumbylene compound with $SiMe_3$ groups close to the Pb atoms,[212] a similar Pb···Pb penetration results from the X-ray data, 94%, supplemented by a wealth of H···H contacts with penetrations as high as 22%. In a recent review,[207] Power has also discussed the effect of H···H dispersion interactions between bulky ligands on the element–element bond distances

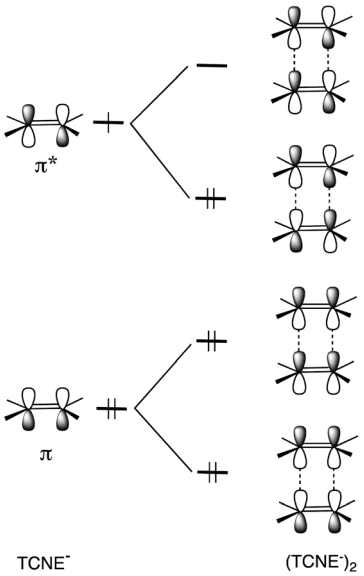

Fig. 37 Orbital interaction diagram between the π systems of two TCNE (TCNE = tetracyanoethylene) radical anions giving rise to the formation of two inter-monomers one-electron bonds (upper part) and significant electron pair repulsion (lower part).

of a variety of organometallic and inorganic compounds. In summary, the long carbon–carbon two-electron bond in **19** has a penetration index of 91%, while in the dicarbadodecaborates, $R_2C_2B_{10}H_{10}$, they can range from 68 to 104%, with an average of 92(2)%.

The radical anion of tetracyanoethylene ($TCNE^{\bullet -}$, **20**) has shown a tendency to form dimers with C···C inter-radical distances of 2.80–3.10 Å. The penetration index for each one-electron C–C bond adopts values between 22 and 37% (the average and standard deviation for 24 structural data sets are shown in **21**). Those values are significantly smaller than those found for other one-electron bonds in a previous section of this work, higher than 50% in all cases (Fig. 28 and 29). The long C–C distances have been attributed to the electrostatic repulsion between the two anionic monomers, but a qualitative MO interaction diagram (Fig. 37) points to a strong Pauli repulsion between the π bonding MOs, which is absent in other one-electron bonds analysed here. The C=C double bonds, in contrast, are little affected by the combined effect of occupying with one electron the π* orbital and the formation of the dimer (**21**) which can be explained by the formation of one-electron bonds between the unpaired electrons occupying the π* orbital of each monomer[213] (Fig. 37).

Metal-cyclopentadienide η^5- and metal–benzene η^6-bonding

The cyclopentadienide anion, $C_5H_5^-$ (abbreviated Cp), and its ability to coordinate in an η^5 mode (*i.e.*, through the five carbon atoms of the ring simultaneously) to a Lewis acid, has been a cornerstone for the explosive ongoing development of organometallic chemistry since the middle of the last century. This anion and a variety of differently substituted derivatives appear as $M(\eta^5\text{-}C_5R_5)$ fragments in well over 60 000 crystal structures in the CSD, including the quite common and versatile (η^5-C_5Me_5) ring, abbreviated as Cp*. For simplicity, we will use in what follows the symbol Cp for any cyclopentadienide derivative, regardless of its substitution pattern. The wide family of molecules with an MCp fragment, thus, appears as an excellent target for a study of the interpenetration of the van der Waals crusts of the M and C atoms. We have therefore calculated penetration indices from the average M–C distance found in the CSD for η^5-coordinated cyclopentadienides with most of the naturally occurring chemical elements, and the results are graphically displayed in Fig. 38, summarizing data for 117 278 independent MCp fragments of 73 elements.

Let us first discuss the behaviour of the transition metal-containing MCp groups, for which the following observations can be made: (a) most transition metals of groups 3–9 show penetrations characteristic of metal-carbon *σ* bonds, *i.e.*, between 90 and 105%; (b) the behaviour of the transition metals of the same group presents practically the same penetration values, regardless of their period; (c) Zn and Cd present smaller penetrations, at around 85%, and so does the only identified AgCp fragment in $[(\eta^5\text{-}C_5H_2(SiMe_3)_3AgP^nBu_3]$,[214] most likely due to the closed shell nature of their d orbitals that cannot,

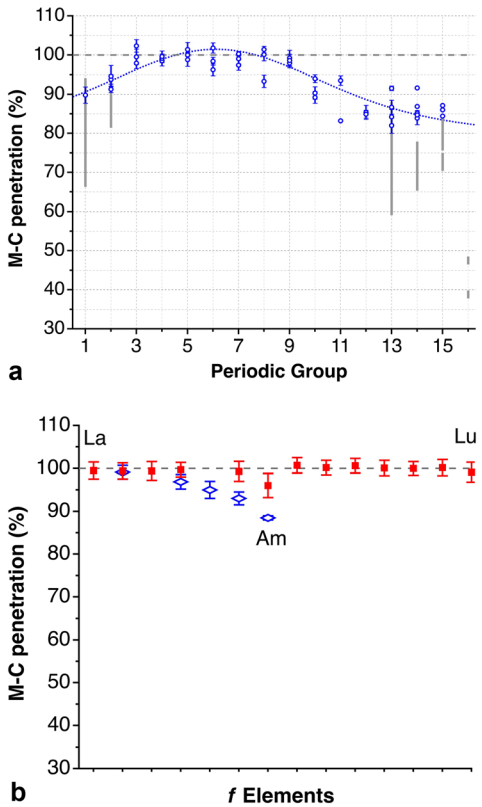

Fig. 38 M–C penetration indices and esds in $M(\eta^5\text{-}C_5R_5)$ groups, where M is any element of groups 1–16 (a) or a rare earth (b). The continuous line is provided only as a guide to the eye; the dashed line marks the 100% value. For main group elements, the grey bars indicate the averages (± one standard deviation) of hypercoordinated MCp fragments, while the circles correspond to those fragments that obey the octet rule (Chart 5). Data are provided in the ESI (Table S32).‡

therefore, act as acceptors as in earlier transition metals. Substantial modification of the electronic properties of the Cp ring through the recent introduction[215] of the perfluorinated Cp* ligand, $C_5(CF_3)_5^-$, gives penetration indices of 95% in two Rh complexes, well within the range presented by a large number of known RhCp fragments.

The main group MCp fragments deserve a more detailed discussion. On average, they have significantly lower penetration indices than the transition metal analogues as well as wider dispersion. A detailed analysis of the structural data reveals that the smaller penetrations are associated with the hypercoordination of the M atom (represented by the grey bars in Fig. 39a), whereas those fragments that obey the octet rule (represented by blue circles) have penetration indices similar to those of transition metals of groups 10–12. Record low penetrations are found in the three group 16 compounds, Cp*$SePh_3$, Cp*$TePh_3$, and $Me_4CpTePh_3$.[216]

Central to the series of electron precise main group MCp fragments is the MeC-(η^5-C_5Me_5)$^{2+}$ cation (Chart 5), commonly referred to as Hogeveen's dication, with a penetration index close to those of transition metals (92%). This carbocation was prepared and characterized by NMR in 1973,[217,218] and its structure has been confirmed by X-ray crystallography quite recently.[219] In the meantime, Hoffmann established its isolobal analogy with an MCp fragment[220] that explains the transition metal-like behaviour of this carbocation. Such an analogy makes the $Mn(CO)_3^+$ and CMe^{3+} fragments orbitally and electronically comparable and, combined with the anionic aromatic Cp* ring, makes the Hogeveen dication isolobal to the [$(OC)_3$-MnCp*] complex (Fig. 39).

Isoelectronic groups extend the isolobal analogy for the five early *s* and *p* groups (Chart 5), including MCp molecular ions of Si, Ge, Sn, Pb, P, As and Sb. The hypercoordinated fragments appear, *e.g.*, in the MCp_2 sandwich compounds and in molecules with more than one extra ligand at the M atom, such as ClSnCp (Chart 5),[221] formally a tin(II) compound, in which the Sn–Cl bond forms an angle with the symmetry axis of Cp of 117° to make room for the lone pair, thus leaving only two sp^3 hybrids available for bonding with Cp, *i.e.*, not isolobal with Hogeveen's dication.

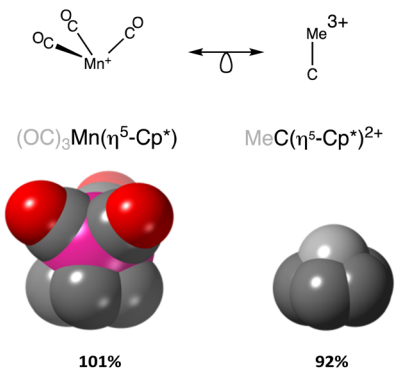

Fig. 39 Space-filling models of [$(OC)_3$MnCp*] and the Hogeveen dication (MeC–Cp*)$^{2+}$, and the corresponding Mn–C and C–C penetration indices. The methyl groups are omitted for clarity.

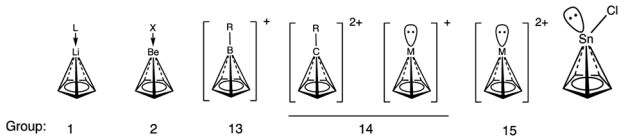

Chart 5 Main group MCp fragments that follow the octet rule, and an example of a similar Sn compound that does not follow the octet rule.

While no structures of cyclopentadienide-noble gas fragments have been found, some argon adducts with isoelectronic neutral rings have been determined in the gas phase: pyrrole,[222] pyrazole,[223] imidazole[224] and furan.[225,226] In all these cases, the average Ar–E penetrations for each compound (E = C, N or O) are around 0%, clearly indicating the van der Waals nature of these complexes. Finally, the rare earths show a quite homogeneous behaviour (Fig. 38b), with penetration indices very close to 100%. The actinides, in contrast, show a continuous decrease from U to Am, with the latter having an average p_{AmC} value of 88.5(5)%.

Given the excellent performance of the penetration indices for the description of bonding in MCp groups throughout the periodic table, it is natural to turn to the bonds and/or contacts of elements with arenes in an η^6-mode. Moreover, given the similar behaviour found for elements of the same group, we go a step further and look now at the E–C penetration indices of all the elements of a group combined. The results of such a study are summarized in Fig. 40. The first thing we see in this figure is that MBz fragments of transition metals of groups 3–11, as well as those of rare earths, behave similarly to those of MCp systems, with penetrations close to 100%. Among group 11 compounds, several structures coded as η^6-coordinated have hapticities of 4 or lower, notably the carbene complexes (NHC)Cu-Bz,[227,228] in which the difference between the shortest and longest Cu–C_{Bz} distance is in the range 0.6–1.0 Å, that are not included in Fig. 40. In other compounds from this group, the metal atom is hypercoordinated and the M–Bz penetration is much smaller. The group 12 metals show a very different behaviour, and they are found connected in an η^6-mode only by non-covalent contacts with a correspondingly low average penetration index of 26(3)%. The lanthanide (Ln) and actinide (An) families are represented in Fig. 40 by the averages of each of the f series, 87(5) and 96(10)%, respectively.

The MBz fragments, where M is a group 1 element, behave similarly to the transition metal-containing MCp fragments, with somewhat smaller penetrations than the transition metals. These are further separated in electron precise and hypercoordinated situations, with average values of p_{MC} of 82(3)% and 72(5%), respectively. The highest penetration within this group in electron precise complexes, 87%, is found for the interaction of the highly charged arene $C_6H_3(BMe_3)_3^{3-}$ with $Li(thf)^+$,[229] undoubtedly favoured by a strong coulombic attraction. A slightly higher penetration, however, appears for a hypercoordinated Cs compound.[230] Unlike alkaline ions, the proton is not found as an η^6 adduct with benzene, which corresponds to a high energy second order transition state,[231] but it forms a σ bond with one carbon atom. A covalently bonded hydrogen atom R–H, however, can establish η^6

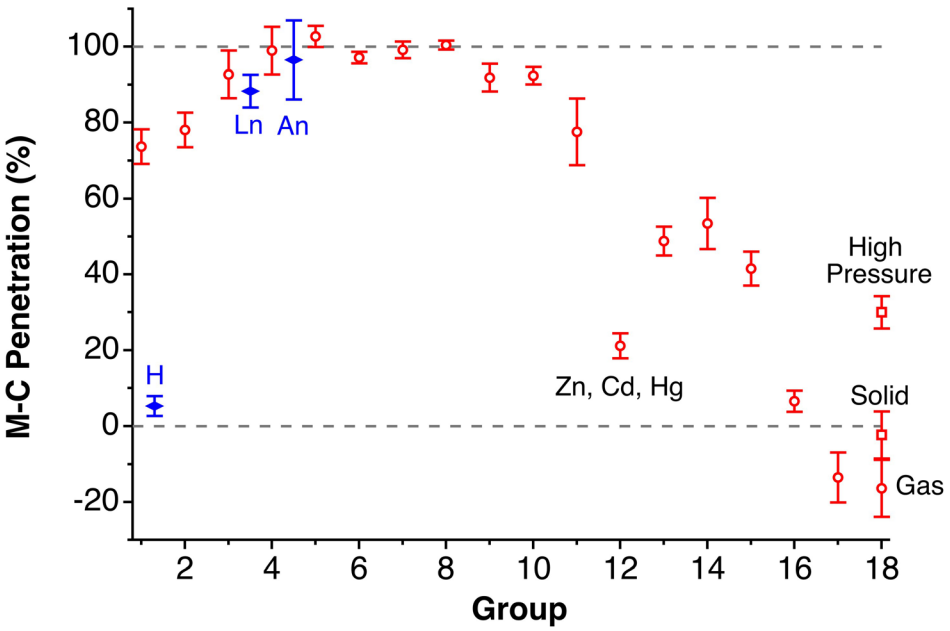

Fig. 40 E–C penetration indices and esds for all elements of the same periodic group in η^6-bonded or weakly interacting E–benzene fragments (circles). The diamonds represent the average values and esds of all the lanthanides (Ln) and actinides (An) η^6-coordinated by benzene, placed close to group 3 elements for comparison and of the intermolecular H···benzene contacts. The data for groups 1, 2, 16, 17, and 18 have been retrieved as intermolecular contacts. Data are provided in the ESI (Table S32).‡

noncovalent interactions through small positive RH···C penetrations, with an average penetration index of 5(3)%, indicative of essentially dispersion-governed interactions.

Alkaline-earth MBz fragments also reach relatively high penetrations, with an average index of 80 (6)%, most likely due to the supplementary coulombic attraction of the alkaline-earth cations. The highest penetration (96%) is found in a half-sandwich Ca complex,[232] and penetrations in excess of 80% are found as well for Mg,[233] Sr,[234] and Ba,[235] and similar values are obtained from the calculated distances[236] for Ca, Sr and Ba (84–92%). The Mg and Ca ions coordinated by NacNac (abbreviation for the ligands with the pentane-1,3-diiminato skeleton, **22**) are found bonded to aryl rings that achieve in general quite high penetrations, in the range 78–95%.[237–240] The recently reported[241] Be_2Cp_2 fits nicely into this picture.

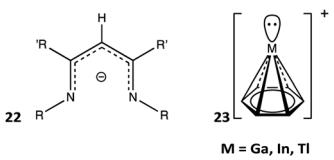

The elements of groups 13–15 present penetration indices significantly lower than those of the earlier groups, except for the Zn group. They are coded in the CSD as bonded, and slight differences appear between the electron precise and hypercoordinated systems, except for the group 15 ones, for which no electron precise structures have been found. It is interesting to stress the presence of pristine group 13 MBz^+ molecular cations with hemispherical coordination, whose electronic structure is schematically depicted in **23**, where M is Ga,[242,243] In[244] or Tl,[245] all with similar penetration indices between 50 and 62%.

The elements of the rightmost two groups, the halides and the noble gases, have negative average penetration indices, −13(7) and −17(8)% for groups 17 and 18, respectively. Such a small approach points to purely dispersion-dominated interactions with the arene rings. The penetration indices with the noble gases, moreover, are seen to increase asymptotically with the covalent radius (Fig. 41), a result that is consistent with the dependence of the London attraction on the polarizability which, in turn, increases with the atomic number of the interacting atoms,[246] according to the Fajans rules.

Ionic solids

In solid state chemistry it is common to analyse structural data using Shannon and Prewitt's ionic radii.[247,248] It might thus, in principle, seem odd to use penetration indices for ionic solids,

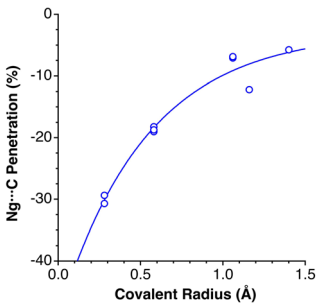

Fig. 41 Dependence of the noble gas-benzene penetration index on the covalent radius of the former. The line shown is a fitting to an exponential function with a limiting value of −3%. Data are provided in the ESI (Table S33).‡

since they are defined based on the covalent and van der Waals radii. Certainly, the values of the ionic and covalent radii for a given element are quite different; in addition, while a covalent radius is representative of the distribution of bond distances of an element in different coordination numbers and oxidation states, the ionic radius is in most cases specific for only one oxidation state and a fixed coordination number. Yet, for a pair of elements with different electronegativities, their covalent radii sum is rather similar to the corresponding ionic radii sum in their common oxidation states. For instance, for the Ba–O couple, the covalent and ionic radii sums are 2.81 and 2.75 Å, respectively, or 2.60 and 2.71 Å for K and F. In some cases, they may even differ by 0.02 Å or less, well below the uncertainty of those atomic parameters, as for the Sr–Cl, Ba–Cl, As–O, Cs–F, Ca–F, Sr–F, Cs–Br, Cs–S and other atom pairs (more information provided in ESI, Table S40 and Fig. S8a‡). Further support for the use of covalent radii comes from the good agreement between the M–O distances in aqueous solution for a set of 33 monoatomic cations compiled by Marcus.[249] For most of the main group and transition metal cations, the average deviation of the M–O distances from the covalent radii sum is less than 0.11 Å (see Fig. S8b in the ESI‡), and only for Ag^{+} and Hg^{2+} is it between 0.3 and 0.4 Å. The lanthanides, Y, and Th, show an excellent correlation between the two parameters, in such a way that the Ln–O distance is equal to the sum of covalent radii minus 0.19 Å.

The NaCl structure

In one of the commonest and most symmetric solid-state structures of binary AX compounds, the NaCl structure, the main stabilizing factor is assumed to be the electrostatic attraction between neighbouring A^{n+} and X^{n-} ions, counterbalanced in part by the anion–anion and cation–cation coulombic repulsions. These strictly ionic interactions are usually modelled with the well-known Madelung potential.[250] In the face-centred cubic NaCl structure, the A···A and X···X distances are identical and are related to the A–X distance (**24**). But what if we consider this structure from the point of view of the penetration of the van der Waals crusts? Even with the same distance, each pair may have quite different penetrations, depending on the relative sizes of A and X and the width of their van der Waals crusts.

X-X = A-A = √2 (A-X) **24**

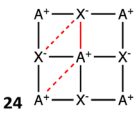

Our present exploration focuses on a sample set of 103 structures of binary AX solids (see ESI, Table S34‡). In Fig. 42a we show the distribution of the A–X, A···A, and X···X penetration indices in that data set. Unsurprisingly, the A–X penetrations are centred around the 100% mark, showing that it is reasonable to use the same set of atomic radii for covalent and ionic bonds. It is also natural that the X···X penetrations are small or negative. In contrast, the A···A penetrations are rather large, their distribution sensibly overlapping with that of the A–X bonds, a fact that results from the generally larger size of the electropositive elements, compared to elements of groups 15–17 that form anions.[6] In some cases, the "non-bonded" cation–cation penetration is even higher than the cation–anion one, as in CsD, CsF, FeD, CsF, NaD, BaO, LaN, and UC.

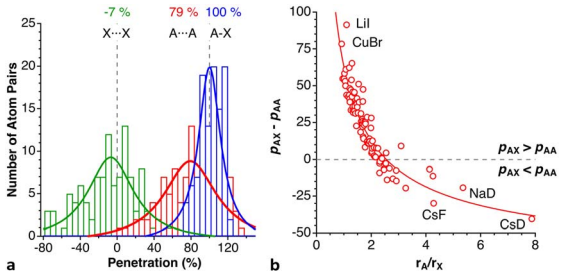

Fig. 42 (a) Distribution of the cation–anion (A–X), cation–cation (A···A), and anion–anion (X···X) penetrations in a sample of 102 AX compounds with the NaCl structure. (b) Relationship between the difference in A–X and A···A penetrations and the ratio of covalent radii. Data are provided in the ESI (Table S34).‡

Given the relationship between the A–X and A···A distances imposed by the cubic symmetry (**24**), the differences between the A–X and A···A penetrations should depend on the relative size of atoms A and X, as can indeed be seen in Fig. 42b. There we see that the penetration between the two "non-bonded" cations (p_{AA}) becomes higher than that between the bonded cation–anion pair (p_{AX}) for a covalent radii ratio r_A/r_X higher than 2.5, which comprises compounds such as AmN, CmN, ZrC, HfC, VO, VN, MgO, and the high-temperature structure of CsCl. There are many binary compounds with smaller size ratios and $p_{AX} > p_{AA}$, in which the A–X penetration is much higher than the A···A one, as expected for bonding and non-bonding situations, respectively, including the case in which the cation and anion have the same size ($r_A/r_X \approx 1.0$), as in the cases of PbTe, AgI, HgTe, InSb, LiBr, NaI, LiI and CuBr, or in the elemental fcc structures of Rh, Al, Cu, or La. At the other extreme of the curve, we find compounds in which the cation is much larger than the anion, of which there are only a few examples in our sample, notably deuterides/hydrides and CsF. The very high interpenetration between the Cs atoms in the latter compound (130%), compared to a standard 100% penetration for the Cs–F bonds, challenges the simple ionic model in this case, despite the large electronegativity difference between Cs and F, since it indicates a higher penetration of the van der Waals crusts of two ions of the same charge than for those of atoms with opposite charges.

The structure of NaCl itself, studied at variable temperatures or pressures (see ESI, Fig. S9‡), is highly illustrative of the effect of those external factors. The Na–Cl distance increases little under applied pressure, and the penetration correspondingly increases from 91% at ambient pressure to 104% at 31.1 GPa.[251] In contrast, the non-bonded atom pairs become much closer, their penetration indices increasing from 60 to 118% (Na···Na) and from −22 to 39% (Cl···Cl) in the same pressure range. It is well known that the main effect of increasing the temperature on most solids is an expansion of the crystal lattice, *i.e.*, a decrease in the interatomic penetrations, except for the

special family of materials with a negative thermal expansion coefficient. However, the effect is rather small, compared to the effect of applied pressure, and in the case of NaCl, the penetrations decrease by only 5–6% for the Na–Cl bonds as well as for the Na···Na and Cl···Cl contacts on going from room temperature to 873 K. Interestingly, such a small interpenetration decrease seems to be enough to allow for a higher mobility of the sodium cations and to enhance the ionic conductivity by several orders of magnitude.[252]

The perovskite structure

Similarly to what is shown in the previous sub-section for binary compounds with the NaCl structure, we have carried out a penetration study on ABO_3 compounds with a perovskite structure. In that structure, the B cations occupy octahedral sites and form strong coordination bonds with the oxo ions, whereas the more electropositive A cations are commonly considered to be held by electrostatic interactions in cubic O_8 sites.

The first case studied here is a prototypical perovskite, $BaTiO_3$. The Ba–O, Ti–O and Ba–Ti interpenetrations decrease by at most 4% from room temperature to 1645 K. More interestingly, the Ti–O and Ba–Ti penetrations are practically identical, at around 115%, clearly higher than the still high 96–100% values of the Ba–O pairs. The other two perovskites explored, $CaGeO_3$ and $CaSnO_3$, present distinct penetration ranges for the three atom pairs considered, but all of them are within the 90 to 110% interval (see Fig. S10 in the ESI‡). The high penetration indices are consistent with the observation of Vegas and coworkers,[253] that in $MSnO_3$ perovskites (M = Ca, Sr, Ba) the MSn substructure has the same topology than the high-pressure structure of MSn alloys and, in the case of M = Ba, even the same unit cell parameters. In a wider context, much work has been devoted to the recognition of metal structures in metal compounds.[254]

Covalent bonds: single and multiple

Common main group element–element bonds

In this section, we wish to explore how the applicability of penetration indices can be extended to covalent bonds, from single to triple bonds between main group elements. To this end, we have analysed the penetration indices for some of the commonest bonds involving second-row elements. First, we look at the structures of simple prototypical molecules in the gas phase (Table 2), which seem to present a good correlation between the bond order and penetration index (Fig. 43a).

The good bond order-penetration index correlation found for a limited set of prototypical compounds in the gas phase might not be representative of what may happen for a much wider set of molecules. For this reason, we analysed the same element–element bonds in the CSD crystal structure database. The results, shown in Fig. 43b, indicate that, except for the relatively low penetration found in peroxides, all single bonds appear close to the 100% mark, the double bonds at around 108%, and the triple bonds at about 117%, consistent with the ranges found for our reduced set of gas phase molecules. For the specific case of the B–B bonds, we also show in the ESI‡ (Fig. S11) the dependence of the penetration on bond order similar to that shown in Fig. 43a for the CSD structures, including the non-bonding distance of compound **9** as an example of bond order zero, and we find that the B–B penetration in diborane can be interpolated to a bond order of 0.86.

In a recent study,[256] Bickelhaupt and co-workers showed the relevance of the atomic size of the interacting atoms in determining the bond dissociation energy for a series of small R–R′ molecules (R, R′ = CH_3, NH_2, OH, F, SiH_3, PH_2, SH and Cl). That work reported the energy difference and the overlap between the SOMOs of the two interacting groups for Me–R′ (R′ = Me, Cl, F) at their energy minima. We find both parameters to be nicely correlated with the corresponding penetration indices: the penetration decreases as the gap increases, and the overlap increases with the penetration. Despite the small amount of data available, this seems like another promising direction for the application of penetration indices in computational and theoretical chemistry which deserves further exploration in the future.

Table 2 Penetration indices (in %) for main group element–element bonds with different bond orders (b.o.) in some simple prototypical compounds. Data for the gas phase are obtained from the Mogadoc database

B. o.	C–C	N–N	O–O	C–O	C–N	Range
1.0	99.4[a]	98.6[b]	91.6[c]	100.5[d]	100.4[e]	92–101
1.5	106.3[f]	104.6[g]	102.8[h]	107.7[i]	106.7[j]	103–107
2.0	109.2[k]	108.9[l]	106.5[m]	110.2[n]	110.1[o]	106–110
2.5	113.1[p]p	115.2[y]	112.1[q]	116.5[r]	113.1[s]	112–117
3.0	115.6[t]	116.9[u]	116.3[v]	115.8[w]	116.2[x]	116–117

[a] C_2H_6. [b] Hydrazine. [c] H_2O_2. [d] Me_2O. [e] $MeNH_2$. [f] Benzene. [g] Pyridazine. [h] O_3. [i] M(acetylacetonate)$_n$ (M = Mn, Cu, Zn; n = 2, 3). [j] Pyridine. [k] Ethylene. [l] N_2Me_2. [m] O_2. [n] H_2CO. [o] H_2CNH. [p] $C_2H_2^+$. [q] O_2^+. [r] CO^+. [s] HCN^+. [t] HCCH. [u] N_2. [v] O_2^{2+}.[255] [w] CO. [x] HCN. [y] MeN_3.

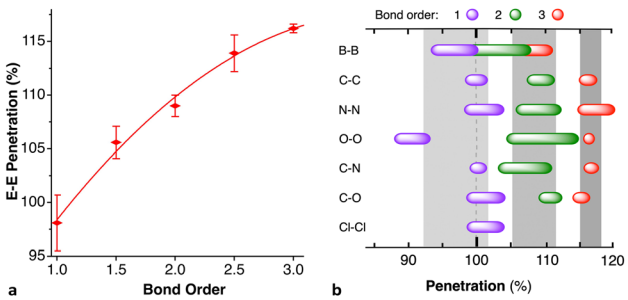

Fig. 43 (a) Average penetration indices and esds found for element–element bonds with different bond orders in some prototypical compounds (Table 2) in the gas phase. (b) Progression of the penetration indices (average ± two standard deviations) of several single, double and triple element–element bonds, as deduced from the analysis of crystal structural data from the CSD (see ESI, Tables S35–S37‡). The shaded areas correspond to the ranges of values found for the gas phase bonds (Table 2).

Metal–metal multiple bonding

Having seen how the penetration indices allow us to compare bonds of different pairs of main group elements, an obvious test is to carry out a similar analysis for transition metals that can span five bond orders, such as Cr or Mo in their different oxidation states. The distribution of Cr–Cr bond distances as a function of the bond order, commented on by us in previous work,[257] can be easily translated to the penetration index language. The results are summarized in Fig. 44, where we can see that there is a practically linear correlation between the centre of the Cr–Cr penetration index distribution and the bond order ($r^2 = 0.989$), spanning the range from 100 to 145%, even if there is some overlap of the penetration distributions between the sets of structures whose bond orders differ by only one unit. A similar trend can be found for the Mo–Mo bonds, although with higher penetration than the Cr–Cr ones for the same bond order.

Although actinide–actinide bonds are less common, interest in U–U bonding has led several researchers to carry out computational studies on some simple molecules such as U_2, $(\mu\text{-H})_2U_2$ and $H_2U_2H_2$, which had been previously detected in the gas phase or by matrix isolation. In a diatomic molecule, even if six bonding electron pairs could in principle be formed, high-level calculations have led to assigning a U–U bond order of five.[258] Notwithstanding the bond order, the penetration index corresponding to the optimized distance has an amazingly large value of 199%. Earlier DFT calculations[259] for $(\mu\text{-H})_2U_2$ and $H_2U_2H_2$ also give very high penetration indices (216 and 210%, respectively), even if in the latter case the maximum possible bond order would be four. Crystallographically characterized U–U bonds all show much smaller penetrations (125–146%), comparable to those found for Cr–Cr and Mo–Mo double and triple bonds (Fig. 44). For comparison, the Th–Th bonds in 75 independent structural data sets from 17 structures found in the CSD have penetration indices of 105–129%, consistent with the lower ability of this element to form multiple bonds due to its smaller number of valence electrons. The absence of bridging ligands in U_2 and the unusually large penetration make it an interesting case for further investigation.

Multiple bonding in actinyl groups

One of the most common motifs in the chemistry of actinides is the actinyl group, formed by two bonds between an actinide and bare oxygen atoms in a *trans*-position, *i.e.*, forming a practically linear O≡An≡O group, to which triple bond character is attributed.[260] Analogous groups can be found for transition metals, as in molybdenyl or osmyl ions, that can be compared to the CO_2 molecule. By analysing the structural data for actinyl compounds, we wish to test if the penetration index can be used as a general bonding indicator for all the actinides and to compare the An–O bonds with similar bonds involving other elements of the periodic table.

The results of such an analysis are presented in Fig. 45. Notice that each of the four types of oxyl bonds analysed there covers a relatively narrow range of penetration indices (less than 25%), with the actinyl groups showing significantly higher penetration values than the other bonds to oxygen studied. Also notice that the estimated standard deviation of the distribution peak (Table 3) for one single molecule, CO_2, in different crystal environments, is significantly larger than those of the other M=O bond families considered, even if they contain a wide variety of M and An atoms bonded to oxygen or of substituents *R* in the case of ketones. This shows what a powerful tool the penetration index is for summarizing structural information of large groups of analogous bonds implying atoms of different sizes. Despite the experimental uncertainty in the penetration values for CO_2, they are within the upper part of the distribution function for C=O bonds in the large family of acyclic ketones.

We then zoom in on the peak of the actinides and treat the data for each element separately, showing fittings of the

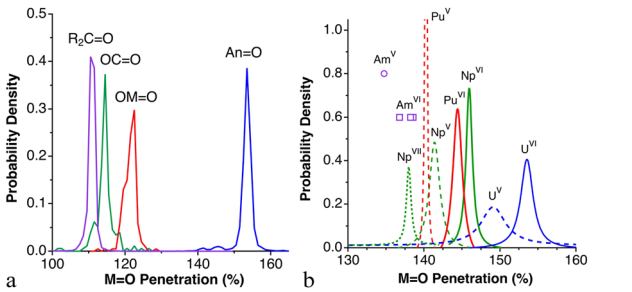

Fig. 45 (a) Distribution of penetration indices in ethers, CO_2, transition metal MO_2 and actinyl AnO_2 groups. (b) Breakdown of the actinyl peak by element and oxidation state. Data are provided in the ESI (Tables S38 and S39).‡

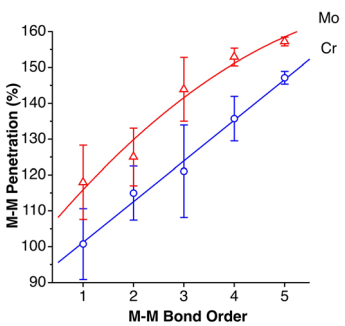

Fig. 44 Average penetration indices and esd for M–M bonds of a given bond order (M = Cr, Mo). Data were adapted from ref. 257.

Table 3 Average values of the penetration indices (p_{av}, esd in parentheses) for bonds to oxygen in actinyls, metals (M) of the second and third transition series, CO_2 molecules trapped in organic or organometallic crystal structures, and acyclic ketones. The position of the maximum of a Lorentzian distribution function (p_{max}) resulting from least squares fitting to the corresponding histogram is also given for comparison, and *N* is the number of independent structural data sets found for each family. Raw data are provided in ESI, Table S38

	p_{av}	p_{max}	*N*
O≡An≡O	153 (1)	153.6	6509
O=M=O	120 (1)	121.8	208
O=C=O	114 (6)	114.4	177
R_2C=O	111 (1)	111.0	22 192

Table 4 Ranges of M–O bond distances and penetration indices of actinyl groups, average penetration indices (p_{av}) and penetration indices at the maximum probability density (p_{max}), obtained from a fitting of the probability density histograms to a Lorentzian function. N is the number of crystallographically independent data sets

	N	M–O (Å)	p (%)	p_{av} (%)	p_{max} (%)
All U	6212	1.52–2.47	109–169	153.5 (10)	153.6
U^{VI}	2078	1.52–2.47	109–169	153.5 (10)	153.5
U^{V}	60	1.76–1.90	145–154	149.4 (19)	149.1
Np^{VII}	4	1.89–2.06	128–138	135.2 (35)	138.0
Np^{VI}	113	1.68–1.78	144–150	146.0 (6)	146.0
Np^{V}	96	1.73–1.90	137–147	141.4 (8)	141.4
Pu^{VI}	74	1.71–1.78	142–146	144.4 (5)	144.4
Pu^{V}	6	1.81–1.82	140–141	140.2 (2)	140.3
Am^{VI}	3	1.74–1.77	136–139	137.9 (9)	—
Am^{V}	1	1.81	135	—	—

corresponding histograms to Lorentzian functions for clarity (Fig. 45b). We find that each of the elements appears in a distinct range of penetration indices, and they are even well separated by oxidation states (Table 4).

Conclusions and perspective

Based on the standard empirical sets of covalent and van der Waals atomic radii, the periodic behaviour of the width of the atomic van der Waals crusts has been analysed and found to be between 0.60 and 1.20 Å for all naturally occurring elements, which represent over 60% of the volume of the atomic van der Waals spheres, reaching proportions higher than 90% for H, He, and B–Ne. The crusts of alkaline elements, on the other side, are found to occupy the smallest portion of the van der Waals sphere for a given period.

We have shown how the Lennard-Jones potential energy curves as a function of the interatomic distance can be successfully replaced by energy as a function of the penetration index, which should greatly facilitate comparisons for pairs of elements with different atomic sizes and, consequently, quite different interatomic equilibrium distances. In the case of noble gas-noble gas or noble gas-molecule van der Waals adducts, in homopolar dihydrogen bonding between alkanes, or in the interlayer contacts of 2D solids, penetration indices are found around the 0% value. The penetrations, though, can be modulated using applied pressure or using the electronegativity difference between the interacting atoms.

As forces other than London dispersion appear in non-covalent bonding, higher penetrations are achieved, as in the σ-hole and metallophilic interactions, ion-dipole interactions or the wide variety of hydrogen bonding interactions. Higher penetration indices are found for one- and three-electron bonds, smaller than those for single bonds but, surprisingly, not much smaller, reaching values of up to 80%. A similar range of penetrations can be found for secondary metal–ligand interactions, 3 center-2 electron bonds or electron-deficient bonding.

In general, the penetration index and bond order evolve in parallel. In the case of Xe–O bonds and nonbonded contacts found in enclathrated XeO_3 molecules, such a relationship is reflected in a good correlation between the calculated Wiberg index[200] and the penetration index. It is still more remarkable that electron-deficient bonds, *e.g.*, in boranes have penetration indices above 90%, very close to those of single bonds. Exceptions to these general trends are the C–C single bonds between adamantyl, diamantyl and triamantyl groups reported by Schreiner *et al.*,[208] whose lengths correspond to penetrations as small as 91%, and the intermonomer C–C distances in the dimer of the $TCNE^{\bullet-}$ radical anion,[213] formally one-electron bonds, with penetrations of around 30%.

In ionic solids or highly polar molecules, penetration indices between atoms with opposite charges are similar to those found for covalent single bonds and to covalent coordinating bonds. An unexpected finding for ionic solids is that the interpenetrations of crusts of two neighbouring, "non-bonded" cations cover a wide range of penetration indices, between 60 and 120%, becoming higher than those between the bonded cation–anion pair for a covalent radii ratio r_A/r_X higher than 2.5.

All in all, the ranges of penetration indices found for a host of systems analysed in this work (Fig. 46) describe a continuous path between non-bonded and strongly bonded atom pairs. Such a pathway between nonbonding and bonding is nicely represented by the ranges of stability of three types of O–H interactions calibrated by Lobato *et al.*,[17] expressed in terms of penetration indices, which go from 4 to 23% for van der Waals contacts, to 42–62% for O···H hydrogen bonds, and from 81 to 124% for O–H covalent bonds, although the distribution of the hydrogen bonds obtained from crystallographic data (Fig. 22a) reveals a still wider range (25–60%).

The highest penetration indices were found in quintuple Cr–Cr (144–150%) and Mo–Mo (156–158%) bonds. Interestingly, the corresponding values for the sextuple bonds calculated by Roos *et al.*[261] for diatomic Cr_2 (153%) and Mo_2 (162%) molecules are not significantly higher than those of the quintuple bonds,

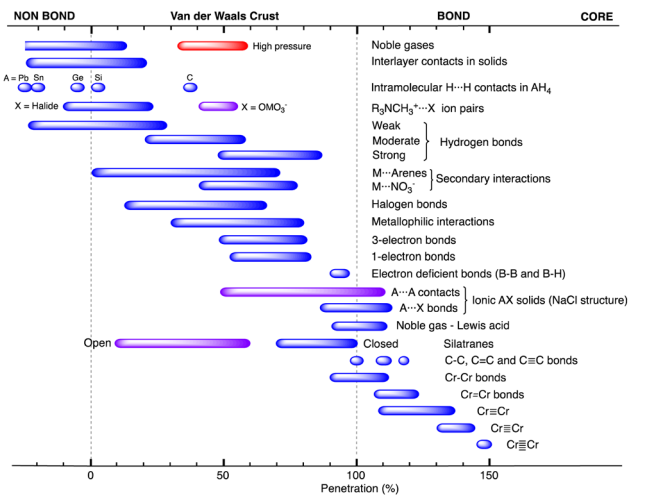

Fig. 46 Ranges of penetration indices presented by the different bond types discussed in this paper, showing continuous distribution from the very low penetration of pure van der Waals interactions to the strongly covalent metal–metal quintuple bonds.

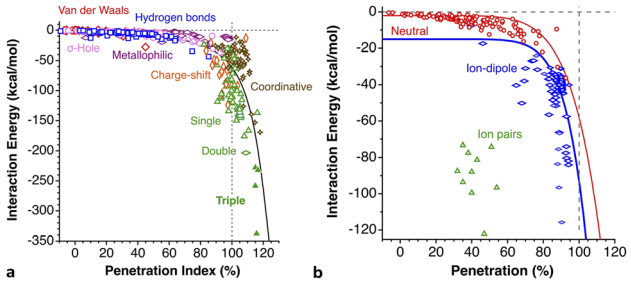

Fig. 47 (a) Distribution of interaction energies between neutral species for different types of atom–atom interactions according to their penetration index. (b) Comparison of the interaction energies in σ-hole interactions involving two neutral (circles), one ionic (rhombuses) and two ionic (triangles) species.

considering that the attribution of a sextuple bond implies the existence of two σ components. The record high penetration (199%), however, results from calculations on the U_2 molecule,[258] to which a formal bond order of five has been attributed.

An important question addressed in this paper is whether there is some general trend relating the degree of interpenetration to the interaction energy for non-covalent interactions. As a first attempt at answering such a question, we collect in Fig. 47 data for a wide variety of systems for which interaction energies have been reported by several authors, from weak van der Waals interactions to covalent triple bonds, with the only restriction that at least one of the two interacting moieties must be neutral. There, we plot the interaction energies published by several authors as a function of the penetration index, calculated by us from the optimized distance reported. Briefly, these are the data sources:

(a) The van der Waals family includes homo- and heteroatomic dimers of noble gases discussed in this work, as well as those reported by Zhou *et al.*,[19] and the homopolar C–H···H–C interactions between simple alkanes and polyhedranes reported earlier by us,[199] those between the hydrogen atoms in dimers of tri(3.5-*tert*-butylphenyl)-methane or unsubstituted and triphenylmethane reported by Schreiner and coworkers[113] and between two E_2H_6 molecules (E = B, Ga).[262]

(b) The metallophilic interactions include dimers of d^8 square planar complexes[81] and of linear d^{10} complexes of Hg,[80] or group 11 elements (Cu, Ag, and Au),[263,264] disregarding some [L–Cu–X] complexes in which the dimer is held together mostly *via* intermolecular Cu···X interactions.

(c) σ-hole interactions include atom pairs grouped under the umbrellas of halogen bonding,[166,169,172] chalcogen bonding, tetrel bonding,[165] Br···CO interactions,[265] and M···XC_6F_5 interactions.[266]

(d) A sample of 58 different hydrogen bonds analysed by Srivastava[267] and the classical hydrogen bonds in adducts of water, ammonia and HF reported by Freindorf *et al.*[268]

(e) A sample of covalent bonds, that comprises C–C bonds and H_2[269,270] and the triple bonds in N_2 and CO.[270]

(f) Characteristic charge-shift bonds.[271,272]

(g) Metal–ligand bonds in 18-electron complexes of Fe, Ru, Os, Cr, Mo and W with ethylene and acetylene[273] or with N-heterocyclic carbenes[274] and Ru–L bonds.

The different types of non-covalent interactions cover different ranges of penetration values, consistent with Fig. 46. Moreover, it can be seen that the dependence of the interaction energies reported by different authors on the penetration index follows a general trend, according to which the interaction energy decreases gradually for penetration indices of up to 60% and drops sharply for higher degrees of interpenetration, offering a non-linear continuum of bonding intensities from the very weak van der Waals interactions to the triple bonds of molecules such as N_2 and CO, although a more extensive study should be performed to have a better representation of the penetration indices higher than 100%. A sample of coordinative bonds in transition metal complexes computationally analysed by several authors appears to follow a trend similar to that of the covalent bonds (Fig. 47a). It is also noteworthy that the highly polar covalent bond in the NaCl molecule behaves similarly to the non-polar bonds.

As could be expected, the interactions involving charged species enhance the attractive energy between the interacting species. This can be seen by comparing the penetration dependence of the interaction energy for neutral σ-hole systems with similar interactions involving one species with a +1 or −1 charge: chalcogen[275] or tetrel bonds,[165] involving a halide ion, and halonium ions,[276] *i.e.*, ion-dipole or ion-induced dipole interactions (Fig. 47b). If the two interacting species are ions of opposite charge, as in the tetramethylammonium-halide ion pairs recently investigated by us,[10] further stability is achieved for the same penetration index.

The present study has allowed us to detect that it is common to find a similar penetration dependence of the electrostatic and Pauli components of the interaction energy and there is consequently a correlation between these two terms in the case of dimers of noble gases (Fig. 4). As a result, there is a net repulsive effect of these two terms in uncharged systems, which can be compensated for by the weaker London dispersion forces only at quite low penetrations (long distances). In Fig. 48a we see how the EDA analysis of the interaction between two noble gases shows us that increasing the electrostatic attraction by decreasing the interatomic distance is destabilising because the

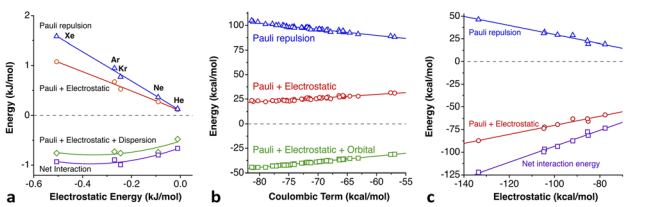

Fig. 48 (a) Effect of the addition (from top to bottom) of the electrostatic and dispersion terms to the Pauli repulsion for optimized Ng_2 dimers, compared to the net interaction energy. (b) Effect of the addition (from top to bottom) of the electrostatic and orbital terms to the Pauli repulsion for optimized adducts of iodonium cations with N-donor Lewis bases. The net interaction energy is practically indistinguishable from the sum of the electrostatic, Pauli and orbital terms (squares). (c) Effect of the addition of the electrostatic and orbital terms to the Pauli repulsion and the net interaction energy for the TMA·X ion pairs in the κ-C and 3κ-H conformations.

Pauli repulsion increases even more. The addition of the London dispersion component, however, is enough to compensate for the net Pauli plus coulombic repulsion, making the interaction slightly attractive and very close to the total interaction energy. The same behaviour has been found by us in the set of covalent bonds and coordinative bonds and non-bonding interactions analysed by Kumar *et al.*[277] (see Fig. S12a–c in the ESI‡), with only donor–acceptor complexes involving N or O as donor atoms and BR_3 molecules as Lewis acids.

For comparison, we present in Fig. 48b a similar EDA analysis for the adducts of iodonium cations with N-donor Lewis bases (D), $D–I^+\cdots D$.[276] It shows that, even if the electrostatic contribution is much stronger than that for the case of Ng_2 dimers, it is the orbital interaction terms that make the adducts stable, resulting in much higher interaction energies (notice the different energy units used in Fig. 48a and b), and much higher penetrations (90–91%) than those in the case of noble gas dimers (between −12 and +2%). In a different direction, in the hydrogen-bonded systems studied by Grabowski,[278] which show a similar correlation between the electrostatic and Pauli energy terms, the electrostatic attraction slightly overcomes the repulsion (Fig. S13a and b in the ESI‡).

Needless to say, when the two interacting species have charges of opposite signs as in tetramethylammonium-halide (TMA·X) ion pairs,[10] the coulombic component is the predominant one, overwhelming the Pauli repulsion (Fig. 48c). A non-negligible orbital contribution is also apparent. In those ion pairs, two interaction topologies are considered, one in which the halide interacts with one methyl group, with a predominant X···C penetration but non-negligible X···H penetrations (termed κ-C), and another in which the interaction is with three hydrogen atoms of three different methyl groups of the TMA cation (3κ-H interaction). Interestingly, regardless of the interaction topology, the different contributions to the interaction energy are well correlated, and the resulting interaction energies are significantly higher than those of the ion-dipole interactions of the halonium systems (Fig. 48b), despite the lower penetration values of the closest contacts (32–54%). The wide variety of ion pairs formed by carbadodecaborate anions and a host of cations submitted by Madureira *et al.*[279] to an energy decomposition analysis also present a correlation between the electrostatic and Pauli repulsion terms (Fig. S13c in the ESI‡), with an important net contribution to the interaction energy.

Additional directions for further applications of the penetration index can be foreseen, and preliminary studies on some of them are giving promising results. We can mention the study of reaction pathways and transition states, wherein the penetration indices between bonds being cleaved or formed can provide useful information on the associative or dissociative nature of the transition state, the effect of oxidation states or coordination number on bond strengths, a possible calibration of the degree of frustration of Lewis pairs, the correlations

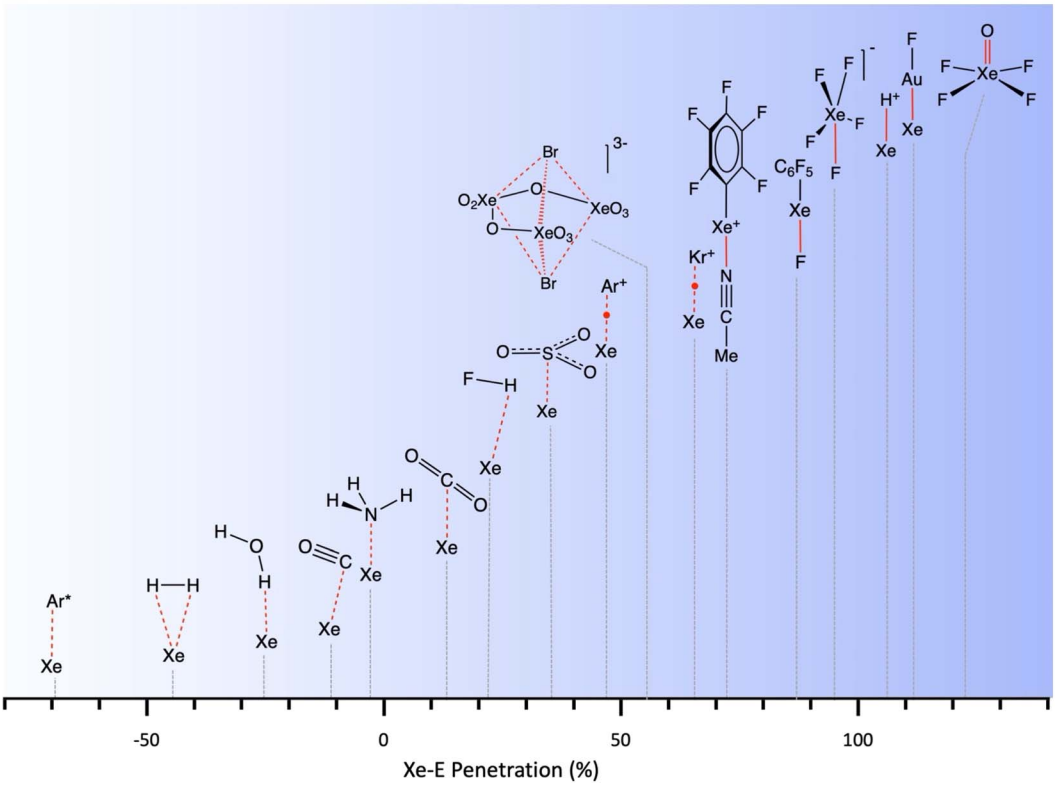

Fig. 49 Panoramic view of the many possibilities of bonding of a chemical species to a Xe atom, displayed in increasing order of the Xe-element penetration index, from an excited state of the Xe···Ar diatom (−69%) and an interaction with the σ H–H bond of the dihydrogen molecule (−44%) through one-electron bonded Ar–Xe^+ and Kr–Xe^+ cations (48 and 66%) to the hypervalent XeF_5 (98%) and the two-electron bonds in Xe–H^+, F–Cu–Xe and $XeOF_5$ (106, 115 and 121%).

between bond distances and vibrational force constants (or infrared stretching frequencies), the structure of excited states and exciplexes, or the analysis of the nuclear spin coupling and the hyperfine coupling between unpaired electrons and nuclear spins of neighbouring atoms evaluating the core-valence interpenetrations, of importance in EPR and NMR spectroscopies.

In summary, we think that the present work provides solid support for the application of van der Waals penetration indices to the analysis of covalent and non-covalent bonding as well, which allows for the comparison of interatomic distances regardless of the size of the interacting atoms. Thus, we have shown the existence of good correlations of penetration indices with bonding and energetic parameters such as bond angles, interaction energies, contributions to the interaction energy obtained from EDA analysis, formal bond orders or calculated Wiberg bond indices, or the electronegativity difference between the interacting atoms. We wish to illustrate our take-home message with a last figure (Fig. 49) that presents a map of the wealth of interactions involving a Xe atom, covering the range of penetration indices between −69 and +121%).

Methodology

The methodology for the structural searches and the computational studies reported are given in the ESI.‡

Data availability

The Methodology section, complementary figures and tables, and a spreadsheet with the raw data for all figures are available in the ESI.‡

Author contributions

Both authors contributed to the conceptualization, funding acquisition, planning of the research and methodology, and revision of the original draft. JE carried out the DFT calculations and EDA analysis and visualization. SA carried out the data curation and the writing of the original draft.

Conflicts of interest

There are no conflicts to declare.

Acknowledgements

The authors are grateful to professors Stuart Macgregor, Wojciech Grochala, Matthias Bickelhaupt, Ángel Vegas, Pere Alemany, Sason Shaik and Roald Hoffmann for inspiring discussions. This work was supported by the Spanish Ministry of Economy and Competitiveness (PGC2018-093863-B-C21 and PID2019-109119GA-I00), the Spanish Structures of Excellence María de Maeztu program (grant MDM-2017-0767) and the Generalitat de Catalunya – AGAUR (grant 2017-SGR-1289). The allocation of computer time at CSUC is also acknowledged. J. E. is indebted to the Spanish MICCIN for a Ramón y Cajal research contract (RYC-2017-22853) and to the Gobierno de Aragón-ESF program (Research Group E07_23R) for financial support.

References

1 R. F. W. Bader, *Atoms in Molecules, A Quantum Theory*, Clarendon Press, Oxford, 1990.
2 S. Alvarez, *De mujeres, hombres y moléculas*, Edicions Universitat de Barcelona, Barcelona, 2020.
3 M. Rahm, R. Hoffmann and N. W. Ashcroft, Atomic and Ionic Radii of Elements 1-96, *Chem. – Eur. J.*, 2016, **22**, 14625–14632.
4 P. Politzer, Electrostatic potential–electronic density relationships in atoms, *J. Chem. Phys.*, 1980, **72**, 3027–3033.
5 R. J. Gillespie and P. L. A. Popelier, *Chemical Bonding and Molecular Geometry*, Oxford University Press, Oxford, 2001.
6 B. Cordero, V. Gómez, A. E. Platero-Prats, M. Revés, J. Echeverría, E. Cremades, F. Barragán and S. Alvarez, Covalent Radii Revisited, *Dalton Trans.*, 2008, 2832–2838.
7 S. Alvarez, A Cartography of the Van der Waals Territory, *Dalton Trans.*, 2013, **42**, 8617–8636.
8 J. Vogt and S. Alvarez, Van der Waals Radii of the Noble Gases, *Inorg. Chem.*, 2014, **53**, 9260–9266.
9 P. Szarek and W. Grochala, Most Probable Distance between the Nucleus and HOMO Electron: The Latent Meaning of Atomic Radius from the Product of Chemical Hardness and Polarizabiity, *J. Phys. Chem. A*, 2014, **118**, 10281–10287; A. M. Mroz, A. M. Davenport, J. Sterling, J. Davis and C. H. Hendon, An electric field-based approach for quantifying effective volumes and radii of chemically affected space, *Chem. Sci.*, 2022, **13**, 6558.
10 D. M. Gil, J. Echeverría and S. Alvarez, Tetramethylammonium Cation: Directionality and Covalency in Its Interactions with Halide Ions, *Inorg. Chem.*, 2022, **61**, 9082–9095.
11 M. Pérez-Jiménez, J. Campos, J. Jover, S. Alvarez and E. Carmona, Coordination of E-C Bonds (E = Zn, Mg, Al) and the Zn-H Bonds of $(C_5Me_5)ZnH$ and $(C_5Me_5)ZnZnH$ across a Quadruply Bonded Dimolybdenum Dihydride Complex, *Organometallics*, 2022, **41**, 3225–3236.
12 J. P. M. Lommerse, A. J. Stone, R. Taylor and F. H. Allen, The Nature and Geometry of intermolecular interactions between halogens and oxygen or nitrogen, *J. Am. Chem. Soc.*, 1996, **118**, 3108–3116.
13 J. Echeverría, G. Aullón and S. Alvarez, Intermolecular interactions in group 14 hydrides: Beyond C-H···H-C contacts, *Int. J. Quantum Chem.*, 2017, **117**, e25432.
14 A. Bauzá, A. Frontera and T. J. Mooibroek, σ-Hole Interactions Involving Nitro Aromatic Ligands in Protein Structure, *Chem.–Eur. J.*, 2019, **25**, 13436–13443.
15 F. Grandinetti, *Noble Gas Chemistry. Structure, Bonding, and Gas Phase Chemistry*, Wiley-VCH, Weinheim, 2018.
16 N. Bartlett, Xenon exafluoroplatinate(V) $Xe^{+}(PtF_6)^{-}$, *Prod. Chem. Soc.*, 1962, **6**, 218.
17 A. Lobato, M. A. Salvadó, J. M. Recio, M. Taravillo and V. G. Baonza, Highs and Lows of Bond Lengths: Is There Any Limit?, *Angew. Chem., Int. Ed.*, 2021, **60**, 17028–17036.
18 T. van Mourik and J. H. van Lenthe, Benchmark full configuration interaction calculations on the helium dimer, *J. Chem. Phys.*, 1995, **102**, 7479–7483.

19 N. Zhou, Z. Lu, Q. Wu and Y. Zhang, Improved parametrization of interatomic potentials for rare gas dimers with density-based energy decomposition analysis, *J. Chem. Phys.*, 2014, **140**, 214117.
20 A. Wüest and F. Merkt, Determination of the interaction potential of the ground electronic state of Ne_2 by high-resolution vacuum ultraviolet laser spectroscopy, *J. Chem. Phys.*, 2003, **118**, 8807–8812.
21 P. R. Herman, P. E. LaRocque and B. P. Stoicheff, Vacuum ultraviolet laser spectroscopy. V. Rovibronic spectra of Ar_2 and constants of the ground and excited states, *J. Chem. Phys.*, 1088, **89**, 4535–4549.
22 M. Molski and J. Konarski, Modified Dunham potential for rovibrational diatomic systems, *Can. J. Phys.*, 1995, **73**, 59–62.
23 P. E. LaRocque, R. H. Lipson, P. R. Herman and B. P. Stoicheff, Vacuum ultraviolet laser spectroscopy. IV. Spectra of Kr_2 and constants of the ground and excited states, *J. Chem. Phys.*, 1986, **84**, 6627–6641.
24 J. Vogt, N. Vogt, R. Rudert, E. Popov, S. Schlagenhauf, K. Deutzmann and R. Kramer, New Features in the MOGADOC Database, *Struct. Chem.*, 2015, **26**, 1725–1727.
25 D. Zagorac, H. Müller, S. Ruehl, J. Zagorac and S. Rehme, Recent developments in the Inorganic Crystal Structure Database: theoretical crystal structure data and related features, *J. Appl. Crystallogr.*, 2019, **52**, 918–925.
26 R. Feltgen, H. Kirst, K. A. Köhler and H. Pauly, Unique determination of the He_2 ground state potential from experiment by use of a reliable potential model, *J. Chem. Phys.*, 1982, **76**, 2360–2378.
27 J. A. Barker, R. O. Watts, J. K. Lee, T. P. Schafer and Y. T. Lee, Interatomic potentials for krypton and xenon, *J. Chem. Phys.*, 1974, **61**, 3081–3089.
28 A. Shee, S. Knecht and T. Saue, A theoretical benchmark study of the spectroscopic constants of the very heavy rare gas dimers, *Phys. Chem. Chem. Phys.*, 2015, **17**, 10978–10986.
29 A. F. Schuch and R. L. Mills, New allotropic form of He(3), *Phys. Rev. Lett.*, 1961, **6**, 596–597.
30 J. de Smedt, W. H. Keesom and H. H. Mooy, On the crystal structure of neon, *Proc. K. Ned. Akad. Wet., Ser. B: Phys. Sci.*, 1930, **33**, 255–257.
31 D. G. Henshaw, Atomic distribution in liquid and solid neon and solid argon by neutron diffraction, *Phys. Rev.*, 1958, **111**, 1470–1475.
32 L. H. Bolz and F. A. Mauer, Measurements of the lattice constants of neon isotopes in the temperature range 4-24 K, *Adv. X-Ray Anal.*, 1962, **6**, 242–249.
33 Z. M. Geballe, H. Liu, A. K. Mishra, M. Ahart, M. Somayazulu, Y. Meng, M. Baldini and R. J. Hemley, Synthesis and Stability of Lanthanum Superhydrides, *Angew. Chem., Int. Ed.*, 2018, **57**, 688–692.
34 R. J. Hemley, C. S. Zha, A. P. Jephcoat, H. K. Mao, L. W. Finger and D. E. Cox, X-ray diffraction and equation of state of solid neon to 110 GPa, *Phys. Rev. B: Condens. Matter Mater. Phys.*, 1989, **39**, 11820–11827.
35 M. P. Housden and N. C. Pyper, The noble gas dimers as a probe of the energetic contributions of dispersion and short-range electron correlation in weakly bound system, *Mol. Phys.*, 2007, **105**, 17–18.
36 W. Caminati, Free-jet rotational spectrum and tunneling motion of difluoromethane···xenon, *J. Phys. Chem. A*, 2006, **110**, 4359–4362.
37 I. E. Collings and M. Hanfland, Packing Rearrangements in 4-Hydroxycyanobenzene Under Pressure, *Molecules*, 2019, **24**, 1759.
38 T. Higashi and K. Osaki, p-Cyanophenol, *Acta Crystallogr.*, 1977, **B33**, 607–609.
39 C. Desplanches, E. Ruiz, A. Rodríguez-Fortea and S. Alvarez, Exchange Cupling of Transition-Metal Ions through Hydrogen Bonding: A Theoretical Investigation, *J. Am. Chem. Soc.*, 2002, **124**, 5197–5205.
40 J. Mohanraj, E. Capria, L. Benevoli, A. Perucchi, N. Demitri and A. Fraleoni-Morgera, XRD- and infrared-probed anisotropic thermal expansion properties of an organic semiconducting single crystal, *Phys. Chem. Chem. Phys.*, 2018, **20**, 1984–1992.
41 M. Chokiewicz, S. Pawledzio, M. Woinska and K. Wozniak, Fragmentation and transferability in Hirshfeld atom refinement, *IUCrJ*, 2022, **9**, 298–315.
42 A. Y. Manakov, V. I. Voronin, A. V. Kurnosov, a. E. Teplykh, V. Y. Kormarov and Y. A. Dyadin, Structural Investigations of Argon Hydrates at Pressures up to 10 kbar, *J. Inclusion Phenom. Macrocyclic Chem.*, 2004, **48**, 11–18.
43 E. Cerpa, A. Krapp, A. Vela and G. Merino, The Implications of Symmetry of the External Potential on Bond Paths, *Chem. – Eur. J.*, 2008, **14**, 10232–10234.
44 M. Ilczyszyn, M. Selent and M. M. Ilczyszyn, Participation of Xenon Guest in Hydrogen Bond Network of β-Hydroquinone Crystal, *J. Phys. Chem. A*, 2012, **116**, 3206–3214.
45 Y. Morinaka, S. Sato, A. Wakamiya, H. Nikawa, N. Mizorogi, F. Tanabe, M. Murata, K. Komatsu, K. Furukawa, T. Kato, S. Nagase, T. Akasaka and Y. Murata, X-ray observation of a helium atom and placing a nitrogen atom inside $He@C_{60}$ and $He@C_{70}$, *Nat. Commun.*, 2013, **4**, 1554.
46 G. Hoffman, M. C. Walkey, J. Gräsvik, G. R. Bacanu, S. Alom, S. Bloodworth, M. E. Light, M. H. Levitt and R. J. Whitby, A Solid-State Intramolecular Wittig Reaction Enables Efficient Synthesis of Endofullerenes Including $Ne@C_{60}$, $^3He@C_{60}$, and $HD@C_{60}$, *Angew. Chem., Int. Ed.*, 2021, **60**, 8960–8966.
47 H. M. Lee, M. M. Olmstead, T. Suetsuna, H. Shimotani, N. Dragoe, R. J. Cross, K. Kitazawa and A. L. Balch, Crystallographic characterization of $Kr@C_{60}$ in $(0.09Kr@C_{60}/0.91C_{60})\cdot\{Ni^{II}(OEP)\}\cdot 2C_6H_6$, *Chem. Commun.*, 2002, 1352–1353.
48 R. Sure, R. Tonner and P. Schwerdtfeger, A Systematic Study of Rare Gas Atoms Encapsulated in Small Fullerenes using Dispersion Corrected Density Functional Theory, *J. Comput. Chem.*, 2015, **36**, 88–96.

49 A. Krapp and G. Frenking, Is This a Chemical Bond? A Theoretical Study of $Ng_2@C_{60}$ (Ng=He, Ne, Ar, Kr, Xe), *Chem. – Eur. J.*, 2007, **13**, 8256–8270.
50 E. Cerpa, A. Krapp, R. Flores-Moreno, K. J. Donald and G. Merino, Influence of Endohedral Confinement on the Electronic Interaction between He atoms: A $He_2@C_{20}H_{20}$ Case Study, *Chem. – Eur. J.*, 2009, **15**, 1985–1990.
51 A. Wueest and F. Merkt, Potential energy curves of diatomic molecular ions from high-resolution photoelectron spectroscopy. III. The low-lying ungerade states of Kr_2^+, *Mol. Phys.*, 2005, **103**, 1285–1300.
52 C. A. Reed and R. D. Bolskar, Discrete Fulleride Anions and Fullerenium Cations, *Chem. Rev.*, 2001, **100**, 1075–1120.
53 R. M. Badger, A relation between internuclear distances and bond force constants, *J. Chem. Phys.*, 1934, **2**, 128–131.
54 R. Saha, G. Jana, S. Pan, G. Merino and P. K. Chattaraj, How Far Can One Push the Noble Gases Towards Bonding?: A Personal Account, *Molecules*, 2019, **24**, 2933.
55 B. Mallada, A. Gallardo, M. Lamanec, B. de la Torre, V. Spirko, P. Hobza and P. Jellinek, Real-space imaging of anisotropic charge of σ-hole by means of Kelvin probe force microscopy, *Science*, 2021, **374**, 863–867.
56 Y. Li, Y. Lu, P. Adelhelm, M.-M. Titirici and Y.-S. Hu, Intercalation chemistry of graphite: alkali metal ions and beyond, *Chem. Soc. Rev.*, 2019, **48**, 4655–4687.
57 J. Xu, Y. Dou, Z. Wei, J. Ma, J. Deng, Y. Li, H. Liu and S. Dou, Recent Progress in Graphite Intercalation Compounds for Rechargeable Metal (Li, Na, K, Al)-Ion Batteries, *Adv. Sci.*, 2017, **4**, 1700146.
58 P. Trucano and R. Chen, Study of graphite by neutron diffraction, *Nature*, 1975, **258**, 136–137.
59 O. Dolotko, A. Sensyshyn, M. J. Muehlbauer, K. Nikolowski and H. Ehrenberg, Understanding structural changes in NMC Li-ion cells by in situ neutron diffraction, *J. Power Sources*, 2014, **255**, 197–203.
60 L. Boulet-Roblin, D. Sheptyakov, P. Borel, C. Tessier, P. Novak and C. Villevieille, Crystal structure evolution via operando neutron diffraction during long-term cycling of a customized 5 V full Li-ion cylindrical cell $LiNi_{0.5}Mn_{1.5}O_4$ vs. graphite, *J. Mater. Chem. A*, 2017, **5**, 25574–25582.
61 R. C. Asher, A lamellar compound of sodium and graphite, *J. Inorg. Nucl. Chem.*, 1959, **10**, 238–249.
62 P. Lagrange, D. Guerard and A. Herold, Sur la structure du composé KC_8, *Ann. Chim.*, 1978, **3**, 143–159.
63 P. Lagrange, D. Guerard, D. El Makrini and A. Herold, Examen radiocristallographique du composé d'insertion de premier stade RbC_8, *C. R. Seances Acad. Sci., Ser. C*, 1978, **287**, 179–182.
64 T. Janowski and P. Pulay, A Benchmark Comparison of σ/σ and π/π Dispersion: the Dimers of Naphthalene and Decalin, and Coronene and Perhydrocoronene, *J. Am. Chem. Soc.*, 2012, **134**, 17520–17525.
65 C. Boisseau, I. Simbotin and R. Côté, Macrodimers: ultralong range Rydberg molecules, *Phys. Rev. Lett.*, 2002, **88**, 133004.
66 V. Bendkowsky, B. Butscher, J. Nipper, J. P. Shafer, R. Löw and T. Pfau, Observation of ultralong-range Rydberg molecules, *Nature*, 2009, **458**, 1005–1008.
67 C. H. Greene, A. S. Dickinson and H. R. Sadeghpour, Creation of Polar and Nonpolar Ultra-Long-Range Rydberg Molecul, *Phys. Rev. Lett.*, 2000, **85**, 2458–2461.
68 N. Zuber, V. S. V. Anasuri, M. Berngruber, Y.-Q. Zou, F. Meinert, R. Löw and T. Pfau, Observation of a molecular bond betweenions and Rydberg atoms, *Nature*, 2022, **605**, 454–456.
69 J. Simons and M. Gutowski, Double-Rydberg Molecular Anions, *Chem. Rev.*, 1991, **91**, 669–677.
70 A. C. J. Lawson, R. B. J. Roof, J. D. Jorgensen, B. Morosin and J. E. Schirber, Structure of ND_4F - II, *Acta Crystallogr., Sect. B: Struct. Sci.*, 1989, **45**, 212–218.
71 M. W. Crofton and T. Oka, Observation of forbidden transitions of ammonium ion (NH_4^+) ν_3 band and determination of ground state rotational constants. Observation of ν_3 band allowed transitions of ND_4^+, *J. Chem. Phys.*, 1987, **35**, 5893.
72 J. Melin, G. Seabra and J. V. Ortiz, in *Theoretical Aspects of Chemical Reactivity*, ed. A. Toro-Labbé, Elsevier B. V., Amsterdam, 2007, pp. 87–100.
73 A. I. Boldyrev and J. Simons, On the Possibility of Mixed Rydberg-Valence Bonds, *J. Phys. Chem. A*, 1999, **103**, 3575–3580.
74 A. I. Boldyrev and J. Simons, Rydberg bonding in ammonium dimer ($(NH_4)_2$), *J. Phys. Chem.*, 1992, **96**, 8840–8843.
75 P. Pyykkö, Strong Closed-Shell Interactions in Inorganic Chemistry, *Chem. Rev.*, 1997, **97**, 597–636.
76 H. Schmidbaur and H. G. Raubenheimer, Excimer and Exciplex Formation in Gold(I) Complexes Preconditioned by Aurophilic Interactions, *Angew. Chem., Int. Ed.*, 2020, **59**, 14748–14771.
77 P. K. Mehrotra and R. Hoffmann, Cu(I)-Cu(I) Interactions. Bonding Relationships in $d^{10}d^{10}$ Systems, *Inorg. Chem.*, 1978, **17**, 2187–2189.
78 Y. Jiang, S. Alvarez and R. Hoffmann, Binuclear and Polynuclear Gold(I) Complexes, *Inorg. Chem.*, 1985, **24**, 749–757.
79 A. Carvajal, X.-Y. Liu, P. Alemany, J. J. Novoa and S. Alvarez, Ligand Effects and Dimer Formation in Bicoordinate Copper(I) Complexes, *Int. J. Quantum Chem.*, 2002, **86**, 100–105.
80 J. Echeverría, J. Cirera and S. Alvarez, Mercurophilic interactions: A Theoretical Study of the Importance of the Ligands, *Phys. Chem. Chem. Phys.*, 2017, **19**, 11645–11654.
81 J. J. Novoa, G. Aullón, P. Alemany and S. Alvarez, On the Bonding Nature of the M···M Interactions in Dimers of Square-Planar Pt(II) and Rh(I) Complexes, *J. Am. Chem. Soc.*, 1995, **117**, 7169–7171.
82 G. Aullón, P. Alemany and S. Alvarez, On the Existence of a Pyramidality Effect in $d^8\cdots d^8$ Contacts. Theoretical Study and Structural Correlation, *Inorg. Chem.*, 1996, **35**, 5061–5067.

83 G. Aullón and S. Alvarez, Chain Conformation and Metal⋯Metal Contacts in Dimers and Stacks of d^8-ML_4 Complexes: Electronic Effects, *Chem. – Eur. J.*, 1997, **3**, 655–664.

84 A. Kobayashi, Y. Sasaki and H. Kobayashi, Structural Studies of Commensurate Peierls State of $Rb_{1.67}[Pt(C_2O_4)_2]\cdot 1.5H2O$, *Bull. Chem. Soc. Jpn.*, 1979, **52**, 3682–3691.

85 A. E. Pullen, C. Faulmann, H.-L. Liu, D. B. Tanner, K. A. Abboud and J. R. Reynolds, Electrocrystallization and characterization of phosphonium-based radical anion salts $[MePh_3P]$ $[Pd(dmit)_2]_3$ and $[Ph4_P]$ $[Pd(dmit)_2]_3$ (dmit = 1,3-dithiole-2-thione-4,5-dithiolate). Comparison with related Pd and Ni isologues, *Inorg. Chim. Acta*, 1998, **282**, 90–95.

86 A. Galstyan, P. J. Sanz-Miguel, J. Wolf, E. Freisinger and B. Lippert, Discrete Molecular Squares $\{[(en)M(CN)]_4\}^{4+}$ Derived from $[(en)M(CN)_2]$ (M = Pt^{II}, Pd^{II}), *Eur. J. Inorg. Chem.*, 2011, 1649–1666.

87 K. Kitano, R. Tanaka, T. Kimura, T. Tsuda, S. Shimizu, H. Takagi, T. Nishioka, D. Shiomi, A. Ichimura, I. Kinoshita, K. Isobe and S. Ooi, Lantern-type dinuclear $Cr^{III}Pt^{II}$ and $V^{IV}Pt^{II}$ complexes bridged by pyridine-2-thiolate. Synthesis and characterization, *J. Chem. Soc., Dalton Trans.*, 2000, 995–1000.

88 K. Meelich, M. Galanski, V. B. Arion and B. K. Keppler, Bis(2-amino alcohol-κN)dicarboxylatoplatinum(II) Complexes – Elegant Synthesis via Ring-Opening of Bis(2-amino alcoholato-κ^2N,O)platinum(II) Species with Dicarboxylic Acids, *Eur. J. Inorg. Chem.*, 2006, 2476–2483.

89 B. T. Watson, M. Vanga, A. Noonikara-Poyil, A. Muoz-Castro and H. V. R. Dias, Copper(I), Silver(I), and Gold(I) Ethylene Complexes of Fluorinated and Boron-Methylated Bis- and Tris(pyridyl)borate Chelators, *Inorg. Chem.*, 2023, **62**, 1636–1648.

90 T. Nguyen, A. D. Sutton, M. Brynda, J. C. Fettinger, G. J. Long and P. P. Power, Synthesis of a Stable Compound with Fivefold Bonding Between Two Chromium(I) Centers, *Science*, 2005, **844**, 844–847.

91 R. Wolf, C. Ni, T. Nguyen, M. Brynda, G. J. Long, A. D. Sutton, R. C. Fischer, J. C. Fettinger, M. Hellman, L. Pu and P. P. Power, Substituent Effects in Formally Quintuple-Bonded ArCrCrAr Compounds (Ar = Terphenyl) and Related Species, *Inorg. Chem.*, 2007, **46**, 11277–11290.

92 M. Carrasco, M. Faust, R. Peloso, A. Rodríguez, J. López-Serrano, E. Alvarez, C. Maya, P. P. Power and E. Carmona, Quadruply bonded dimolybdenum complexes with highly unusual geometries and vacant coordination sites, *Chem. Commun.*, 2012, **48**, 3954–3956.

93 M. Carrasco, I. Mendoza, M. Faust, J. López-Serrano, R. Peloso, A. Rodríguez, E. Alvarez, C. Maya, P. P. Power and E. Carmona, Terphenyl Complexes of Molybdenum and Tungsten with Quadruple Metal–Metal Bonds and Bridging Carboxylate Ligands, *J. Am. Chem. Soc.*, 2914, **136**, 9173–9180.

94 M. Carrasco, I. Mendoza, E. Alvarez, A. Grirrane, C. Maya, R. Peloso, A. Rodríguez, A. Falceto, S. Alvarez and E. Carmona, Experimental and Computational Studies of the Molybdenum-Flanking Arene Interaction in Quadruply Bonded Dimolybdenum Complexes with Terphenyl Ligands, *Chem. – Eur. J.*, 2015, **21**, 410–421.

95 A. Velian, S. Lin, J. M. Miller, M. W. Day and T. Agapie, Synthesis and C−C Coupling Reactivity of a Dinuclear NiI−NiI Complex Supported by a Terphenyl Diphosphine, *J. Am. Chem. Soc.*, 2010, **132**, 6296–6297.

96 G. A. Landrum and R. Hoffmann, Secondary Bonding between Chalcogens or Pnicogens and Halogens, *Angew. Chem., Int. Ed.*, 1998, **37**, 1887–1890.

97 H. A. Jahn and E. Teller, Stability of Polyatomic Molecules in Degenerate Electronic States. I. Orbital Degeneracy, *Proc. R. Soc. London, Ser. A*, 1937, **161**, 220–235.

98 I. B. Bersuker, *The Jahn-Teller effect*, Cambridge University Press, Cambridge, UK, 2006.

99 M. A. Halcrow, Jahn-Teller distortions in transition metal compounds, and their importance in functional molecular and inorganic materials, *Chem. Soc. Rev.*, 2013, **42**, 1784–1795.

100 J. Echeverría, E. Cremades, A. J. Amoroso and S. Alvarez, Jahn-Teller Distortions of Six-coordinate Copper(II) Compounds: Cis or Trans?, *Chem. Commun.*, 2009, 4242–4244.

101 W. Grochala, Plasticity of the coordination sphere of Ag^{2+}, *Phys. Status Solidi*, 2006, **243**, R81–R83.

102 T. Hansen, X. Sun, M. Dalla Tiezza, W.-J. van Zeist, J. N. P. van Stralen, D. P. Geerke, L. P. Wolters, J. Poater, T. A. Hamlin and F. M. Bickelhaupt, C-X Bond Activation by Palladium: Steric Shielding versus Steric Attraction, *Chem. – Eur. J.*, 2022, **28**, 3202201093.

103 C. F. Matta, J. Hernández-Trujillo, T.-H. Tang and R. F. W. Bader, Hydrogen–Hydrogen Bonding: A Stabilizing Interaction in Molecules and Crystals, *Chem. – Eur. J.*, 2003, **9**, 1940–1951.

104 J. Poater, M. Solà and F. M. Bickelhaupt, Hydrogen–Hydrogen Bonding in Planar Biphenyl, Predicted by Atoms-In-Molecules Theory, Does Not Exist, *Chem. – Eur. J.*, 2006, **12**, 2889–2895.

105 J. Poater, R. Visser, M. Solà and F. M. Bickelhaupt, Polycyclic Benzenoids: Why Kinked is More Stable than Straight, *J. Org. Chem.*, 2007, **72**, 1134–1142.

106 S. Grimme, C. Mück-Lichtenfeld, G. Erker, G. Kehr, H. Wang, H. Beckers and H. Willner, When Do Interacting Atoms Form a Chemical Bond? Spectroscopic Measurements and Theoretical Analyses of Dideuteriophenanthrene, *Angew. Chem., Int. Ed.*, 2009, **48**, 2592–2595.

107 A. I. Proktavatilov and A. P. Isakina, An X-ray powder diffraction study of crystalline α-methane-d4, *Acta Crystallogr., Sect. B: Struct. Crystallogr. Cryst. Chem.*, 1980, **36**, 1576–1580.

108 G. J. H. van Nes and A. Vos, Single-crystal structures and electron density distributions of ethane, ethylene and acetylene. I. Single-crystal X-ray structure determinations of two modifications of ethane, *Acta Crystallogr., Sect. B: Struct. Crystallogr. Cryst. Chem.*, 1978, **34**, 1947–1956.

109 G. J. H. van Nes and A. Vos, Single-crystal structures and electron density distributions of ethane, ethylene and acetylene. III. Single-crystal X-ray structure determination of ethylene at 85 K, *Acta Crystallogr., Sect. B: Struct. Crystallogr. Cryst. Chem.*, 1979, **35**, 2593–2601.

110 A. Stein, C. W. Lehmann and P. Luger, Crystal structure of cyclobutane at 117 K, *J. Am. Chem. Soc.*, 1992, **114**, 7684–7687.

111 F. E. Kühn, M. Groarke, E. Bencze, E. Herdtweck, A. Prazeres, A. M. Santos, M. J. Calhorda, C. C. Romão, I. S. Gonçalves, A. D. Lopes and M. Pillinger, Octahedral Bipyridine and Bipyrimidine Dioxomolybdenum(VI) Complexes: Characterization, Application in Catalytic Epoxidation, and Density Functional Mechanistic Study, *Chem. – Eur. J.*, 2002, **8**, 2370–2383.

112 H. Imgartinger, A. Goldmann, R. Jahn, M. Nixdorf, H. Rodewald, G. Maier, K.-D. Malsch and R. Emrich, Tetra-tert-butyltetrahedrane—Crystal and Molecular Structure, *Angew. Chem., Int. Ed.*, 1984, **23**, 993–994.

113 S. Rösel, H. Quanz, C. Legomenn, J. Becker, E. Mossou, L. Cañadillas-Delgado, E. Aldeweyher, S. Grimme and P. R. Schreiner, London Dispersion Enables the Shortest Intermolecular Hydrocarbon H···H Contact, *J. Am. Chem. Soc.*, 2017, **139**, 7428–7431.

114 M. Brookhart and M. L. H. Green, Carbon-hydrogen-transition metal bonds, *J. Organomet. Chem.*, 1983, **250**, 395–408.

115 M. J. Calhorda, Weak hydrogen bonds: theoretical studies, *Chem. Commun.*, 2000, 801–809.

116 W. Scherer and G. S. McGrady, Agostic Interactions in d^0 Metal Alkyl Complexes, *Angew. Chem., Int. Ed.*, 2005, **43**, 1782.

117 E. Clot and O. Eisenstein, Agostic Interactions from a computational Perspective: One Name, Many Interpretations, *Struct. Bonding*, 2004, **113**, 1–36.

118 M. Brookhart, M. L. H. Green and G. Parkin, Agostic interactions in transition metal compounds, *Proc. Natl. Acad. Sci. U. S. A.*, 2007, **104**, 6908–6914.

119 Q. Lu, F. Neese and G. Bistoni, London dispersion effects in the coordination and activation of alkanes in σ-complexes: a local energy decomposition study, *Phys. Chem. Chem. Phys.*, 2019, **21**, 11569–11577.

120 R. D. Young, Characterisation of Alkane σ-Complexes, *Chem. – Eur. J.*, 2014, **20**.

121 R. H. Crabtree, E. M. Holt, M. Lavin and S. M. Morehouse, Inter- vs. intramolecular carbon-hydrogen activation: a carbon-hydrogen-iridium bridge in $[IrH(mq)L_2]BF_4$ and a CH + M → CMH reaction trajectory, *Inorg. Chem.*, 1985, **24**, 1986–1992.

122 J. Fernández-Valparís and S. Alvarez, Design of a Structural Database for Homoleptic Transition Metal Complexes, *Struct. Chem.*, 2015, **26**, 1715–1723.

123 F. M. Chadwick, N. H. Rees, A. S. Weller, T. Krämer, M. Iannuzzi and S. A. Macgregor, A Rhodium–Pentane Sigma-Alkane Complex: Characterization in the Solid State by Experimental and Computational Techniques, *Angew. Chem., Int. Ed.*, 2016, **55**, 3677–3681.

124 S. D. Pike, F. M. Chadwick, N. H. Rees, M. P. Scott, A. S. Weller, T. Kramer and S. A. Macgregor, Solid-State Synthesis and Characterization of σ-Alkane Complexes, $[Rh(L_2)(\eta^2,\eta^2\text{-}C_7H_{12})][BArF_4]$ (L_2 = Bidentate Chelating Phosphine), *J. Am. Chem. Soc.*, 2015, **137**, 820–833.

125 S. Kleinhenz, V. Pfennig and K. Seppelt, Preparation and Structures of $[W(CH_3)_6]$, $[Re(CH_3)_6]$, $[Nb(CH3)_6]^-$, and $[Ta(CH_3)_6]^-$, *Chem. – Eur. J.*, 1998, **4**, 1687–1691.

126 S. H. Crosby, G. J. Clarkson and J. P. Rourke, A Delicate Balance between sp^2 and sp^3 C-H Bond Activation: A Pt(II) Complex with a Dual Agostic Interaction, *J. Am. Chem. Soc.*, 2009, **131**, 14142–14143.

127 W. Scherer, T. Priermeier, A. Haaland, H. V. Volden, G. S. McGrady, A. J. Downs, R. Boese and D. Bläser, Molecular Structures of $EtTiCl_3$ and $EtTiCl_3$(dmpe) (dmpe = $Me_2PCH_2CH_2PMe_2$): New Insights into β-Agostic Bonding, *Organometallics*, 1998, **17**, 4406–4412.

128 E. D. Bloch, W. L. Queen, R. Krishna, J. M. Zadorzny, C. M. Brown and J. R. Long, Hydrocarbon Separations in a Metal–Organic Framework with Open Iron(II) Coordination Sites, *Science*, 2012, **335**, 1606–1610.

129 V. Lavallo, Y. Canac, A. DeHope, B. Donadieu and G. Bertrand, A Rigid Cyclic (Alkyl)(amino)carbene Ligand Leads to Isolation of Low-Coordinate Transition-Metal Complexes, *Angew. Chem., Int. Ed.*, 2005, **44**, 7236–7239.

130 G. Bruno, S. Lanza and F. Nicolò, Structure of $[Pt(C_6H_5)_2$(btz-N,N')].$CHCl_3$, btz = 2,2'-bi-5,6-dihydro-4H-1,3-thiazine, *Acta Crystallogr.*, 1990, **C46**, 765–767.

131 T. M. Boyd, B. E. Tegner, G. J. Tizzard, A. J. Martínez-Martínez, S. E. Neale, M. A. Hayward, S. J. Coles, S. A. Macgregor and A. S. Weller, A Structurally Characterized Cobalt(I) σ-Alkane Complex, *Angew. Chem., Int. Ed.*, 2019, **59**, 6177–6181.

132 A. J. Bukvic, A. L. Burnage, G. J. Tizzard, A. J. Martínez-Martínez, A. I. McKay, N. H. Rees, B. E. Tegner, T. Krämer, H. Fish, M. R. Warren, S. J. Coles, S. A. Macgregor and A. S. Weller, A Series of Crystallographically Characterized Linear and Branched σ-Alkane Complexes of Rhodium: From Propane to 3-Methylpentane, *J. Am. Chem. Soc.*, 2021, **143**, 5106–5120.

133 A. J. Martínez-Martínez, B. E. Tegner, A. I. McKay, A. J. Bukvic, N. H. Rees, G. J. Tizzard, S. J. Coles, M. R. Warren, S. A. Macgregor and A. S. Weller, Modulation of σ-Alkane Interactions in $[Rh(L_2)(alkane)]$+ Solid-State Molecular Organometallic (SMOM) Systems by Variation of the Chelating Phosphine and Alkane: Access to η^2,η^2-σ-Alkane Rh(I), η^1-σ-Alkane Rh(III) Complexes, and Alkane Encapsulation, *J. Am. Chem. Soc.*, 2019, **140**, 14958–14970.

134 L. R. Doyle, M. R. Galpin, S. K. Furfari, B. E. Tegner, A. J. Martínez-Martínez, A. C. Whitwood, S. A. Hicks, G. C. Lloyd-Jones, S. A. Macgregor and A. S. Weller, Inverse Isotope Effects in Single-Crystal to Single-Crystal Reactivity and the Isolation of a Rhodium Cyclooctane σ-Alkane Complex, *Organometallics*, 2022, **41**, 284–292.

135 A. I. McKay, T. Krämer, N. H. Rees, A. L. Thompson, K. E. Christensen, S. A. Macgregor and A. S. Weller,

Formation of a σ-alkane Complex and a Molecular Rearrangement in the Solid-State: $[Rh(Cyp_2PCH_2CH_2PCyp_2)(\eta^2{:}\eta^2\text{-}C_7H_{12})][BAr^F{}_4]$, *Organometallics*, 2017, **36**, 22–25.

136 B. Eguillor, M. A. Esteruelas, V. Lezáun, M. Oliván, E. Oñate, J.-Y. Tsay and C. Xia, A Capped Octahedral MHC_6 Compound of a Platinum Group Metal, *Chem. – Eur. J.*, 2016, **22**, 9106–9110.

137 G. J. Kubas, R. R. Ryan, B. I. Swanson, P. J. Vergamini and H. J. Wasserman, Characterization of the First Examples of Isolable Molecular Hydrogen Complexes, $M(CO)_3(PR_3)_2(H_2)$ (M = Mo, W; R = Cy,/-Pr). Evidence for a Side-on Bonded H_2 Ligand, *J. Am. Chem. Soc.*, 1984, **106**, 451–452.

138 G. J. Kubas, Metal–dihydrogen and σ-bond coordination: the consummate extension of the Dewar–Chatt–Duncanson model for metal–olefin π bonding, *J. Organomet. Chem.*, 2001, **635**, 37–68.

139 F. Maseras, A. Lledós, E. Clot and O. Eisenstein, Transition Metal Polyhidrides: From Qualitative Ideas to Reliable Computational Studies, *Chem. Rev.*, 2000, **100**, 601–636.

140 M. Yousufuddin, T. B. Wen, S. A. Mason, G. J. McIntyre, G. Jia and R. Bau, A Neutron Diffraction Study of $[OsClH_3(PPh_3)_3]$: A Complex Containing a Highly "Stretched" Dihydrogen Ligand, *Angew. Chem., Int. Ed.*, 2005, **44**, 7227–7230.

141 A. A. Zuzek and G. Parkin, Si–H and Si–C Bond Cleavage Reactions of Silane and Phenylsilanes with $Mo(PMe_3)_6$: Silyl, Hypervalent Silyl, Silane, and Disilane Complexes, *J. Am. Chem. Soc.*, 2014, **136**, 8177–8180.

142 W. Chen, S. Shimada and M. Tanaka, Synthesis and Structure of Formally Hexavalent Palladium Complexes, *Science*, 2002, **295**.

143 P. Gualco, A. Amgoune, K. Miqueu, S. Ladeira and D. Bourissou, A Crystalline σ Complex of Copper, *J. Am. Chem. Soc.*, 2011, **133**, 4257–4259.

144 S. Shimada, M. L. N. Rao, T. Hayashi and M. Tanaka, Isolation of Dinuclear (μ-Silylene)(silyl)nickel Complexes and Si−Si Bond Formation on a Dinuclear Nickel Framework, *Angew. Chem., Int. Ed.*, 2001, **40**, 213–216.

145 G. A. Jeffrey, *An Introduction to Hydrogen Bonding*, Oxford University Press, New York, 1997.

146 G. R. Desiraju and T. Steiner, *The Weak Hydrogen Bond. Its Structural Chemistry and Biology*, Oxford University Press, Oxford, 1999.

147 T. Steiner, The Hydrogen Bond in the Solid State, *Angew. Chem., Int. Ed.*, 2002, **41**, 48–76.

148 S. J. Grabowski and W. A. Sokalski, Different types of hydrogen bonds: correlation analysis of interaction energy components, *J. Phys. Org. Chem.*, 2005, **18**, 779–784.

149 J. W. Steed and J. L. Atwood, *Supramolecular Chemistry*, Wiley, Hoboken, NJ, 3rd edn, 2022.

150 F. Dankert, K. Reuter, C. Donsbach and C. von Hänisch, A structural study of alkaline earth metal complexes with hybrid disila-crown ethers, *Dalton Trans.*, 2017, **46**, 8727–8735.

151 K. Kawaguchi and E. Hirota, Diode laser spectroscopy of the v_3 and v_2 bands of FHF^- in 1300 cm^{-1} region, *J. Chem. Phys.*, 1987, **87**, 6838.

152 K. Kawaguchi and E. Hirota, Infrared diode laser spectroscopy of FDF^-, *J. Mol. Struct.*, 1995, **352/353**, 389–394.

153 K. Kawaguchi and E. Hirota, Infrared diode laser study of the hydrogen bifluoride anion: FHF^- and FDF^-, *J. Chem. Phys.*, 1986, **84**, 2953.

154 J. A. Ibers, Refinement of Peterson and Levy's neutron diffraction data on KHF_2, *J. Chem. Phys.*, 1964, **40**, 402–404.

155 A. R. Mahjoub, D. Leopold and K. Seppelt, Iodine pentafluoride - hydrogen fluoride co-crystallisates, directed weak interactions, *Eur. J. Solid State Inorg. Chem.*, 1992, **29**, 635–647.

156 B. Dereka, Q. Yu, N. H. C. Lewis, W. B. Carpenter, J. M. Bowman and A. Tokmakoff, Crossover from hydrogen to chemical bonding, *Science*, 2021, **371**, 160–164.

157 A. Haaland, *Molecules and Models. The Molecular Structures of Main Group element Compounds*, Oxford University Press, Oxford, 2008.

158 J. O. Lundgren and I. Olovsson, Hydrogen Bond Studies. XV. The Crystal Structure of Hydrogen Chloride Dihydrate, *Acta Crystallogr.*, 1967, **23**, 966–971.

159 R. Attig and J. M. Williams, The $H_5O_2^+$ Ion in Hydrogen Bromide Dihydrate, *Angew. Chem., Int. Ed.*, 1976, **15**, 491–492.

160 N. Lebrun, F. Mahe, J. Lamiot, M. Foulon and J. C. Petit, A new crystalline phase of nitric acid dihydrate, *Acta Crystallogr., Sect. C: Cryst. Struct. Commun.*, 2001, **57**, 1129–1131.

161 G. Gilli and P. Gilli, *The Nature of the Hydrogen Bond*, Oxford University Press, Oxford, 2009.

162 H. A. Fargher, T. J. Sherbow, M. M. Haley, D. W. Johnson and M. D. Pluth, C–H···S hydrogen bonding interactions, *Chem. Soc. Rev.*, 2022, **51**, 1454.

163 H. Keil, R. Herbst-Irmer, S. Rathjen, C. Girschik, T. Müller and D. Stalke, Si–H···Se Chalcogen–Hydride Bond Quantified by Diffraction and Topological Analyses, *Inorg. Chem.*, 2022, **61**, 6319–6325.

164 L. d. A. Santos, T. C. Ramalho, T. A. Hamlin and F. M. Bickelhaupt, Intermolecular Covalent Interactions: Nature and Directionality, *Chem. – Eur. J.*, 2023, **29**, e202203791.

165 A. Bauzà, T. J. Mooibroek and A. Frontera, Tetrel-Bonding Interaction: Rediscovered Supramolecular Force?, *Angew. Chem., Int. Ed.*, 2013, **52**, 12317–12321.

166 Y. Mo, D. Danovich and S. Shaik, The roles of charge transfer and polarization in non-covalent interactions: a perspective from ab initio valence bond methods, *J. Mol. Model.*, 2022, **28**, 274.

167 S. J. Grabowski, Pnicogen and tetrel bonds—tetrahedral Lewis acid centres, *Struct. Chem.*, 2019, **30**, 1141–1152.

168 E. Bartashevich, Y. Matveychuk and V. Tsirelson, Identification of the Tetrel Bonds between Halide Anions and Carbon Atom of Methyl Groups Using Electronic Criterion, *Molecules*, 2019, **24**, 1083.

169 C. Wang, D. Danovich, Y. Mo and S. Shaik, On The Nature of the Halogen Bond, *J. Chem. Theory Comput.*, 2014, **10**, 3726–3737.

170 H. I. Bioemink, S. A. Cooke, J. H. Holloway and A. C. Legon, Rotational spectroscopy of mixtures of trimethylamine and fluorine: Identification of the ion pair $[(CH_3)_3NF]^+\cdots F^-$ in the gas phase, *Angew. Chem., Int. Ed. Engl.*, 1997, **36**, 1340–1342.

171 P. Metrangolo and G. Resnati, Halogen Bonding: A Paradigm in Supramolecular Chemistry, *Chem. – Eur. J.*, 2001, **7**, 2511–2519.

172 J. S. Murray and P. Politzer, Interaction and Polarization Energy Relationships in σ-Hole and π-Hole Bonding, *Crystals*, 2020, **10**, 76.

173 L. Pauling, The Nature of the Chemical Bond. II. The One-electron Bond and the Three-electron Bond, *J. Am. Chem. Soc.*, 1931, **53**, 3225.

174 Ø. Burrau, Berechnung des Energiewertes des Wasserstoffmolekel-Ions (H_2^+) im Normalzustand, *Naturwissensch*, 1927, **15**, 16–17.

175 S. Stimson, M. Evans, C.-W. Hsu and C. Y. Ng, Rotationally resolved vacuum ultraviolet pulsed field ionization-photoelectron vibrational bands for HD^+ ($X^2\Sigma_g^+$, v^+=0-20), *J. Chem. Phys.*, 2007, **126**, 164303.

176 X. He, S. Lv, T. Hayat and K. Han, Potential Energy Surfaces for the First Two Lowest-Lying Electronic States of the LiH_2^+ System, and Dynamics of the $H^+ + LiH \rightleftharpoons H_2^+ + Li$ Reactions, *J. Phys. Chem. A*, 2016, **120**, 2459–2470.

177 A. Carrington, C. H. Pyne, A. M. Shaw, S. M. Taylor, J. M. Hutson and M. M. Law, Microwave spectroscopy and interaction potential of the long-range $H\cdots Kr^+$ ion: An example of Hund's case, *J. Chem. Phys.*, 1996, **105**, 8602–8614.

178 M. W. Johnson, E. Sandor and E. Arzi, The crystal structure of deuterium fluoride, *Acta Crystallogr., Sect. B: Struct. Crystallogr. Cryst. Chem.*, 1975, **31**, 1998–2003.

179 E. Sandor and R. F. C. Farrow, Crystal structure of solid hydrogen chloride and deuterium chloride, *Nature*, 1967, **213**, 171–172.

180 A. Ikram, B. H. Torrie and B. M. Powell, Structures of solid deuterium bromide and deuterium iodide, *Mol. Phys.*, 1993, **79**, 1037–1049.

181 S. Biswas, I. M. Oppel and H. F. Bettinger, Synthesis and Structural Characterization of 9-Azido-9-Borafluorene: Monomer and Cyclotrimer of a Borole Azide, *Inorg. Chem.*, 2010, **49**, 4499–4506.

182 A. Hübner, A. M. Diehl, M. Bolte, H.-W. Lerner and M. Wagner, High-Temperature Reactivity of the Strongly Electrophilic Pristine 9H-9-Borafluorene, *Organometallics*, 2013, **32**, 6827–6833.

183 J. D. Hoefelmeyer and F. P. Gabbai, An Intramolecular Boron-Boron One-Electron σ-Bond, *J. Am. Chem. Soc.*, 2000, **122**, 9054–9055.

184 A. Hübner, A. M. Diehl, M. Diefenbach, B. Endeward, M. Bolte, H.-W. Lemer, M. C. Holthausen and M. Wagner, Confirmed by X-ray Crystallography: The B·B One-Electron σ Bond, *Angew. Chem., Int. Ed.*, 2014, **53**, 4832–4835.

185 D. D. Danielson and K. Hedberg, The effect of temperature on the structure of gaseous molecules. 4. Molecular structure and barrier to internal rotation for diboron tetrabromide, *J. Am. Chem. Soc.*, 1979, **101**, 3199–3203.

186 N. Wiberg, T. Blank, K. Amelunxen, H. Noth, J. Knizek, T. Habereder, W. Kaim and M. Wanner, On the Gallanyls $R^*_3Ga_2\cdot$ and $R^*_4Ga_3\cdot$ As Well As Gallanides $R^*_3Ga_2^-$ and $R^*_4Ga_3^-$ ($R^* = SitBu_3$) – Syntheses, Characterization, Structures, *Eur. J. Inorg. Chem.*, 2001, 1719–1727.

187 C. Pluta, K.-R. Pörschke, C. Kruger and K. Hildenbrand, An Al–Al One-Electron π Bond, *Angew. Chem., Int. Ed.*, 1993, **32**, 388–390.

188 X. He, R. A. Bartlett, M. M. Olmstead, K. Ruhlandt-Senge, B. E. Sturgeon and P. P. Power, Reduction of a Tetraaryldigallane to Afford a Radical Anion with Ga–Ga Multiple Bonding Character, *Angew. Chem., Int. Ed.*, 1993, **32**, 717–719.

189 Z. Feng, Y. Fang, H. Ruan, Y. Zhao, G. Tan and X. Wang, Stable Radical Cation and Dication of an N-Heterocyclic Carbene Stabilized Digallene: Synthesis, Characterization and Reactivity, *Angew. Chem., Int. Ed.*, 2020, **59**, 6769–6774.

190 S. Bontemps, G. Bouhadir, W. Gu, M. Mercy, C.-H. Chen, B. M. Foxman, L. Maron, O. V. Ozerov and D. Bourissou, Metallaboratranes Derived from a Triphosphanyl–Borane: Intrinsic C_3 Symmetry Supported by a Z-Type Ligand, *Angew. Chem., Int. Ed.*, 2008, **47**, 1481–1484.

191 M.-E. Moret, L. Zhang and J. C. Peters, A Polar Copper–Boron One-Electron σ-Bond, *J. Am. Chem. Soc.*, 2013, **135**, 3792–3795.

192 M. Sircoglou, S. Bontemps, G. Bouhadir, N. Saffon, K. Miqueu, W. Gu, M. Mercy, C.-H. Chen, B. M. Foxman, L. Maron, O. V. Ozerov and d. Bourissou, Group 10 and 11 Metal Boratranes (Ni, Pd, Pt, CuCl, AgCl, AuCl, and Au^+) Derived from a Triphosphine−Borane, *J. Am. Chem. Soc.*, 2008, **130**, 16729–16738.

193 B. J. Graziano, T. R. Scott, M. V. Vollmer, M. J. Dorantes, V. G. Young, E. Bill, L. Gagliardi and C. C. Lu, One-electron bonds in copper–aluminum and copper–gallium complexes, *Chem. Sci.*, 2022, **13**, 6525–6531.

194 I. Østrom, A. O. Ortolan, F. S. S. Schneider, G. F. Caramori and R. L. T. Parreira, Quest for Insight into Ultrashort C−H$\cdots\pi$ Proximities in Molecular "Iron Maidens", *J. Org. Chem.*, 2018, **83**, 5114–5122.

195 N. A. Dodd, Y. Cao, J. Bacsa, E. C. Towles, T. G. Gray and J. P. Sadighi, Three-Electron Nickel(I)/Nickel(0) Half-Bond, *Inorg. Chem.*, 2022, **61**, 16317.

196 D. Oliveira de Sousa and M. A. C. Nascimento, Are One-Electron Bonds Any Different from Standard Two-Electron Covalent Bonds?, *Acc. Chem. Res.*, 2017, **50**, 2264–2272.

197 H. Braunschweig, R. D. Dewhurst, K. Hammond, J. Mies, K. Radacki and A. Vargas, Ambient-Temperature Isolation of a Compound with a Boron-Boron Triple Bond, *Science*, 2012, **336**, 1420–1422.

198 J. Böhnke, H. Braunschweig, P. Constantinidis, T. Dellermann, W. C. Ewing, I. Fischer, K. Hammond,

F. Hupp, J. Mies, H.-C. Schmitt and A. Vargas, Experimental Assessment of the Strengths of B–B Triple Bonds, *J. Am. Chem. Soc.*, 2015, **137**, 1766–1769.

199 J. Echeverría, G. Aullón, D. Danovich, S. Shaik and S. Alvarez, Dihydrogen contacts in alkanes are subtle but not faint, *Nat. Chem.*, 2011, **3**, 323–330.

200 K. M. Marczenko, H. P. A. Mercier and G. J. Schrobilgen, A Stable Crown Ether Complex with a Noble-Gas Compound, *Angew. Chem., Int. Ed.*, 2018, **57**, 12448–12452.

201 J. T. Goettel, H. P. A. Mercier and G. J. Schrobilgen, *J. Fluorine Chem.*, 2018, **211**, 60.

202 R. H. Crabtree and M. Lavin, A Structural Analysis of the Semibridging Carbonyl, *Inorg. Chem.*, 1986, **25**, 805–812.

203 M. E. Moussa, S. Welsch, L. Dütsch, M. Piesch, S. Reichl, M. Seidl and M. Scheer, The Triple-Decker Complex $[Cp^*Fe(\mu,\eta^5{:}\eta^5\text{-}P_5)Mo(CO)_3]$ as a Building Block in Coordination Chemistry, *Molecules*, 2019, **24**, 325.

204 J. K. Puri, R. Singh and V. K. Chahal, Silatranes: a review on their synthesis, structure, reactivity and applications, *Chem. Soc. Rev.*, 2011, **40**, 1791–1840.

205 S. Shaik, D. Danovich, W. Wu and A. Haaland, Charge-shift bonding and its manifestations in chemistry, *Nat. Chem.*, 2009, **1**, 443–449.

206 R. Carrasco, G. Aullón and S. Alvarez, X-X Through-Cage Bonding in Cu, Ni and Cr Complexes with M_3X_2 Cores (X = S, As), *Chem. – Eur. J.*, 2009, **15**, 536–546.

207 D. J. Liptrot and P. P. Power, London dispersion forces in sterically crowded inorganic and organometallic molecules, *Nat. Rev. Chem.*, 2017, **1**, 0004.

208 P. R. Schreiner, L. V. Chernish, P. A. Gunchenko, E. Y. Tikhonchuk, H. Hausmann, M. Serafin, S. Schlecht, J. E. P. Dahl, R. M. K. Carlson and A. a. Fokin, Overcoming lability of extremely long alkane carbon–carbon bonds through dispersion forces, *Nature*, 2011, **477**, 308–311.

209 Y. Ishigaki, T. Shimajiri, T. Takeda, R. Katoono and T. Suzuki, Longest C–C Single Bond among Neutral Hydrocarbons with a Bond Length beyond 1.8 Å, *Chem*, 2018, **1**, 795–806.

210 J. Li, R. Pang, Z. Li, G. Lai, X.-Q. Xiao and T. Müller, Exceptionally Long C−C Single Bonds in Diamino-o-carborane as Induced by Negative Hyperconjugation, *Angew. Chem., Int. Ed.*, 2019, **58**, 1397–1401.

211 J. Llop, C. Viñas, J. M. Oliva, F. Teixidor, M. A. Flores, R. Kivekas and R. Sillanpää, Modulation of the C–C distance in disubstituted 1,2-R_2-o-carboranes. Crystal structure of closo 1,2-$(SPh)_2$-1,2-$C_2B_{10}H_{10}$, *J. Organomet. Chem.*, 2002, **657**, 232–238.

212 H. Arp, J. Baumgartner, C. Marschner, P. Zark and T. Müller, Dispersion Energy Enforced Dimerization of a Cyclic Disilylated Plumbylene, *J. Am. Chem. Soc.*, 2012, **134**, 6409–6415.

213 J. J. Novoa, P. Lafuente, R. E. Del Sesto and J. S. Miller, Exceptionally Long (≥ 2.9 Å) C–C Bonds between $[TCNE]^-$ Ions: Two-Electron, Four-Center π*-π* C–C Bonding in π-$[TCNE]_2^{2-}$, *Angew. Chem., Int. Ed.*, 2001, **40**, 2540–2545.

214 H.-G. Stammler, P. Jutzi, W. Wieland and B. Neumann, (Tributylphosphine-P.)[1,2,4-tris(trimethylsilyl) cyclopentadienyl]silver(I), *Acta Crystallogr.*, 1998, **C34**, 9800064.

215 R. Sievers, M. Sellin, S. M. Rupf, J. Parche and M. Malischewski, Introducing the Perfluorinated Cp* Ligand into Coordination Chemistry, *Angew. Chem., Int. Ed.*, 2022, e202211147, DOI: **10.1002/anie.202211147**.

216 J. M. Kieser, L. O. Jones, M. C. Uible, M. Zeller, G. C. Schatz and S. C. Bart, Late to the Party: Synthesis and Characterization of Tellurium and Selenium Half-Sandwich Complexes, *Organometallics*, 2021, **40**, 4104–4109.

217 H. Hogeveen and P. W. Kwant, Direct observation of a remarkably stable dication of unusual structure: $(CCH_3)_6^{2+}$, *Tetrahedron Lett.*, 1973, **14**, 1665–1670.

218 H. Hogeveen and P. W. Kwant, Pyramidal Mono- and Dications, *Acc. Chem. Res.*, 1975, **8**, 413–420.

219 M. Malischewski and K. Seppelt, Crystal Structure Determination of the Pentagonal-Pyramidal Hexamethylbenzene Dication $C_6(CH_3)_6^{2+}$, *Angew. Chem., Int. Ed.*, 2016, **55**, 1–4.

220 R. Hoffmann, Building Bridges Between Inorganic and Organic Chemistry, *Angew. Chem., Int. Ed. Engl.*, 1982, **21**, 711–724.

221 K. D. Bos, E. J. Bulten, J. G. Noltes and A. L. Spek, The crystal and molecular structure of cyclopentadienyltin(II) chloride. The bonding of the cyclopentadienyl group in tin(II) compounds, *J. Organomet. Chem.*, 1975, **99**, 71–77.

222 R. K. Bohn, K. W. Hillig and R. L. Kuczowski, Pyrrole-argon: Microwave spectrum, structure, dipole moment, and ^{14}N quadrupole coupling constants, *J. Phys. Chem.*, 1989, **93**, 3456–3459.

223 W. Caminali, P. G. Favero and B. Velino, Adducts of aromatic molecules with rare gases: rotational spectrum of pyrazole-argon, *Chem. Phys.*, 1998, **239**, 223–227.

224 W. Caminali, S. Melandri, A. Millemaggi and P. G. Favero, Rotational spectrum of the imidazole-argon complex, *Chem. Phys. Lett.*, 1998, **294**, 377–380.

225 S. G. Kukolich, Microwave structure measurements on the furan-argon complex, *J. Am. Chem. Soc.*, 1983, **105**, 2207–2210.

226 R. M. Spycher, L. Hausherr-Primo, G. Grassi and A. Bauder, Rotational spectra of isotopic furan-$(argon)_n$, n=1,2, complexes and their vibrationally averaged structures, *J. Mol. Struct.*, 1995, **351**, 7–17.

227 W. Drescher and C. Kleeberg, Terminal versus Bridging Boryl Coordination in N-Heterocyclic Carbene Copper(I) Boryl Complexes: Syntheses, Structures, and Dynamic Behavior, *Inorg. Chem.*, 2019, **58**, 8215–8229.

228 N. Parvin, J. Hossain, A. George, P. Parameswaran and S. Khan, N-heterocyclic silylene stabilized monocordinated copper(i)–arene cationic complexes and their application in click chemistry, *Chem. Commun.*, 2020, **56**, 273–276.

229 D. Franz, A. H. Ilkhechi, M. Bolte, H.-W. Lemer and M. Wagner, A Quest for Ligand-Unsupported Li^+–π

Interactions in Mono-, Di-, and Tritopic Lithium Arylborates, *Eur. J. Inorg. Chem.*, 2011, 5414–5421.

230 A. V. Zabula, A. Y. Rogachev, I. A. Buzei and R. West, Silicon in a Negatively Charged Shell: Anions of Spirosilabifluorene, *Organomet*, 2013, **32**, 3760–3768.

231 N. Solcà and O. Dopfer, Protonated Benzene: IR Spectrum and Structure of $C_6H_7^+$, *Angew. Chem., Int. Ed.*, 2002, **41**, 3628–3631.

232 S. Krieck, H. Gorls, L. Yu, M. Reiher and M. Westerhausen, Stable "Inverse" Sandwich Complex with Unprecedented Organocalcium(I): Crystal Structures of $[(thf)_2Mg(Br)\text{-}C_6H_2\text{-}2,4,6\text{-}Ph_3]$ and $[(thf)_3Ca\{\mu\text{-}C_6H_3\text{-}1,3,5\text{-}Ph_3\}Ca(thf)_3]$, *J. Am. Chem. Soc.*, 2009, **131**, 2977–2985.

233 C. Jones, L. McDyre, D. M. Murphy and A. Stasch, Magnesium(i) reduction of benzophenone and anthracene: first structural characterisation of a magnesium ketyl, *Chem. Commun.*, 2010, **46**, 1511–1513.

234 B. Freitag, J. Pahl, C. Farber and S. Harder, Syntheses of Heteroleptic Amidinate Strontium Complexes Using a Superbulky Ligand, *Organometallics*, 2018, **37**, 469–475.

235 X. Shi and J. Cheng, Reversible addition and hydrogenation of 1,1-diphenylethylene with a barium complex, *Dalton Trans.*, 2019, **48**, 8565–8568.

236 Q. Wang, S. Pan, Y.-B. Wu, G. Deng, J.-H. Bian, G. Wang, L. Zhao, M. Zhou and G. Frenking, Transition-Metal Chemistry of Alkaline-Earth Elements: The Trisbenzene Complexes $M(Bz)_3$ (M=Sr, Ba), *Angew. Chem., Int. Ed.*, 2019, **58**, 17365–17374.

237 K. Yuvaraj and C. Jones, Reductive coupling of CO with magnesium anthracene complexes: formation of magnesium enediolates, *Chem. Commun.*, 2021, **57**, 9224–9227.

238 J. Pahl, A. Friedrich, H. Elsen and S. Harder, Cationic Magnesium π–Arene Complexes, *Organomet*, 2018, **37**, 2901–2909.

239 B. Rosch, T. X. Gentner, J. Langer, C. Farber, J. Eyselein, L. Zhao, C. Ding, G. Frenking and S. Harder, Dinitrogen complexation and reduction at low-valent calcium, *Science*, 2021, **371**, 1125–1128.

240 A. S. S. Wilson, M. S. Hill and M. F. Mahon, Calcium Hydride Insertion Reactions with Unsaturated C–C Bonds, *Organomet*, 2018, **38**, 351–360.

241 J. T. Boronski, A. E. Crumpton, L. L. Wales and S. Aldridge, Diberyllocene, a stable compound of Be(I) with a Be–Be bond, *Science*, 2023, **380**, 1147–1149.

242 U. Thewalt, T. Zafiropoulos and H. Schmidbaur, Isolation and Crystal Structure of (Hexamethylbenzene)gallium(I) Tetrachlorogallate(III), a Mono(arene) Complex of Gallium(I), *Z. Naturforsch., B: Chem. Sci.*, 1984, **39**, 1642–1646.

243 L. Kuppers and W. Frank, Investigation of mesitylene-solvated group 13 mixed-metal halides: syntheses and crystal structures of bis(1,3,5-trimethylbenzene)gallium(I) tetrachlorido- and tetrabromidoaluminate(III) and (1,3,5-trimethylbenzene)gallium(I) tetraiodidoaluminate(III). Variation of the gallium-π-arene bond strength, *Z. Naturforsch., B: Chem. Sci.*, 2019, **74**, 773–782.

244 M. Schorpp, S. Rein, S. Weber, H. Scherer and I. Krossing, Guilty and charged: a stable solution of the hexamethylbenzene radical cation as a ligand forming oxidising agent, *Chem. Commun.*, 2018, **54**, 10036–10039.

245 Y. Sarazin, N. Kaltsoyannis, J. A. Wright and M. Bochmann, Mono(arene) Complexes of Thallium(I) Supported by a Weakly Coordinating Anion, *Organometallics*, 2007, **26**, 1811–1815.

246 E. V. Anslyn, *Modern Physical Organic Chemistry*, University Science Books, Sausalito, CA, 2006.

247 R. D. Shannon and C. T. Prewitt, Effective Ionic Radii in Oxides and Fluorides, *Acta Crystallogr.*, 1969, **B25**, 925–946.

248 R. D. Shannon, Revised Effective Ionic Radii and Systematic Studies of Interatomic Distances in Halides and Chalcogenides, *Acta Crystallogr.*, 1976, **A32**, 751–767.

249 Y. Marcus, Ionic Radii in Aqueous Solutions, *Chem. Rev.*, 1988, **88**, 1475–1498.

250 E. Madelung, Das elektrische Feld in Systemen von regelmässig angeordneten Punktladungen, *Phys. Z.*, 1918, **19**, 524–533.

251 L. Liu and W. A. Bassett, Compression of Ag and phase transformation of NaCl, *J. Appl. Phys.*, 1973, **44**, 1475–1479.

252 I. E. Hooton and P. W. M. Jacobs, Ionic conductivity of pure and doped sodium chloride crystals, *Can. J. Chem.*, 1988, **66**, 830–835.

253 L. A. Martínez-Cruz, A. Ramos-Gallardo and A. Vegas, MSn and $MSnO_3$ (M = Ca, Sr, Ba): New Examples of Oxygen-Stuffed Alloys, *J. Solid State Chem.*, 1994, **110**, 397–398.

254 A. Vegas, *Structural Models of Inorganic Crystals, From the elements to the compounds*, Universitat Politècnica de València, Valencia, 2018.

255 M. Fu, S. Pan, L. Zhao and G. Frenking, Bonding Analysis of the Shortest Bond between Two Atoms Heavier than Hydrogen and Helium: O_2^{2+}, *J. Phys. Chem. A*, 2020, **124**, 1087–1092.

256 E. Blokker, X. Sun, J. Poater, J. M. van der Schuur, T. A. Hamlin and F. M. Bickelhaupt, The Chemical Bond: When Atom Size Instead of Electronegativity Difference Determines Trend in Bond Strength, *Chem. – Eur. J.*, 2021, **27**, 15616–15622.

257 A. Falceto and S. Alvarez, Comparison of the Cr-Cr quadruple and quintuple bonding mechanisms, *Struct. Bonding*, 2016, **170**, 149–164.

258 L. Gagliardi and B. O. Roos, Quantum chemical calculations show that the uranium molecule U_2 has a quintuple bond, *Nature*, 2005, **433**, 848–851.

259 P. F. Souter, G. P. Kushto, L. Andrews and M. Neurock, Experimental and Theoretical Evidence for the Formation of Several Uranium Hydride Molecules, *J. Am. Chem. Soc.*, 1997, **119**.

260 M. Autillo, R. E. Wilson, M. Vasiliu, G. F. de Melo and D. A. Dixon, Periodic Trends within Actinyl(VI) Nitrates and Their Structures, Vibrational Spectra, and Electronic Properties, *Inorg. Chem.*, 2022, **61**, 15607–15618.

261 B. O. Roos, A. C. Borin and L. Gagliardi, Reaching the Maximum Multiplicity of the Covalent Chemical Bond, *Angew. Chem., Int. Ed.*, 2007, **46**, 1469–1472.

262 J. Echeverría, G. Aullón and S. Alvarez, Dihydrogen Interactions in Group 13 Compounds: H···H or E···H (E = B, Al, Ga) Interactions?, *Dalton Trans.*, 2017, **46**, 2844–2854.

263 M. B. Brands, J. Nitsch and C. Fonseca-Guerra, Relevance of Orbital Interactions and Pauli Repulsion in the Metal−Metal Bond of Coinage Metals, *Inorg. Chem.*, 2018, **57**, 2603.

264 A. Carvajal, S. Alvarez and J. J. Novoa, The Nature of Intermolecular $Cu^{I}\cdots Cu^{I}$ Interactions: A Combined Theoretical and Structural Database Analysis, *Chem. – Eur. J.*, 2004, **10**, 2117–2132.

265 J. Echeverría, J. D. Velasquez and S. Alvarez, Understanding the Interplay of Dispersion, Charge Transfer, and Electrostatics in Noncovalent Interactions: The Case of Bromine−Carbonyl Short Contacts, *Cryst. Growth Des.*, 2020, **20**, 7180–7187.

266 I. Benito, R. M. Gomila and A. Frontera, On the energetic stability of halogen bonds involving metals: implications in crystal engineering, *CrystEngComm*, 2022, **24**, 4440–4446.

267 A. K. Srivastava and N. Misra, Calculating interaction energies of hydrogen bonded dimers and complexes of HF, H_2O and NH_3: Super-molecular versus AIM Approach, *J. Comput. Methods Mol. Des.*, 2014, **4**, 19–23.

268 M. Freindorf, E. Kraka and D. Cremer, A Comprehensive Analysis of Hydrogen Bond Interactions Based on Local Vibrational Modes, *Int. J. Quantum Chem.*, 2012, **112**, 3174–3187.

269 L. Zhao, M. von Hopffgarten, D. M. Andrada and G. Frenking, Energy decomposition analysis, *Wiley Interdiscip. Rev.: Comput. Mol. Sci.*, 2018, **8**, e1345.

270 G. Gayatri, Y. Soujanya, I. Fernández, G. Frenking and G. N. Sastry, Further Shortening of the C-C Single Bond in Substituted Tetrahedranyl Tetrahedrane Systems: An Energy Decomposition Analysis, *J. Phys. Chem. A*, 2008, **112**, 12919–12924.

271 L. Zhang, F. Ying, W. Wu, P. C. Hiberty and S. Shaik, Topology of Electron Charge Density for Chemical Bonds from Valence Bond Theory: A Probe of Bonding Types, *Chem.–Eur. J.*, 2009, **15**, 2979–2989.

272 M. Kaupp, D. Danovich and S. Shaik, Chemistry is about energy and its changes: A critique of bond-length/bond-strength correlations, *Coord. Chem. Rev.*, 2017, **344**, 355–362.

273 M. S. Nechaev, V. M. Rayón and G. Frenking, Energy Partitioning Analysis of the Bonding in Ethylene and Acetylene Complexes of Group 6, 8, and 11 Metals: $(CO)_5TM\text{-}C_2H_x$ and $Cl_4TM\text{-}C_2H_x$ (TM) Cr, Mo, W), $(CO)_4TM\text{-}C_2H_x$ (TM) Fe, Ru, Os), and $TM^{+}\text{-}C_2H_x$ (TM = Cu, Ag, Au), *J. Phys. Chem. A*, 2004, **108**, 3134–3142.

274 R. Tonner, G. Heydernrych and G. Frenking, Bonding Analysis of N-Heterocyclic Carbene Tautomers and Phosphine Ligands in Transition-Metal Complexes: A Theoretical Study, *Chem.–Asian J.*, 2007, **2**, 1555–1567.

275 L. d. A. Santos, S. C. C. van der Lubbe, T. A. Hamlin, T. C. Ramalho and F. M. Bickelhaupt, A Quantitative Molecular Orbital Perspective of the Chalcogen Bond, *ChemistryOpen*, 2021, **10**, 391–401.

276 J. D. Velasquez, J. Echeverría and S. Alvarez, Structure and bonding of halonium compounds, *Inorg. Chem.*, 2023, **23**, 8980–8992.

277 N. Kumar, S. Saha and G. N. Sastry, Towards developing a criterion to characterize non-covalent bonds: a quantum mechanical study, *Phys. Chem. Chem. Phys.*, 2021, **23**, 8478–8488.

278 S. J. Grabowski, What Is the Covalency of Hydrogen Bonding?, *Chem. Rev.*, 2011, **111**, 2597–2625.

279 L. M. P. Madureira, L. G. Dias, R. L. T. Parreira and G. F. Caramori, Shedding light on the physical nature of ion pair involving carba-closo-dodecaborate anions. Insights from computation, *Phys. Chem. Chem. Phys.*, 2023, **25**, 5710–5717.